Three-Dimensional Modelling of Simultaneous Saccharification and Fermentation of Cellulose to Ethanol

by

Josebus Maree van Zyl

Dissertation presented for the degree of Doctor of Philosophy in Engineering at Stellenbosch University

Promotor: Prof. Thomas Michael Harms
Co-Promotor: Prof. Lee Rybeck Lynd
Faculty of Engineering

March 2012

DECLARATION

By submitting this dissertation electronically, I declare that the entirety of the work contained therein is my own, original work, that I am the sole author thereof (save to the extent explicitly otherwise stated), that reproduction and publication thereof by Stellenbosch University will not infringe any third party rights and that I have not previously in its entirety or in part submitted it for obtaining any qualification.

Signature: ..... Date: 13 February 2012

ABSTRACT

Second-generation bioethanol is an alternative transportation fuel currently being investigated whereby cellulose, specifically lignocellulosic (woody) portions, of any plant mass can be converted to ethanol. To date, the technology had only been successfully implemented with demonstration scale facilities. Despite intensive research efforts at laboratory scale, no-one is certain what the secondary effects of scale-up to large systems are. The objective of this project was to develop three-dimensional numerical models of a laboratory scale fermenter which could predict the effects of particulate mixing and reaction kinetics for future scale-up investigations.

A numerical model of the reaction kinetics for simultaneous saccharification and fermentation of Avicel (microcrystalline cellulose) particles to ethanol is presented. The novelty of this model is the separation of the two primary cellulase enzyme-kinetics, which generated the capability to predict the heterogeneous behaviour of the enzyme-substrate interactions. This model improves the understanding of these systems while maintaining sufficient simplicity for implementation alongside a commercial computational fluid dynamics environment.

Effects of the various fermentation medium constituents and the influence of each on the dynamic viscosity of the medium were also investigated. Results indicated that particle volume fraction had the dominant effect on the apparent dynamic viscosity resulting in further research of the particle properties. Due to the irregular shapes of Avicel particles, tests were conducted to determine drag and settling behaviour, which led to the development and modification of models to account for these phenomena. This investigation is unique as it allows a more accurate calculation of particle transportation through a three-dimensional environment including the effects of natural packing density. At lower particle volume fraction the concentration of ethanol and glycerol had the greatest effect on the apparent dynamic viscosity and was calculated from models obtained from literature.

Validation of the physics and the incorporation thereof in the simulations resulted in the modification of various generic models which either improved numerical stability or accuracy, or both. Contributions included a modified form of the pressure force model, which proved significantly more stable and accurate than previous models proposed in literature. The models developed for capturing the effects of particles on the apparent dynamic viscosity proved effective for this specific substrate.

Results from cross-coupling the reaction models with computational fluid dynamic simulations provide a novel approach to capturing the secondary effect of substrate conversion and particle distribution on the performance of the fermentation vessels. This is the first time where that biological reactions were

successfully combined with particle dynamics and fluid flow fields to investigate the secondary effects which occur in fermenters.

This work served as a foundation for future research and development within the bioethanol field with significant potential for expansion into other biochemical disciplines.

OPSOMMING

Tweede-generasie bioetanol is 'n alternatiewe vervoerbrandstof wat tans ondersoek word waar sellulose, spesifiek lignosellulosiese (houtagtige) gedeeltes, van enige plantmassa na etanol omgesit kan word. Tot op hede was die tegnologie slegs suksesvol geïmplimenteer in demonstrasieskaal fasiliteite. Ten spyte van intensiewe navorsingpogings op laboratoriumskaal, is niemand seker wat die sekondêre effekte van die opskaal tot groot stelsels sal wees nie. Die doelwit van die projek was om drie-dimensionele modelle te ontwikkel van 'n laboratoriumskaal fermentor wat die effekte van partikulêre vermenging en reaksiekinetika kan voorspel vir toekomstige opskaal navorsing.

'n Numeriese model van die reaksiekinetika vir gelyktydige versuikering en fermentasie van Avicel (mikrokristallyne sellulose) partikels tot etanol word aangebied. Die oorspronklikheid van die model is geleë in die skeiding van die twee primêre sellulase ensiemkinetika, wat lei tot die vermoë om die heterogene gedrag van die ensiem-substraat interaksies te voorspel. Hierdie model verbeter die kennis van die stelsels, terwyl voldoende eenvoud behoue bly vir implementering parallel aan kommersiële berekeningsvloeidinamika sagteware.

Effekte van die verskillende bestanddele van die fermentasiemedium en die invloed van elk op die dinamiese viskositeit van die medium is ook ondersoek. Resultate dui aan dat partikel volume fraksie die dominante invloed op die skynbare dinamiese viskositeit het, wat gelei het tot verdere ondersoek van die partikel eienskappe. As gevolg van die onreëlmatige vorms van Avicel partikels, is toetse gedoen om die sleur-en uitsakkingsgedrag te bepaal, wat gelei het tot die ontwikkeling en aanpassing van modelle om hierdie verskynsels in ag te neem.

Hierdie ondersoek is uniek, want dit laat meer akkurate berekening van partikelvervoer deur 'n drie-dimensionele omgewing toe, insluitend die effekte van natuurlike verpakkingsdigtheid. By laer partikel volume fraksie het die konsentrasie van etanol en gliserol die grootste effek op die skynbare dinamiese viskositeit gehad en was bereken vanaf modelle in die literatuur.

Bevestiging van die fisika en die insluiting daarvan in die simulasies het gelei tot die aanpasing van verskillende generiese modelle wat óf numeriese stabiliteit óf akkuraatheid óf beide verbeter. Bydraes gemaak sluit 'n aangepaste vorm van die drukkragmodel in, wat heelwat meer stabiel en akkuraat was as die vorige modelle voorgestel in die literatuur. Die modelle wat ontwikkel is om die effek van partikels op die skynbare viskositeit vas te vang, was effektief bewys vir hierdie spesifieke substraat.

Resultate van die kruiskoppeling van inligting vanaf die reaksiemodelle met berekeningsvloeidinamika simulasies lewer 'n nuwe benadering tot die bepaling van die sekondêre effek van substraatomskakeling en partikeldistribusie op die uitvoering van die fermentasie toestel. Hierdie is die eerste poging om biologiese

reaksies met partikel dinamika en vloeivelde te kombineer om die sekondêre effekte wat in fermenter plaasvind, te ondersoek.

Hierdie werk dien as 'n grondslag vir toekomstige navorsing en ontwikkeling binne die bioetanolveld, met beduidende potensiaal vir uitbreiding na ander biochemiese dissiplines.

ACKNOWLEDGEMENTS

The Holy Father for the necessary strength and guidance to hold on and will to continue even when all appeared impossible.

My family for their moral support and foundation to stand on throughout the course of the study.

Professor Thomas M Harms for the endless support and guidance through the difficult journey of my Ph.D.

Professor Lee R Lynd for fruitful discussions pertaining to the bioethanol production process.

Doctor Eugéne van Rensburg for consistent assistance in the microbiology labs and for a great friendship developed.

Professor Jacky Snoep and Arrie Arendse for the use of the fermenters in this study.

My Father, Professor Willem H van Zyl, for endless discussions on biology and a voice of reason during hardships.

The Department of Process Engineering at Stellenbosch University for use of their rheology machine and laboratory equipment during the course of this study.

The Department of Microbiology at Stellenbosch University for the provision of laboratory equipment and chemicals mentioned in this study.

State funding received through the Centre for Renewable and Sustainable Energy Studies and funding received through the Department of Mechanical and Mechatronic Engineering sourced from the Stellenbosch University 'Hope' project.

Genencor and Novozymes for the generous supply of Spezyme® CP and Novozym® 188 enzyme mixture, respectively.

Vicki Vermeulen for the moral support and assistance with the debugging of C code.

TABLE OF CONTENTS

LIST OF FIGURES

LIST OF TABLES

NOMENCLATURE

Symbols

[B]	g/L	Beta-glucosidase concentration
[C]	g/L	Cellulose concentration
$[C]_{endo}$	g/L	Amorphous cellulose concentration
$[C]_{exo}$	g/L	Crystalline cellulose concentration
[Cb]	g/L	Cellobiose concentration
$[C_{f,endo}]$	g/L	Free amorphous cellulose concentration
$[C_{f,exo}]$	g/L	Free crystalline cellulose concentration
$[C_f]$	g/L	Free cellulose concentration
$[CO_2]$	g/L	Carbon dioxide concentration
$[C_T]$	g/L	Total cellulose concentration
[E]	g/L	Cellulase enzyme concentration
[EC]	g/L	Cellulose-enzyme complex concentration
$[EC]_{endo}$	g/L	Cellulose-endoglucanase enzyme complex concentration
$[EC]_{exo}$	g/L	Cellulose-exoglucanase enzyme complex concentration
$[E_{f,endo}]$	g/L	Free endoglucanase enzyme concentration
$[E_{f,exo}]$	g/L	Free exoglucanase enzyme concentration
$[E_f]$	g/L	Free cellulase enzyme concentration
$[E_f]$	g/L	Free enzyme concentration
$[E_T]$	g/L	Total cellulase enzyme concentration
[Eth]	g/L	Ethanol concentration
[G]	g/L	Glucose concentration
[Gly]	g/L	Glycerol concentration
[X]	g/L	Yeast cell concentration
A_{ij}^{D}	kg/m^3·s	Linearised drag co-efficient
a	m^2/s	Variable as a function of temperature and ethanol concentration
$\boldsymbol{A}$	m^2	Face area of a cell surface
b		Variable as a function of temperature
C_D		Drag co-efficient
C_L		Lift co-efficient
C_{VM}		Virtual mass co-efficient
$C_{\varepsilon 1}$		Emperical constant in k-ε turbulence model
$C_{\varepsilon 2}$		Emperical constant in k-ε turbulence model
C_μ		Emperical constant in k-ε turbulence model
C_i^μ		Phase co-efficient in k-ε turbulence model
c_h	h^{-1}	Conversion-independent component in rate function
D	h^{-1}	Dilution rate
D_i	m	Impeller diameter
D_{avg}	m	Effective particle diameter

D_{eff}	m	Effective Stokes diameter of the particles
D_0	m	Original effective particle size
$\boldsymbol{F}_{ij}^{D}$	kg/m^2·s^2	Linearised drag force vector
$\boldsymbol{F}_{L}$	kg/m^2·s^2	Lift force vector
$\boldsymbol{F}_{ij}^{VM}$	kg/m^2·s^2	Virtual mass force vector
$\boldsymbol{F}_{ij}^{TD}$	kg/m^2·s^2	Turbulent dispersion force vector
$F_{i,s}$	kg/m^2·s^2	Turbulent dispersion force vector
$F_{intern,s}$	kg/m^2·s^2	Internal momentum source terms
F_r	kg/m^2·s^2	Rotational body force
$\boldsymbol{g}$	m/s^2	Gravitational constant
G_f	m^3/s	Grid flux
h	kg·m^2/s^2	Enthalpy
K	kg/m·s$^{(1-n)}$	Viscosity variable as a function of volume fraction
k	m^2/s^2	Turbulence kinetic energy
k_i	m^2/s^2	Phase turbulence kinetic energy
K_{C_Cb}	g/L	Inhibition constant of cellobiose on cellulose conversion
K_{C_Eth}	g/L	Inhibition constant of ethanol on cellulose conversion
K_{Cb}	g/L	Rate constant for hydrolysis of cellobiose to glucose
K_{Cb_G}	g/L	Inhibition of hydrolysis of cellobiose by glucose
k_{endo}	h^{-1}	Hydrolysis rate constant of endoglucanase
K_{endo}	L/g	Equilibrium constant for endoglucanase
k_{exo}	h^{-1}	Hydrolysis rate constant of exoglucanase
K_{exo}	L/g	Equilibrium constant for exoglucanase
k_{fc}	h^{-1}	Adsorption rate constant of cellulase
K_G	g/L	Monod constant
k_h	h^{-1}	Hydrolysis rate constant
K_m	g/L	Michaelis constant of β-glucosidase for cellobiose
k_t	kg·m/s^2·K	Thermal conductivity
K_{X_Eth}	g/L	Inhibition of cell growth by ethanol
l_{cd}	m	Characteristic length equal to particle diameter
M	N·m	Moment
m_e	kg	Mass of the ethanol component
m_g	kg	Mass of the glycerol component
M_i	kg/m^2·s^2	Phase momentum source term
m_{total}	kg	Total mass of the solution
m_w	kg	Mass of the water component
N	rpm	Revolutions per minute rotational rate of the Impeller
n		Viscosity power variable as a function of volume fraction
n_D		Exponent co-efficient for Gidaspow drag model
n_h		Exponent of the declining substrate reactivity
P	Pa	Pressure
P_o	kg·m^2/s^3	Power

r_c	g/L·h	Conversion rate of cellulose
Re		Reynolds number
Re_y		Reynolds number for boundary layer calculations
Re_d		Reynolds number for particles
r_i	m	Inner radius
r_o	m	Outer radius
$S_{interphase}$	kg/m^2·s^2	Interphase momentum source terms
S_i^k	kg/m·s^2	Source term for turbulence kinetic energy
S_i^ε	kg/m·s^2	Source term for turbulence eddy dissipation energy
S_i	s^{-1}	Phase mean strain rate
T	K	Absolute temperature
T_i	s	Phase turbulent time scale
t	h	Time
Ta	m^2/s	Taylor number
u	m/s	Cartesian velocity x-component
v	m/s	Cartesian velocity y-component
w	m/s	Cartesian velocity z-component
u'_i or u'_j	m/s	Instantaneous velocity fluctuations vectors
$\overline{u'_i}$ or $\overline{u'_j}$	m/s	Averaged instantaneous velocity fluctuations vectors
u'_x	m/s	Instantaneous velocity fluctuations vector in the x-direction
u'_y	m/s	Instantaneous velocity fluctuations vector in the y-direction
u'_z	m/s	Instantaneous velocity fluctuations vector in the z-direction
u_i or u_j	m/s	Velocity
V	m^3	Volume
$\boldsymbol{V}$	m/s	Velocity vector
$\boldsymbol{v}_i$	m/s	Phase velocity
$\boldsymbol{V}_{P,\,term}$	m/s	Terminal settling velocity of the particles
$\boldsymbol{v}_r$	m/s	Relative velocity between phases
$\boldsymbol{v}_g$	m/s	Grid velocity
V_{rs}		Correction factor for the Syamlal and O'brien drag model
x	m	Cartesian x-coordinate
y	m	Cartesian y-coordinate
z	m	Cartesian z-coordinate
x_c		Substrate conversion fraction
x_e		Molar fraction of ethanol
x_g		Molar fraction of glycerol
x_j or x_i	m	Cartesian vectors
x_w		Molar fraction of water
y	m	Perpendicular distance from surface
y^+		Boundary layer parameter
Y_{CO2_G}		Yield of carbon dioxide cells per gram of glucose
Y_{Eth_G}		Yield of ethanol cells per gram of glucose

Y_{Gly_G}		Yield of glycerol cells per gram of glucose
Y_{X_G}		Yield of yeast cells per gram of glucose
α_c		Volume fraction of the continuous phase
α_d		Volume fraction of the dispersed phase
α_i or α_j		Phase volume fraction
$\alpha_{max,d}$		Maximum solids volume fraction
α_p		Volume fraction of particles
α_{tr}		Transition point for the Syamlal and O'brien drag model
α_x		Volume fraction of yeast cells
$\dot{\gamma}$	s^{-1}	Shear-rate
δ_{ij}		Kronecker delta tensor
ε_i	m^2/s^2	Phase turbulent eddy dissipation energy
μ	kg/m·s	Dynamic viscosity
μ_c	kg/m·s	Dynamic viscosity of the continuous phase
μ_{max}	h^{-1}	Maximum cell growth rate
μ_o	kg/m·s	Base dynamic viscosity of the fluid
μ_p	kg/m·s	Apparent dynamic viscosity due to particles
μ_i	kg/m·s	Phase dynamic viscosity
μ_i^t	kg/m·s	Phase turbulent viscosity
μ_w	kg/m·s	Dynamic viscosity of water
ν	m^2/s	Kinematic viscosity
ν_i	m^2/s	Phase kinematic viscosity
ν_c^t	m^2/s	Continuous phase turbulent kinetic viscosity
ν_e	m^2/s	Kinematic viscosity of ethanol
$\nu_{e/w}$	m^2/s	Kinematic viscosity of the binary aqueous ethanol
ν_w	m^2/s	Kinematic viscosity of water
ρ	kg/m^3	Density
ρ_c	kg/m^3	Density of the continuous phase
ρ_d	kg/m^3	Density of the dispersed phase
ρ_e	kg/m^3	Density of ethanol
ρ_g	kg/m^3	Density of glycerol
ρ_i	kg/m^3	Phase density
ρ_p	kg/m^3	Particle density
ρ_w	kg/m^3	Density of water
ρ_x	kg/m^3	Density of yeast cells
σ		Enzyme adsorption capacity on cellulose
σ_{endo}		Endoglucanse enzyme capacity on Avicel
σ_{exo}		Exoglucanase enzyme capacity on Avicel
σ_k		Turbulent kinetic energy Prandtl number
σ_α		Turbulent Prandtl number
σ_ε		Turbulent dissipation energy Prandtl number
τ	$kg/m·s^2$	Shear stress

τ'_{ij}	kg/m·s^2	Stress tensor
τ_c	h	Time constant in the crystalline cellulose conversion function
ω_i	s^{-1}	Inner angular velocity
ω_o	s^{-1}	Outer angular velocity
$\boldsymbol{\omega}$	s^{-1}	Angular velocity

Abreviations

ASM	Algebraic stress model
BCA	Bicinchoninic acid
BP	British Petroleum
CAD	Computer aided design
CAIT	Climate Analysis Indicators Tool
CbU	Cellobiose units
CFD	Computational fluid dynamics
CMC	Carboxyl-methyl-cellulose
CSTR	Continuous stirred tank reactor
DES	Detached eddy simulations
DME	Department of Minerals and Energy
DMF	Dimethylformamide
DNS	Direct numerical simulation
DNS[1]	3,5-dinitrosalicylic acid
EIA	U.S. Energy Information Administration
EPA	Environment Protection Agency
fps	Frames per second
FPU	Filter paper units
GHG	Green house gas
HD	High-definition
HFC	Hydrofluorocarbons
HSRC	Human Sciences Research Council
IPCC	Intergovernmental Panel on Climate Change
IU	International units
LES	Large eddy simulations
$MtCO_2$	Mega-tonnes of Carbon dioxide
$MtCO_2e$	Mega-tonnes of Carbon dioxide equivalent
NS	Navier-Stokes
OD_{600}	Optical density at a 600 nm wavelength
OICA	International Organization of Motor Vehicle Manufacturers
PFC	Perfluorocarbons
pNPG	p-nitrophenyl-β-D-glucopyranoside
RANS	Reynolds Averaged Navier-Stokes
RO	Reverse osmosis
SC	Synthetic complete

SSF	Simultaneous saccharification and fermentation
UNFCCC	United Nations Framework Convention on Climate Change
VOF	Volume of fluid
YNB	Yeast nitrogen base
YPD	Yeast peptone and dextrose
PCT	Patent corporation treaty
WRI	World Resource Institute

1 INTRODUCTION

1.1 Background

The increasing demand for energy and the growing concern about global climate change has urged researchers to investigate alternative, environmentally cleaner energy sources (Siddiqui and Fleten, 2010). These sources include hydropower, solar, wind, geothermal and biomass derived energy (Panwar *et al.*, 2011). Biofuels is a collective name given to energy fuels derived from biological materials (biomass) and include combustion of biological materials, biogas, biodiesel and bioethanol (Naik *et al.*, 2010). The focus of this study is on the biological production of the latter from cellulose.

Bioethanol can be produced from various biological sources using different chemical and biological processes, which can further be divided into first and second-generation technologies based upon the feedstock used (Naik *et al.*, 2010). First generation technologies utilise energy crops such as sugarcane and maize, which are easily converted to ethanol, while second-generation technologies produce ethanol from cellulose. Cellulose is a glucose polymer abundantly available in plant cell walls and as such have a high recalcitrance to degradation and conversion (Lynd *et al.*, 2002).

Bioethanol derived from cellulosic materials such as grass, trees and waste paper has two major advantages. Firstly, if agriculture and cultivation of these sources are managed correctly, these sources can be produced in abundance worldwide providing a vast source for energy (Hall *et al.*, 2010; Ryu and Mandels, 1980 and Durand *et al.*, 1984). Furthermore this technology is capable of closing the carbon cycle thereby minimising the net CO_2 emissions to the atmosphere (Naik *et al.*, 2010). It has also been shown to promote sequestration of CO_2, effectively reducing the atmospheric CO_2 concentration, slowing and possibly eventually counteracting extreme climatic change (Cannell, 2003 and Ryu and Mandels, 1980).

Secondly, cellulosic ethanol does not compete with food sources (Naik *et al.*, 2010). Instead it enables the more efficient use of agricultural produce, as farming residue can now be converted into a fuel source instead of incinerated, which is a common agricultural practise.

Therefore developing efficient technologies and processes to overcome the recalcitrance of lignocellulosic materials will provide significant improvement in energy security in the transport sector, while reducing the negative effects of large transport networks on the environment (Wyman, 2007).

This project investigates the numerical simulation of simultaneous saccharification and fermentation of cellulose particles to ethanol. This process involves the enzymatic hydrolysis of cellulose by cellulases to form oligosaccharides and trace amounts of glucose with cellobiose further hydrolysed

by β-glucosidases to release the remaining glucose (Lynd *et al.*, 2002). The glucose formed by the hydrolysis process is fermented by yeast to form ethanol, carbon dioxide, glycerol and other products in trace amounts. The conversion of cellulose to ethanol affects the fluid properties of the fermentation medium thus influencing the mixing conditions which occur within the reactor. These effects were investigated and modelled using commercial computational fluid dynamics software.

1.2 Problem Statement

Cellulosic ethanol is rapidly becoming commercially viable, with demonstration-scale plants constructed worldwide, for example DuPont Danisco (Reidy, 2010, DuPont, 2011), Abengoa Bioenergy (Abengoa, 2011) and Mascoma (Mascoma, 2011). Literature on cellulosic ethanol reports various numerical models and extensive experimental results on a widespread selection of feedstock, pretreatment methods, organism characteristic and enzymes (both naturally occurring and genetically modified), reactor configurations and fermentation fluid properties. Unfortunately, each study focuses on a specific aspect resulting in a large database of information with almost no means of combining the results to form a complete dataset for a specific substrate and process condition. Such a dataset is required for numerical simulations to correctly design and optimise production plants for large-scale commercial use.

This general lack of a complete datasets for the biological production of cellulosic ethanol, results in many uncertainties when designing large-scale production plants (Hristov et al., 2004). The development of numerical simulations and a complete dataset for engineers is paramount to secure large investments for the construction of full-scale commercial plants.

1.3 Hypothesis

Computational fluid dynamics (CFD) is a powerful engineering tool often used to evaluate large complicated thermodynamic and fluid flow problems. It is believed that should a complete set of kinetic models and corresponding fluid properties be available, engineers could utilise CFD to evaluate various reactor configurations. This will allow engineers to ensure sufficient suspension of feedstock particles, maximising the exposed particle surface area, while maintaining favourable conditions for the enzymatic hydrolysis and fermentation of cellulose or lignocellulosic particles.

The several orders of magnitude difference in time-scale between the mixing rate and reaction rates in these biological reactions cause a problem for simulations. To correctly capture mixing conditions, simulations require a time-step in the order of milliseconds, while the reaction rates can be captured with time-steps in the order of minutes. To overcome this problem it is suggested that if the cellulose particles are maintained in a fully suspended state without excessive turbulence and shear-stress in the fluid, the reactions will occur optimally and

one-dimensional kinetic models are sufficient to determine the concentrations of the various elements in the fermentation broth. Using numerical models to predict the fluid properties of the fermentation medium based on its contents will allow for feasible CFD simulations to accurately predict the mixing conditions within the reactors.

1.4 Objectives

The first objective of the project was to investigate a simple simultaneous saccharification and fermentation process to convert microcrystalline cellulose to ethanol. This process included modelling the enzymatic hydrolysis of the cellulose particles to polysaccharides, primarily cellobiose, which is further hydrolysed enzymatically to form glucose. The glucose is fermented by the yeast *Saccharomyces cerevisiae* to form ethanol, glycerol and carbon dioxide. This investigation allowed the development of an one-dimensional numerical model of the biological reactions under ideal conditions which could predict the reactor contents under ideal fully suspended conditions. Fully suspended particles are ideal as it ensures the maximum exposed feedstock surface area allowing optimal enzyme-substrate accessibility.

The second objective required the analyses of the apparent dynamic viscosity of the bulk fluid in the reactors throughout such a biological process. Development of a numerical model which could approximate the apparent dynamic viscosity within the reactors was thus required for determining the fluid flow conditions to be used in CFD simulations. Each significant constituent within the reactors was investigated to determine which contributed to the final apparent dynamic viscosity. A simple model was proposed to approximate the final reactor broth properties.

The third objective was to model a 1.3 L stirred tank reactor using CFD to evaluate the applicability of this technology to modelling biological systems, with the focus on the effect of the particle transport and distribution on the kinetic reaction models and vice-versa. This included the development of new models to capture the effects of particle packing and parameter estimation for such simulations.

1.5 Dissertation Contribution

Relevant literature is reviewed in Chapter 2, discussing the economical, political and environmental aspects supporting the necessity to research alternative energy sources. A brief introduction to 1st and 2nd-generation bioethanol technology is presented and the processes required for lignocellullose to ethanol conversion are discussed.

The kinetic reaction models, originally proposed by South *et al.* (1995) and Shao *et al.* (2008), were adapted for use with the microcrystalline cellulose (Avicel) particles (Chapter 3). This model was further improved to account for inhibitive

site competition on the particle surface. This model could more accurately predict the initial adsorption and subsequent detachment of the enzymes from the particle surface, as the number of available bonding sites diminished. This supports the theory that the enzymes perform at a constant rate, while the drop in reactivity of microcrystalline cellulose particles is caused primarily by the lack of available bonding sites (van Zyl *et al.*, 2011).

The viscosity of the fermentation broth was analysed using a concentric cylinder double gap rheology instrument (Chapter 4). It was found that for particle concentrations above 20 g/L, the cellulose particles influenced the dynamic viscosity of the fermentation broth greatly, rendering viscous contributions from the other constituents negligible. However, at particle concentrations below 20 g/L, ethanol was found to dominate the influence of the final dynamic viscosity. In Chapter 4 the particle properties, including density, settling rate and effective spherical particle size are further discussed, as these parameters are required for numerical simulations.

Information from both Chapter 3 and Chapter 4 have been filed in a PCT patent (van Zyl et al., 2011).

The models required for the CFD simulations of cellulosic ethanol are discussed and presented in Chapter 5. Various methodologies commonly used to simulate particulate flow are examined and their limitations stated. The selection of numerical models are described, presenting the advantages and disadvantages of each choice, with the focus on determining an effective modelling strategy. Furthermore, the particle model used for the CFD simulations are validated and discussed in Chapter 5.

CFD models of a 1.3 L reactor are described in Chapter 6, and results of the influences of mixing conditions and reaction rates within the reactors presented. Using the information from the particle properties, kinetic model and viscosity, a small scale reactor simulation was generated to illustrate the potential of CFD for this technology.

A preliminary study was conducted to determine the effects of cell and substrate recycling (Appendix C) using kinetic models developed by South *et al.* (1995) and Shao *et al.* (2008) for poplar wood. Results indicated that for a cell and substrate feedback system incorporated into a continuous stirred tank reactor configuration, recycling of cell and solids back to the reactor at maximum permissible concentrations may have a significant increase in the ethanol production. The presence of lignin, however, could significantly reduce the cellulose conversion rates and possible restrict the feedback capability of such systems and this study was thus abandoned and inserted as an appendix.

This dissertation concludes with the discussions and conclusions drawn from the study and proposes future studies and recommendations to improve the knowledge in this field.

2 LITERATURE REVIEW

2.1 Sources of Greenhouse Gases

The world population is currently estimated at 7 billion people (U.S. census Bureau, 2009) requiring energy, food, health and transportation. Automobile usage worldwide is estimated to approach 1 billion vehicles (World Bank, 2008) with global production exceeding 73 million vehicles per annum (OICA, 2008). Automobiles produce air pollutants including sulphur oxides (SO_x), nitrogen oxides (NO_x), hydrocarbons (HC), lead, particulates, carbon monoxide (CO) and carbon dioxide (CO_2) (Sagar, 1995, Faiz *et al.*, 1990). Lead was, however, banned by the Clean Air Act in 1996 (EPA, 1996) and subsequently phased out of all fuels. The remaining pollutants are known to have detrimental environmental and medical affects and are present in all transport fuel exhaust gases. The introduction of catalytic converters (Twigg, 2007) to vehicle exhaust systems significantly reduced products of incomplete combustion, resulting in primarily N_2, CO_2 and $H_2O_{(v)}$ remaining, with N_2 and $H_2O_{(v)}$ being completely harmless to the environment.

CO_2 is essentially harmless to the human health unless excessive levels are reached, which causes asphyxiation. Carbon dioxide is, however, recognised as a greenhouse gas (GHG) and as such it receives much attention in the context of global climate change (Sagar, 1995; Reilly *et al.*, 2007; Florides and Christodoulides, 2009, Baumert *et al.*, 2005; IPCC, 2007). It is estimated that approximately 30 000 $MtCO_2$/year is released into the atmosphere globally with the transportation sector accounting for approximately 20 % of the total global carbon dioxide emissions (WRI, 2011). The remaining sources of CO_2 emissions are presented in Figure 2-1.

There are six anthropological GHGs identified by the UNFCCC for monitoring climate change, namely; CO_2, methane (CH_4), nitous oxide (N_2O), and the three fluorinated gases; sulphur hexafluoride (SF_6), perfluorocarbons (PFCs) and hydrofluorocarbons (HFCs) (Baumert *et al.*, 2005, IPCC, 2007). The primary sources of the non-CO_2 gases are presented in Table 2-1 (Baumert *et al.*, 2005). The total yearly emissions of these six gases are estimated at 37 809 $MtCO_2e$/Year, with CO_2 contributing about 72.8 % (Figure 2-2) of the total selected gases (WRI, 2009). It is this large proportion which explains why CO_2 receives the primary attention when climate change studies are conducted.

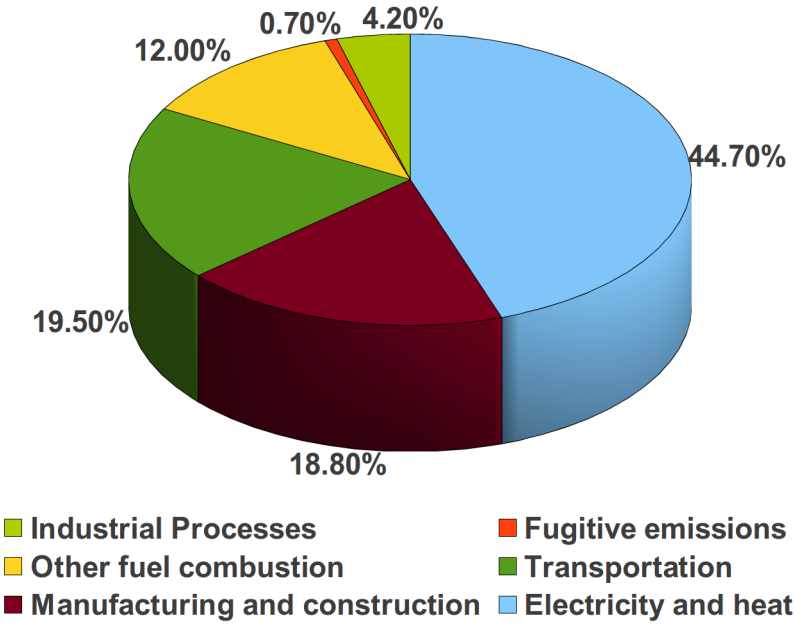

Figure 2-1: World carbon dioxide emissions for 2005

Table 2-1: Selected sources of non-CO_2 greenhouse gases

Methane (CH_4)	Nitrous Oxide (N_2O)	Fluorinated Gases
Land Fills	Agricultural soils	Substitutes for ozone-depleting substances (HFCs, PFCs)
Coal Mining	Adipic and nitric acid production	
Natural Gas and oil systems	Fossil fuel combustion	Industrial activities, including: Semi-conductor manufacturing (PFCs, SF_6, HFCs) Electrical transmission and distribution (SF_6) Aluminium production (PFCs) Magnesium production (SF_6)
Livestock (enteric fermentation)	Livestock manure management	
Livestock manure management	Human sewage	
Waste-water treatment		
Rice cultivation		
Biomass combustion		
Fossil fuel combustion		

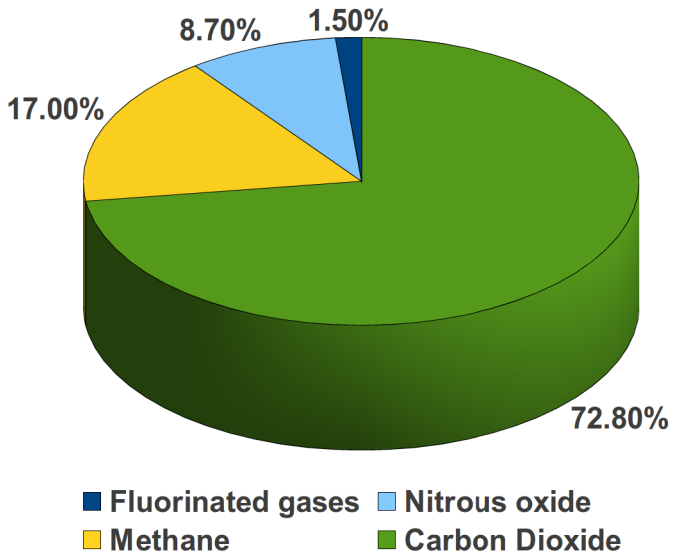

Figure 2-2: Contribution of selected greenhouse gases to climate change

Literature reports various studies on the correlation of global climate change and anthropological CO_2 emissions. In 2007 the Intergovernmental Panel on Climate Change (IPCC) reported an observed total global temperature rise of 0.74 °C over the 100-year trend (1906-2005) (IPCC, 2007). Disagreement exists between various scientific research results whether global climate change is directly caused by anthropological CO_2 emissions or whether it is a natural cyclic global phenomenon (Florides and Christodoulides, 2009). Reilly *et al.* (2007) indicated that if GHG emissions are left uncontrolled, average global temperatures and CO_2 concentrations could respectively rise by 2.75 °C and to 810 ppm by the year 2100. Reilly *et al.* (2007) further showed that average global temperatures and CO_2 concentrations would respectively increase by only 1 °C and to 515 ppm by 2100 if the GHGs are immediately restricted. Baumert *et al.* (2005) states that if the global average temperature is to be kept from rising 2 °C above pre-industrial levels, worldwide emissions would need to peak around 2015 with subsequent emissions decline by 40 % to 45 % by 2050 compared to 1990 levels.

Fuel security and the reduction of GHG emission and additional air pollutants (Janssen *et al.*, 2007) are other important factors that impact on human survival. Humans have largely become depended on fossil fuels as the primary energy source. These sources are limited (Linde *et al.*, 2008a), with oil, natural gas and coal reserves expected to be depleted within approximately 41, 60 and 133 years respectively (BP, 2008).

The limited resources and social-economic factors have caused the oil price (EIA, 2011) to rise steeply (Figure 2-3) placing financial strain on the global population.

The rise in oil price has increased the drive to search for alternative transportation fuels including; alcohol, gaseous hydrocarbons fuel, electricity and hydrogen fuel (Sagar, 1995). Although alcohol fuels can be produced from fossil fuels, biomass-derived alcohols have the greatest potential in reducing the total CO_2 emissions (Sagar, 1995,). Biomass-derived alcohols are produced from the fermentation of photosynthetic plant material rich in starch sugar, or cellulose. Until the containment issues of hydrogen fuels are solved or clean electricity becomes readily available for electric vehicles with economic and sustainable advances in battery technology, the bioethanol-from-biomass route might prove to be the most viable option.

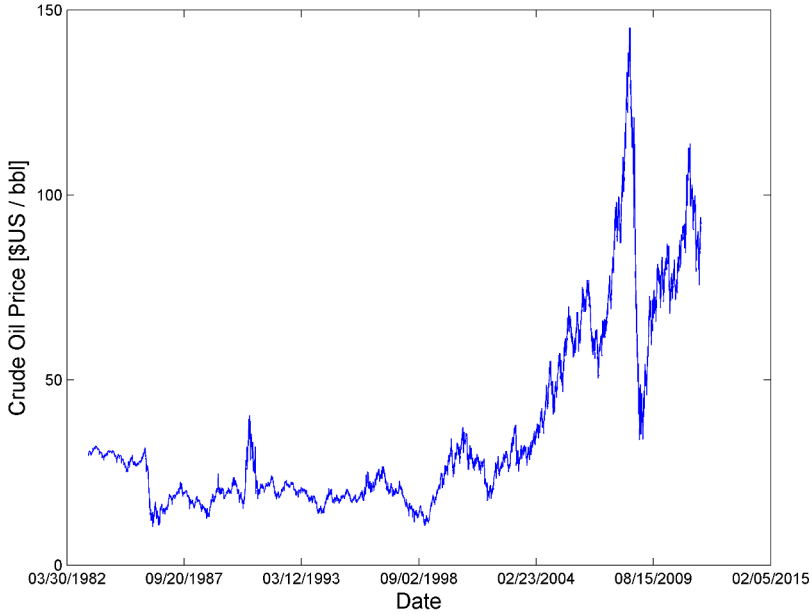

Figure 2-3: Crude oil prices since 1976 to present day

2.2 Energy in South Africa

South Africa used bioethanol from sugarcane in petrol between 1920's and 1960's (DME, 2007). This practice ceased with the low international crude oil prices at the time. With current oil prices soaring to over $100/bbl (EIA, 2011), the biofuel industry is receiving a second opportunity.

The biofuels industrial strategy of the Republic of South Africa specifies that a penetration level of 2 % must be implement within the South African liquid fuel market by 2013. Feedstock specified for biofuels production include sugar cane and sugar beet for the production of bioethanol and sunflower, canola and soya beans for the production of biodiesel (DME, 2007). This penetration level was selected to establish the biofuels industry without jeopardising the food security of

the country. The initial stages of this strategy required 1.4 % of arable land in South Africa, which has 14 % underutilised land especially within the rural areas.

Biodiesel and bioethanol benefit from fuel levy exemptions. Biodiesel receives 50 % and bioethanol 100 % exemption. Bioethanol maintains its 100 % levy on the grounds that it can be used in markets other than transportation, such as ethanol gel that competes with illuminating paraffin, which receives no levies (DME, 2007).

South Africa has an unemployment rate of 25 % (Statistics South Africa, 2011). This unfortunate situation leads to crime (Demombynes and Özler, 2005) and a large economical burden on the rest of the working community. The development of a biofuels industry in South Africa could promote farming in areas previously neglected by the government and create market access for produce. This creates many new job opportunities which could help alleviate poverty in some regions.

Considering the generally unfavourable economic conditions in South Africa (HSRC , 2004), there exists a continuous debate about whether or not biofuels will be detrimental to the food security of the country, possibly depriving citizens of food. Recent studies (DME, 2007) indicate that development of a biofuels market in South Africa would promote the production of additional farming produce, as farmers would suffer lower economical risk in the yearly investment of sowing crops. This is mainly due to an increase in market availability and in the event of significant crop damage, which is unfit for sale as food, the farms could salvage the damage and sell the damaged crops for fuel production.

2.3 1st-Generation Bioethanol Technology

First generation bioethanol is primarily produced from starch and sucrose (Berlin *et al.*, 2006) with America and Brazil being the largest leaders in the field. The primary feedstock used in the United States of America (USA) is starch from maize, while Brazil uses cane sugar. Europe produces its bioethanol from starch originating from wheat and barley, although their global contribution amounts to only a few percent (Linde, 2008a).

Production of bioethanol from maize (Figure 2-4) starts with the milling of the maize kernels or corn to form a meal and open the structure for enzymatic accessibility. Enzymes then hydrolyse the starch (glucose polymers) to form glucose. These sugars are fermented by yeast to form ethanol and CO_2. The ethanol is further washed and distilled from the fermentation broth and dried before supplied to fuel companies for blending with petrol.

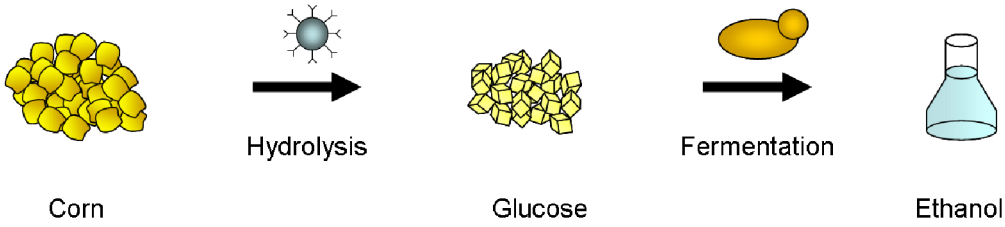

Figure 2-4: First generation bioethanol production process

Bioethanol production from sugarcane follows a more simplistic route, whereby the harvested cane is chopped and milled to extract the maximum amount of sugar. This sugar is fermented by yeast to form ethanol. The remainder of the sugarcane consists mostly of bagasse (the woody part of the cane), which is dried and burned to heat the boilers and produce electricity for the factory, and in some cases to feed electricity into the local electrical grid.

2.4 2nd-Generation Bioethanol Technology

Lignocellulosic ethanol promises a new future for bioethanol production. This fuel is produced from the most abundant raw material in nature, namely: lignocellulosic biomass (Lee, 1997). Lignocellulosic biomass includes; hardwood, softwood, grasses and agricultural residues, with additional raw materials of potential interest being newspaper, office paper and municipal waste (Lee, 1997).

The advantage of biofuels above fossil derived fuels is that the CO_2 emissions resulting from the burning of these fuels are reabsorbed by the next generation of plant feedstock from which they are produced. This effectively closes the carbon cycle, which would allow the transportation sector worldwide to become carbon neutral.

Lignocellulosic ethanol production requires an additional pretreatment process (Figure 2-5) to reduce the recalcitrance of the woody material to enable enzymatic access to the cellulose (Berlin *et al.*, 2006). This process breaks the natural bonds occurring in lignocellulosic biomass, allowing access to enzymes to attach and hydrolyse the cellulose and hemicellulose into free sugars, mostly glucose (Lynd *et al.* 2002). This is necessary as almost all woody biomass contains lignin, an extremely resistant aromatic structure that protects the plant from chemical and enzymatic degradation. The remaining sugars are finally fermentation by yeast or bacteria to form ethanol (Berlin *et al.*, 2006).

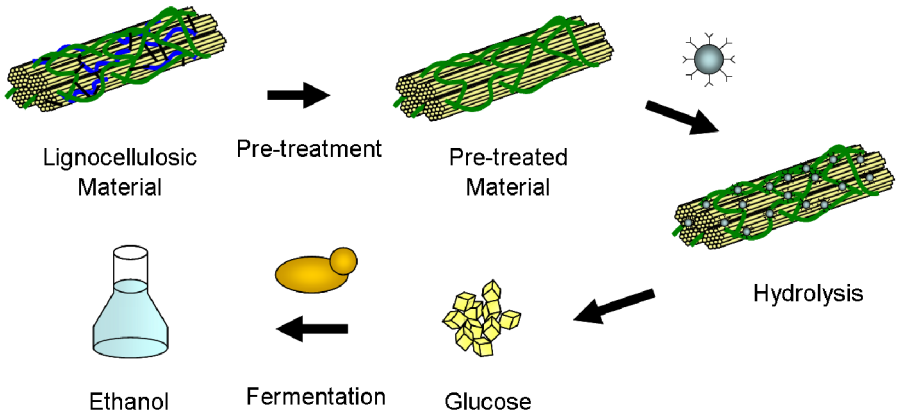

Figure 2-5: Second generation bioethanol production process

This second-generation technology increases the range of feedstock that can be used to produce ethanol and improve the efficiency of current feedstock utilised in the first generation technology by converting the cellulose and hemicellulose as well (Linde, 2008b). Cellulosic ethanol provides a further advantage over 1st-generation ethanol technology as it does not compete with food security or other agricultural produce, effectively eliminating the political "food versus fuel" debate which exist in many countries.

One challenge inhibiting the commercialisation of second-generation bioethanol is the procurement of financial investment to build a commercial-scale plant, which could cost billions of South African Rands (EIA, 2007). This is primarily due to the technology having not been proven at this scale, although currently multiple demonstration plants have been constructed to obtain experimental data on the scaling challenges and its effects on the performance of the plants. Thus methods are required to more accurately predict the performance of these large plants to enable better design strategies and reduce the risk for investors.

2.4.1 Structure of lignocellulosic biomass

Lignocellulose consists primarily of three components, namely; cellulose, hemicellulose and lignin (Figure 2-6). Cellulose is the major constituent of the plant cell wall and consists of unbranched polymers of glucose (Lee, 1997; Linde, 2008b), bundled tightly together to form an extremely strong structural support. Hemicellulose consists of heteropolymers, containing; xylose, arabinose, glucose, mannose and galactose sugars with the hemicellulose mostly comprises of xylan and glucomannan structures (Gírio *et al.*, 2010). Hemicelluloses has an amorphous structure, which is easily degraded. Lignin is a complex, variable, hydrophobic, cross-linked, three-dimensional aromatic polymer that binds the cellulose and hemicellulose together and provides the structural integrity of the plant, which is highly resistant to chemical and enzymatic degradation (Lee,

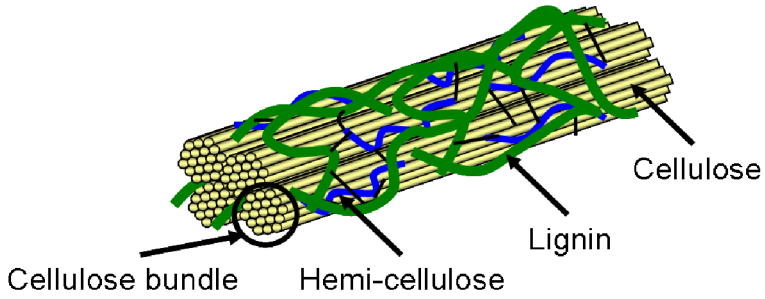

Figure 2-6: Simplified illustration of the lignocellulosic materials structure

1997). It is specifically due to the presence of lignin that it is necessary to pretreat lignocellulosic materials for optimal conversion.

2.4.2 Pretreatment

Disruption of the lignocellulosic biomass structure is done to liberate the cellulose and hemicellulose from their complex with lignin (Lee, 1997), granting chemical treatment or enzymes access to the cellulose and hemicellulose components. This is the current rate limiting process and most difficult problem to be solved (Lee, 1997).

There are multiple pretreatment methods available to disrupt the lignocellulosic biomass structure, including physical, chemical and biological:

- Physical pretreatment involves the reduction in substrate size and this is usually achieved by milling or aqueous / steam treatment. The advantage in damaging the substrate is that it ruptures and exposes more of the substrate for enzymatic hydrolysis.

- Chemical pretreatment methods include the use of dilute acid, alkaline, organic solvent (Berlin *et al.*, 2006), ammonia (NH_4), sulphur dioxide (SO_2), CO_2 and other chemicals to break open or increase the digestibility of the substrate for enzymatic hydrolysis.

- Biological degradation is achieved mainly by fungi, most efficiently by white-rot basidiomycetes, but also by certain actinomycetes (Lee, 1997). Studies have shown that several fungal enzymes can degrade lignin, including lignin peroxidase, Mn-dependent peroxidase and laccase (Lee, 1997).

2.4.3 Hydrolysis

Hydrolysis involves the depolymerisation of the carbohydrate polymers, cellulose, to produce free sugars for fermentation (Lee, 1997). Some micro-organisms including fungi and bacteria are capable of producing cellulase. The classical fungal cellulase system is an enzyme complex consisting of endoglucanase, exoglucanase and cellobiase (β-glucosidase) (Lee, 1997). Endoglucanase attacks random sites of the amorphous cellulose or at surfaces of microfibrils, while exoglucanase releases cellobiose from the reducing and non-reducing ends of cellulose. Cellobiase further hydrolyses the cellobiose and water-soluble cellodextrines to glucose (Lee, 1997). Crystalline cellulose is highly resistant to enzymatic attack and any bonds cleaved by the endoglucanase can readily be reformed. This requires the exoglucanase to remove the cellulose chain from the cellulose bundle and hydrolyse the chains into smaller oligosaccharides.

Anaerobic (without oxygen) thermophilic bacteria have several advantages over other anaerobic micro-organisms, such as high growth and metabolic rates on cellulose and enhanced stability of enzymes (Lee, 1997). Recently a series of genetically engineered bacteria have been developed that produce some enzymes required for hydrolysis of cellulose and efficiently ferment all sugar to ethanol (La Grange *et al.*, 2010).

2.4.4 Fermentation

Fermentation of hexose and pentose sugars released during the hydrolysis process produces ethanol. Fermentation of glucose as a carbon and energy source using bacteria or fungi has been well developed and documented (Lee, 1997). Xylose is known as a hardly fermentable sugar by micro-organisms and therefore the technology for utilizing xylose in enzymatic hydrolysis needs to be developed to enhance the overall conversion efficiency (Lee, 1997).

Currently, freely suspended yeast cells are commonly used in the ethanol production industry. These cells exit the bioreactors during continuous operation, unless separated with a centrifuge and partly returned to the bioreactors (Ge, 2006). The biggest advantage of using self-flocculating yeast strains is that much higher yeast cell densities can be obtained without additional expenses in terms of energy consumption and capital investment (Ge, 2006). Ge (2006) developed and experimentally verified an intrinsic kinetic model for a flocculating fusant yeast strain SPSC01.

2.5 Viscosity

Viscosity plays an important role in selecting and designing mixing vessels, as viscosity influences the shear rates and fluid dynamics of the system. In general, low viscosity fluids require less energy and power to agitate, compared to more viscous fluids. When particles are present, it is important to maintain a fully

suspended particle distribution to maximise the surface contact with the rest of the mixing fluid.

Dynamic viscosity (μ) is defined as the relationship between shear stress (τ) and the strain rate ($\dot{\gamma}$) experienced by a fluid:

$$\tau = \mu \dot{\gamma} \quad . \tag{2-1}$$

Kinematic viscosity (ν) is the ratio between the dynamic viscosity and fluid density (ρ) and is often used in thermodynamic and fluid dynamic dimensional analysis and sometimes referred to as the diffusivity of momentum:

$$\nu = \frac{\mu}{\rho} \quad . \tag{2-2}$$

An important relationship often exploited in rheological studies is the correlation between torque and viscosity for rotation between two concentric cylinders (White, 1991) given by:

$$M = 4\pi\mu \frac{r_o^2 r_i^2}{r_o^2 - r_i^2} (\omega_o - \omega_i) \quad . \tag{2-3}$$

Where r_o and r_i are the radius of the outer and inner cylinders, respectively and ω_o and ω_i the rotational speeds of the outer and inner cylinders, respectively.

Another interesting physical anomaly observed when two concentric cylinders rotate with respects to each other is the appearance of Taylor vortices (White, 1991). These vortices occur as counter rotating circumferential rings due to instabilities in the flow at Taylor numbers greater than $Ta \approx 1\,700$ for small clearance conditions (r_o-r_i) << r_i, calculated using:

$$Ta = r_i (r_o - r_i)^3 \frac{\omega_i^2}{\nu^2} \approx 1\,700 \quad . \tag{2-4}$$

It is thus important to ensure that this condition is not violated in order to obtain accurate viscosity readings.

2.6 Computational Fluid Dynamics

Computational fluid dynamics (CFD) is an engineering tool used to provide predictions of thermodynamic and fluid flow cases and has many applications in engineering, including the prediction of aerodynamics around aircraft and motor vehicles, combustion processes, heat transfer, mixing (Meroney and Colorado, 2009; Jahoda *et al.*, 2009), environmental forecasts and much more (Versteeg and Malalasekera, 1995).

The focus of this study is the modelling of a 1.3 L stirred tank fermenter for the prediction of microcrystalline cellulose particle distribution. Particle distributions

play an important role within reactors as it influences the biological reaction rates (Hristov *et al.*, 2004). This is primarily due to all particle related reactions taking place on the particle surfaces. Fully suspended particles therefore provide the maximum surface exposure, and consequently optimal reaction rates.

Various studies have been conducted involving multiphase flow systems in stirred tank mixers. Armenante *et al.* (1997) conducted a study to compare the validity of CFD to predicting the flow field and turbulent properties in a stirred tank using the algebraic stress model (ASM) and the standard k-ε model to predict turbulence. The results indicated that CFD was capable of capturing the qualitative features of the flow field and turbulence, with the ASM model providing the best results. Multi-stage impeller mixing studies have been performed which promote easier heat removal, better gas attention, less variable shear rates in the liquid and more compact equipment (Alliet-Gaubert *et al.*, 2006 and Montante and Magnelli, 2004).

CFD is used to investigate various multiphase conditions including fluidised beds (Syamlal and O'Brien, 1988 and Ahuja and Patwardhan, 2008), fluid-solid mixers (Ng *et al.*, 2009), particle distributions in rooms, combustion of fuel particles, and free-surface simulations. There are primarily three methodologies to modelling multiphase flows, namely; volume of fluid (VOF), Lagrangian and Eulerian. The simplest of these is the VOF model. These simulations require a single set of momentum equations and assume that the pressure and velocity fields of both fluids in a volume are equal. As the name of the model suggests, all mixture properties and surface interface effects are calculated from the volume fraction occupied by each species. These models are however limited to immiscible liquids or gases and are inappropriate for modelling solid particles.

Modelling solid particles in a fluid flow field requires one of two approaches. The first approach is the Eulerian - Lagrangian technique whereby the solid particles are modelled as individual spherical particles in the flow. These particles are transported through the flow field based on the pressure and drag forces exerted upon each particle parcel. These models mimic spherical particle flows very accurately but are limited in the practical number of particles that can be tracked by the computational power and memory available. The second approach is the Eulerian - Eulerian method whereby each fluid or particle species is modelled separately including its own set of momentum equations with the assumption that each phase experiences the same pressure within each volume. These models require a further set of source terms to describe the interaction forces such as drag and lift as well as set of internal forces for the solid phase.

These internal forces can essentially be replaced with a solid pressure force which limits the particle compaction (Dong and Yu, 2009). A recent development in particulate multiphase flow is the use of granular stress models. These models have primarily been developed for fluidised beds and flows where the internal forces of the solids dominated the flow. They were developed for particles, which can be approximated as spheres and include the solid pressure force and the

colloidal and kinetic frictional forces. They have a great advantage when modelling conditions such as for example fluidised beds, sand sedimentation or the movement of sand dunes due to wind forces.

2.7 Literature Summary

Literature indicates that CO_2 is one of the major contributors to the global climate change phenomenon, with the transportation sector responsible for approximately 20 % of the total CO_2 emissions worldwide. Further it was suggested that fossil fuel reserves are rapidly diminishing. The combination of these two phenomenons urged scientists to investigate alternative transportation fuels.

Biofuels provides a viable alternative to fossil fuels, with the added advantage of reduced atmospheric CO_2 emissions. CO_2 emissions resulting from the burning of biofuels are reabsorbed by the next generation of plant feedstock used to produce the fuel, thus effectively closing the carbon cycle. This would allow the transportation sector worldwide to become effectively carbon neutral.

Bioethanol was discussed in terms of 1st and 2nd generation technology with further discussion focused on the latter. Lignocellulosic materials and the process required for the conversion thereof to ethanol is described in terms of pretreatment, hydrolysis and fermentation. The role viscosity plays in mixing tank design and operation were also discussed.

CFD was identified as a potential tool to evaluate, at least qualitatively, the prevailing fluid flow fields and particle distributions within any flow domain. Models including the Eulerian-Eulerian segregated models coupled with a solid pressure force allows the simulation of inter-penetrating fluid species such as particles in a fluid along with the particle distribution and settling density.

3 KINETIC MODEL FOR SSF OF AVICEL

3.1 Abstract

This chapter describes development of a kinetic model required for predicting simultaneous saccharification and fermentation of Avicel, an insoluble crystalline cellulose polymer for use in a CFD environment. Separate anoxic cultivations of 40 g/L glucose and 100 g/L Avicel were conducted to verify model predictions and obtain parameters to describe the reaction kinetics. Saccharification of Avicel was achieved with *Trichoderma reesei* cellulases from the enzyme preparation Spezyme CP with an enzyme loading of 10 FPU/g cellulose. Cultivations were supplemented with 50 IU/g cellulose of β-glucosidase from Novozym 188 to prevent product inhibition by cellobiose. *Saccharomyces cerevisiae,* also known as bakers yeast, is often used in the food and wine sector and proven to be a robust organism under industrial conditions. *Saccharomyces cerevisiae* MH-1000 was selected for this study and used to ferment glucose to ethanol, glycerol and carbon dioxide. The numerical model presented in this thesis differs from previous models available in literature by separating the endoglucanase and exoglucanase enzyme kinetics and allowing for inhibitive site competition. Assuming all enzymes remain active and that each enzyme complex has a corresponding constant specific activity, the model is capable of predicting adsorbed enzyme concentrations with reasonable accuracy. Comparison of predicted values to experimental measurements indicated that the numerical model was capable of capturing the significant elements involved in the conversion of cellulose to ethanol.

3.2 Introduction

Cellulose is the most abundant carbohydrate polymer found on Earth (Walker and Wilson, 1991) and holds much promise as a sustainable energy source for the production of liquid fuel, food and chemicals (Lee and Fan, 1982). Cellulose is an insoluble, heterogeneous substrate requiring a variety of enzymes for hydrolysis (Lee and Fan, 1982). Initially, free enzyme molecules in the bulk solution adsorb to the cellulose surface forming an enzyme-substrate complex. The formation of these enzyme-substrate complexes allow the entry of water molecules into their active sites and the subsequent reaction with the cellulose molecules to form reduced sugars such as glucose and cellobiose. These sugars are released to the bulk aqueous medium where further decomposition of the cellobiose to glucose is catalysed by the enzyme β-glucosidase.

Various numerical models have been proposed to predict the complex enzyme kinetics responsible for the hydrolysis of cellulose to sugar and cellobiose (Converse *et al.* 1987, Gusakov and Sinitsyn 1985, Scheiding *et al.* 1984, Caminal *et al.* 1985, Converse and Optekar 1993). These models used either Langmuir isotherm or Michaelis-Menten type equations to model enzyme adsorption to cellulose (Zhang and Lynd, 2004). Michaelis-Menten based models have

successfully been used to model enzyme-cellulose interaction; however the fundamental assumptions of these models are based on homogeneous soluble substrates and are not entirely applicable to insoluble cellulose reactions. Langmuir isotherms account for enzyme interactions with heterogeneous insoluble substrates, but are not valid at all substrate concentrations.

The basis of modelling simultaneous saccharification and fermentation (SSF) of a substrate is formed by combining the adsorption model with the enzyme hydrolysis of cellulose and adding an organism to ferment the reduced sugars. Literature on SSF models is limited, however, South *et al.* (1995) proposed a model for the SSF of pretreated hard woods such as birch and popular based on a model developed by Phillippidis *et al.* (1992). South *et al.* (1995) assumed a Langmuir adsorption type behaviour to describe the substrate-enzyme interactions and proposed a diminishing substrate conversion rate (r_c) as a function of conversion (x) and enzyme occupied active sites (EC) on the cellulose surface:

$$r_c = \left(k_h (1-x)^{n_h} + c_h\right) \times \frac{[EC]}{1+\sigma_c}, \tag{3-1}$$

with k_h, n_h and c_h empirical constants and σ_c the adsorption capacity of enzyme to the substrate. Shao *et al.* (2008) and Zhang *et al.* (2009) proposed similar models for paper sludge. Parameters for adsorption and substrate conversion rates for these models were estimated empirically from experimental measurements. The remaining rate equations and parameters describing the conversion of cellobiose to glucose and subsequent fermentation of glucose to ethanol were obtained from literature.

A kinetic model for predicting SSF of Avicel, an artificial microcrystalline cellulose polymer is described in this chapter. It utilizes dynamic adsorption models similar to that used by Shao *et al.* (2008) to describe the adsorption behaviour of the cellulase enzymes, but differs from Shao's model by accounting for enzyme competitive inhibition. The model described in this work also assumes a constant specific enzyme activity which could provide improved approximations to experimentally determined values. Fermentation products from glucose were extended to include the production of glycerol which becomes significant at higher substrate loads. This model was developed for implementation alongside design codes, including CFD, to improve plant performance predictions and design parameter estimation.

3.3 Materials and Methods

3.3.1 Strain and culture medium

Saccharomyces cerevisiae

S. cerevisiae MH-1000 selected for this study is a robust in-house yeast strain, used for the conversion of glucose to ethanol. This strain was preserved at -80 °C in the presence of 15 % glycerol in 0.5 mL aliquots. Prior to each cultivation, a single aliquot was rapidly thawed and a loop full of culture was streaked on YPD agar plates consisting of 10 g/L yeast extract, 20 g/L peptone, 20 g/L glucose and 20 g/L agar. The agar plates were subsequently incubated at 30 °C for 48 h.

Glucose fermentations medium

Synthetic complete (SC) medium was prepared by dissolving 6.8 g Yeast Nitrogen Base (YNB) without amino acid and ammonium sulphate supplementation (Difco, Becton Dickinson and Company) and 20 g $(NH_4)_2SO_4$ into reverse osmosis-purified H_2O to a volume of 1 L. The pH of the medium was adjusted to a value of 5.5 using 3 mol/L of KOH. Of this mixture 400 mL was added to each reactor, with the remaining volume devided equally between eight 250 mL Erlenmeyer flasks. After 80 g of anhydrous glucose (Merck Chemicals KGaA, Darmstad, Germany) was dissolved in reverse osmosis-purified H_2O to a volume of 500 mL, 200 mL quantities were transferred to two 500 mL Buchner flasks, with the remaining volume kept separately in a 250 mL Erlenmeyer flask. The reactors and flasks were sealed and the medium and glucose autoclaved for 20 min at 121°C. The sterilized glucose solution was added aseptically to the reactors and flasks. Subsequently, 4 mL of a vitamin and trace element solution, prepared according to the method of Verduyn *et al.* (1992), was sterilized by filtration through 0.20 µm cellulose acetate filters (Gema Medical S.L., Spain) and added aseptically along with sterilized water to the flask and reactors to a total volume of 50 mL and 800 mL, respectively. For anoxic cultivations in bioreactors, 1.344 g Tween 80 and 0.032 g ergosterol were added to the filter-sterilized vitamin and trace element solution. Ergosterol was first dissolved in 5 mL pure ethanol before addition of water. This ethanol was compensated for in all calculations. Each reactor contained a total of 800 mL culture medium.

Avicel hydrolysis and fermentation medium

Culture medium for the pre-culture flasks was prepared as indicated by the glucose medium preparation. SC medium used for Avicel cultivations was prepared similar to the method described for the glucose fermentation medium, and consisted of 400 mL volumes containing 4.76 g YNB without amino acid supplementation and 14 g $(NH_4)_2SO_4$ dissolved in reverse osmosis-purified H_2O with 80 g Avicel PH-101 (Fluka Analytical, Ireland) added to each reactor. The pH was adjusted to a value of 5.5 using 3 mol/L of KOH and autoclaved along with the glucose flasks for 20 min at 121 °C. Subsequently, 5.6 mL of the vitamin

and trace element solution was filter-sterilized with 0.056 g ergosterol and 2.35 g Tween 80 and equally divided and added aseptically to the reactors. Total reactor volumes were 600 mL before inoculation.

3.3.2 Enzymes

Spezyme CP (Genencor, Finland) which contains cellulolytic enzymes produced by *Trichoderma reesei* served as a source of cellobiohydrolase and endoglucanase. β-glucosidase (Novozym 188, Novozymes, Denmark) was added to prevent product inhibition. Filter paper units and cellobiose units were calculated using assay methods prescribed by Ghose (1987). β-glucosidase activities were measured using p-nitrophenyl-β-D-glucopyranoside (pNPG) described by van Rooyen *et al.,* (2005). Determination of endoglucanase activities was based on the carboxyl-methyl-cellulose (CMC) assay described by Bailey (1992) for xylanase determination. This method was adapted by increasing the incubation time from 5 min to 30 min for sufficient conversion of cellobiose to glucose to occur. Exoglucanase activities were determined using the assay described by Den Haan *et al.* (2007), using Avicel as substrate and measuring the reduced sugars using 3,5dinitrosalicylic acid (DNS). Assays were conducted in 96-well plates to facilitate high throughput of samples. Protein concentrations were determined using the standard Bicinchoninic acid (BCA) protein assay (Novagen, Darmstadt, Germany) and correlated with the enzyme mixture activities according to the protein composition presented by Goyal *et al.* (1991).

3.3.3 Cultivations

Pre-culture

Yeast cells grown from YPD agar plates were used to inoculate 250 mL Erlenmeyer shake flasks containing 50 mL of SC medium supplemented with 40 g/L of glucose as carbon source. After a period of 24 h at 30 °C on a shaking incubator set at 100 rpm, the inoculum was prepared by transferring 10 mL of this culture to a second flask containing the same medium and incubated until early stationary phase (approximately 18 h).

Glucose fermentation

Bioreactor vessels containing 40 g/L of glucose were inoculated to an absorbance of 0.1 units measured at 600 nm (OD_{600}). Samples were drawn at regular 1 hour intervals until the early stationary growth phase. This phase is signified by the absence of available glucose and subsequent ceased yeast growth.

SSF of Avicel

10 FPU/g cellulose of Spezyme CP and 50 IU/g cellulose of Novozym 188 were prepared in citrate buffer pH 5.5 and filter sterilized through 0.20 µm cellulose acetate filters. This was added aseptically to each reactor, bringing the total reactor volume to 800 mL. Inoculation was done to an OD_{600} of 0.1 units yeast

calculated from the pre-culture. Samples were drawn initially at 4 hour intervals for a total of 18 h, followed by 12 h intervals for a total of 112 h.

All cultivations were performed in 1.3 L Bioflow 100 bioreactors (New Brunswick Scientific, New Jersey) at 30 °C with agitation achieved by a Rushton type impeller set at 150 rpm. All cultivations were performed in quadruplicate.

3.3.4 Analysis

Dry Mass Determination

Dry biomass concentrations from cultures grown on 40 g/L glucose were determined by washing and filtering 10 mL samples through a Gooch filter fitted with GF/A grade glass microfiber filters (Whatman International Ltd, England). Filters were dried in a microwave oven for 10 min (700 W at 35 % power), cooled to room temperature and measured using an analytical balance. The optical density and cell counts determined from dilutions of the glucose fermentation sample allowed construction of a standard curve that was used to relate the biomass concentration to cell counts for use with SSF experiments.

Medium Concentrations

Glucose, glycerol and ethanol concentrations were determined using a high performance liquid chromatograph (Thermo Fisher Scientific, Finnigan Surveyor, USA), fitted with a Rezex RHM-Monosaccharide H+ (8 %) (Phenomenex, USA) column and adjusted to a temperature of 60 °C and flow rate of 0.6 mL/min. Milli-Q water served as the mobile phase during all analyses. Residence time and peak information were recorded using Comquest 4.2 (Thermo Fisher Scientific, USA) software.

Substrate Conversion

Avicel conversion was determined by washing the remaining insoluble pellets from each sample 3 times with distilled water to remove residual and unbound enzymes as well as other soluble components from the cellulose. Microfuge tubes (1.5 mL) were dried in an oven at 105 °C, cooled to ambient temperature and weighed. Washed samples (1 mL) were added to each centrifuge tube, dried to a constant weight in an oven at 105 °C, and cooled to ambient temperature. Avicel dry weight was calculated by subtracting the yeast dry weight mass, determined from cell count information, from the dry pellet mass in the centrifuge tubes.

3.3.5 Modelling

MATLAB R2007a Student Edition (The MathWorks, Inc, USA) was used to model the reaction kinetics. Reaction rates were solved iteratively at each time-step, updating the variables once convergence was achieved. Parameters were estimated using a best-fit approach with initial values selected from literature and iteratively adjusted to obtain the most accurate correlations (Appendix E). Final

parameters were selected based on an overall minimum error for each component simulated. A sensitivity analysis was conducted on these modified parameters with specific focus on the percentage change on the final ethanol concentration (Table 3-3).

The numerical model for simultaneous saccharification and fermentation of crystalline cellulose was based on work done by South *et al.* (1995) with regard to the simplicity of the model. The model assumes the following pathway from substrate to product:

Endoglucanase and exoglucanase enzymes adsorb to the insoluble Avicel particle surface forming enzyme-substrate complexes $[EC]_{endo}$ and $[EC]_{exo}$. The rate of formation of these bonds is described by dynamic adsorption type equations:

$$\frac{d[EC]_{endo}}{dt} = \frac{d[C]_{endo}}{dt}(1+\sigma_{endo}) + k_{fc}[E_{f,endo}][C_{f,endo}](1+\sigma_{endo}) - \frac{k_{fc}}{K_{endo}}[EC]_{endo} \quad \text{and} \tag{3-2}$$

$$\frac{d[EC]_{exo}}{dt} = \frac{d[C]_{exo}}{dt}(1+\sigma_{exo}) + k_{fc}[E_{f,exo}][C_{f,exo}](1+\sigma_{exo}) - \frac{k_{fc}}{K_{exo}}[EC]_{exo} \quad , \tag{3-3}$$

which correlate adsorbed enzymes with the conversion rate of the substrate. Where K_{endo} and K_{exo} are adsorption affinity constants and the free enzymes $[E_f]$ and free cellulose $[C_f]$ are determined by:

$$[E_f] = [E_T] - \frac{[EC]\ \sigma_c}{(1+\sigma_c)} \quad \text{and} \tag{3-4}$$

$$[C_f] = [C_T] - \frac{[EC]}{(1+\sigma_c)} \quad , \tag{3-5}$$

respectively, with σ_c the maximum enzyme capacity of the substrate.

Hydrolysis of cellulose consisting of amorphous and crystalline structures are determined as a function of adsorbed enzyme [EC] to the substrate and the enzyme specific activity (k_{endo} and k_{exo}):

$$\frac{d[C]_{endo}}{dt} = -k_{endo}\left(\frac{[EC]_{endo}}{1+\sigma_{endo}}\right)\left(\frac{K_{C\_Cb}}{[Cb]+K_{C\_Cb}}\right)\left(\frac{K_{C\_Eth}}{[Eth]+K_{C\_Eth}}\right) \tag{3-6}$$

$$\frac{d[C]_{exo}}{dt} = \tanh\left(\frac{t}{\tau_c}\right) - k_{exo}\left(\frac{[EC]_{exo}}{1+\sigma_{exo}}\right)\left(\frac{K_{C\_Cb}}{[Cb]+K_{C\_Cb}}\right)\left(\frac{K_{C\_Eth}}{[Eth]+K_{C\_Eth}}\right), \quad (3\text{-}7)$$

with inhibition by cellobiose and ethanol calculated from Phillippidis *et al.* (1992).

For simplicity it was assumed that cellulose chains were converted to cellobiose only by exoglucanase. This conversion of cellulose to cellobiose was modelled proportionally to the cellulose hydrolysis rate, whereas conversion of cellobiose to glucose was modelled using Michaelis-Menten kinetics:

$$\frac{d[Cb]}{dt} = -\frac{342}{324}\frac{d[C]}{dt} - \frac{K_{Cb}[Cb][B]}{K_m\left(1+\frac{[G]}{K_{Cb\_G}}\right)+[Cb]}, \quad (3\text{-}8)$$

as described by Phillippidis *et al.* (1992).

Hydrolysis of cellobiose [Cb] to glucose by β-glucosidase and the glucose [G] utilization by the yeast cells [X] can be described by:

$$\frac{d[G]}{dt} = \left(-\frac{342}{324}\frac{d[C]}{dt} - \frac{d[Cb]}{dt}\right)\frac{360}{342} - \frac{1}{Y_{X\_G}}\frac{d[X]}{dt}. \quad (3\text{-}9)$$

The fermentation of glucose to ethanol, carbon dioxide and glycerol was modelled as an anaerobic batch process following the stoichiometric approximation (Albers *et al.* 2002) that describes the catabolic conversion of glucose as:

$$C_6H_{12}O_6 + 0.2\,H_2 \rightarrow 1.8\,(C_2H_6O + CO_2) + 0.2\,C_3H_8O_3. \quad (3\text{-}10)$$

Therefore, the yeast growth rate and product production rate for ethanol [Eth], carbon dioxide [CO_2] and glycerol [Gly] can be described by equations:

$$\frac{d[X]}{dt} = \frac{\mu_{max}[X][G]}{[G]+K_G}\left(1-\frac{[Eth]}{K_{X\_Eth}}\right), \quad (3\text{-}11)$$

$$\frac{d[Eth]}{dt} = \left(\frac{Y_{Eth\_G}}{Y_{X\_G}}\right)\frac{d[X]}{dt}, \quad (3\text{-}12)$$

$$\frac{d[CO_2]}{dt} = \left(\frac{Y_{CO2\_G}}{Y_{X\_G}}\right)\frac{d[X]}{dt} \text{ and} \quad (3\text{-}13)$$

$$\frac{d[Gly]}{dt} = \left(\frac{Y_{Gly\_G}}{Y_{X\_G}}\right)\frac{d[X]}{dt}, \quad (3\text{-}14)$$

respectively.

3.4 Results

3.4.1 Glucose fermentations

To verify the fermentation model for *S. cerevisiae,* anoxic fermentations were conducted at a glucose concentration of 40 g/L and compared to the numerical model predictions (Figure 3-1). The utilization (Equation 3-11) and conversion of glucose by the yeast to form ethanol, glycerol and carbon dioxide (Equations 3-12, 3-13, 3-14) was modelled assuming a stoichiometric approximation described by Equation 3-10. Glucose was found to be the primary growth-limiting nutrient, since culture growth and product formation ceased once this carbon source was depleted. The maximum growth rate (μ_{max}) for this organism was calculated to be 0.38 h^{-1}.

Measured ethanol concentrations reached approximately 14.6 g/L (72 % of the theoretical maximum). The numerical model, however, predicted a final ethanol concentration of 16.19 g/L. A carbon balance was performed on the experimental results, which indicated that 96.36 % ± 0.24 % of the carbon from the glucose was found in the fermentation products and biomass.

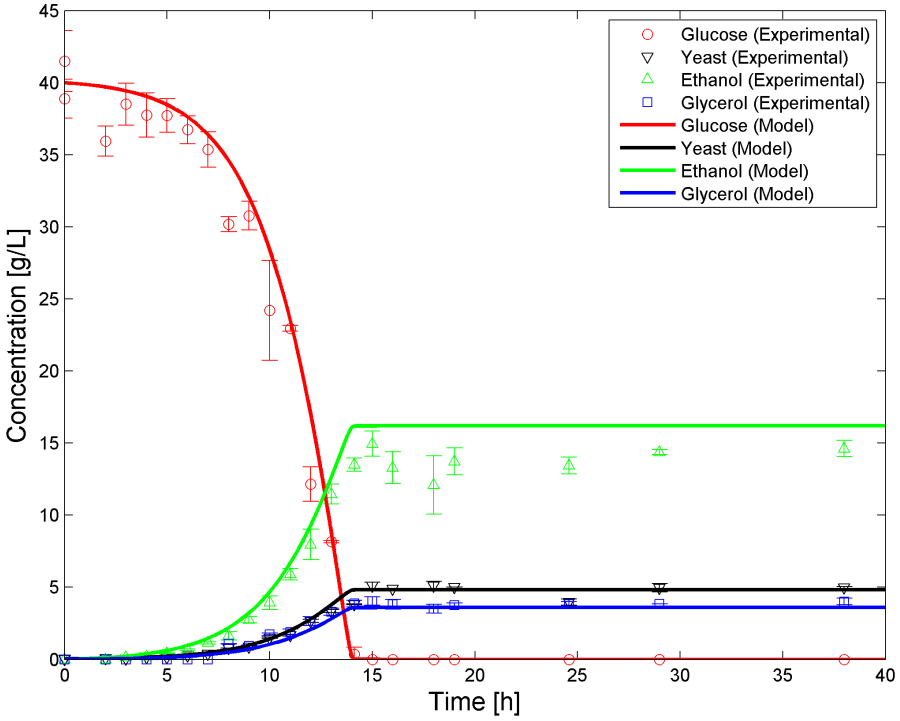

Figure 3-1: Glucose fermentation by *S. cerevisiae*

3.4.2 Enzyme activities

Ooshima *et al.* (1990) showed that the activity of an enzyme in solution is proportional to its protein concentration. Consequently, the protein concentration of adsorbed enzymes can be calculated from the difference between the experimentally-determined activities of the added and free enzymes in the broth based on the protein composition by Goyal *et al.* (1991). This assumes that all the cellulase enzymes are active and have a constant specific activity (Erikson *et al.*, 2002).

The enzyme activities and protein concentrations of Spezyme CP and Novozym 188 are summarized in Table 3-1. These values were used to estimate the added enzyme component in the medium. According to Goyal *et al.* (1991), 80 % of the protein in a mixture derived from *Trichoderma reesei* such as Spezyme CP was identified as exoglucanase, whereas 12 % was found to be endoglucanase. Filter paper units (FPU) and cellobiose units (CbU) were used to standardize and correlate the enzyme loading with values obtained from literature.

Table 3-1: Enzyme activities for Spezyme^{CP} and Novozyme 188

Enzyme Preparation	FPU [U/mL]	CbU [U/mL]	Endoglucanase [IU/mL]	Exoglucanase [IU/mL]	β-glucosidase [IU/mL]	Protein [mg/mL]
Spezyme^{CP}	64.5	N/A	14.07	0.022	2.09	195.4
Novozyme 188	N/A	586.2	0.18	N/A	6.18	148.06

Calculating the total enzyme protein added to each reactor for a cellulase loading of 10 FPU/ g cellulose and a β-glucosidase loading 50 CbU/g cellulose amounts to a total initial concentration of 0.39 g/L endoglucanase, 2.59 g/L exoglucanase and 1.35 g/L of β-glucosidase.

3.4.3 Enzymes adsorption to Avicel

Avicel can be divided into containing endoglucanase and exoglucanase bonding sites. The endoglucanase site consists of long less dense packed chains of cellulose with no exposed ends. These chains are randomly cut by the endoglucanase enzyme (Equation 3-6) to creating new chain ends. Exoglucanase attaches to these ends and proceeds to hydrolyze the remaining densely packed chains into reduced sugars, primarily cellobiose (Equation 3-7). Both these regions are assumed to always be present in Avicel. An initial distribution of endoglucanase and exoglucanase bonding sites was estimated by best fit to the initial experimental measured adsorbed enzyme concentrations and bonding capacity (Kumar and Wyman, 2008) and found to be 55 % and 45 % respectively.

Adsorbed protein concentrations for endoglucanase and exoglucanase enzymes were calculated by subtracting the experimentally-determined free enzyme activity in the broth from the theoretical total enzyme activity initially added (Figure 3-2). Experimental measurements further indicated that negligible amounts of β-glucosidase were adsorbed (data not shown).

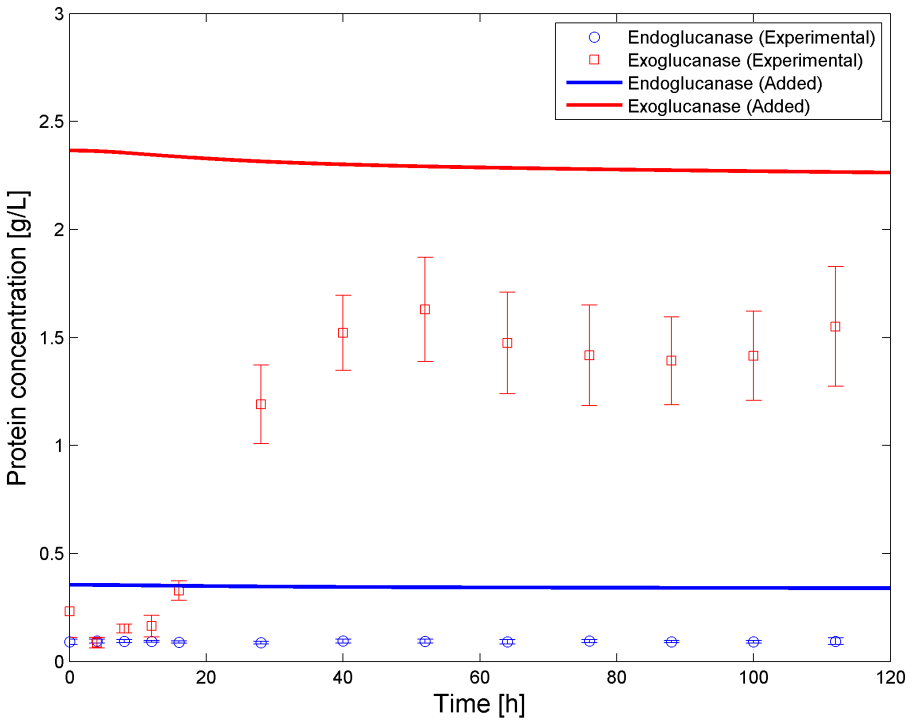

Figure 3-2: Free cellulase concentrations relative to initial enzyme loading

The calculated adsorbed enzyme concentrations (Figure 3-3) indicate that adsorbed endoglucanase remained relatively consistent throughout the fermentation. Adsorbed exoglucanase protein concentrations showed a considerable (5-fold) decrease from approximately 2.4 g/L to around 0.83 g/L after approximately 20 h (Figure 3-3). Adsorption of endoglucanase and exoglucanase to Avicel was modelled using dynamic adsorption models (Equations 3-2 and 3-3). With the assumed initial available site distribution of Avicel, the model could be used to predict the significant decrease in adsorbed exoglucanase and further agreed with the near constant adsorbed endoglucanase concentration.

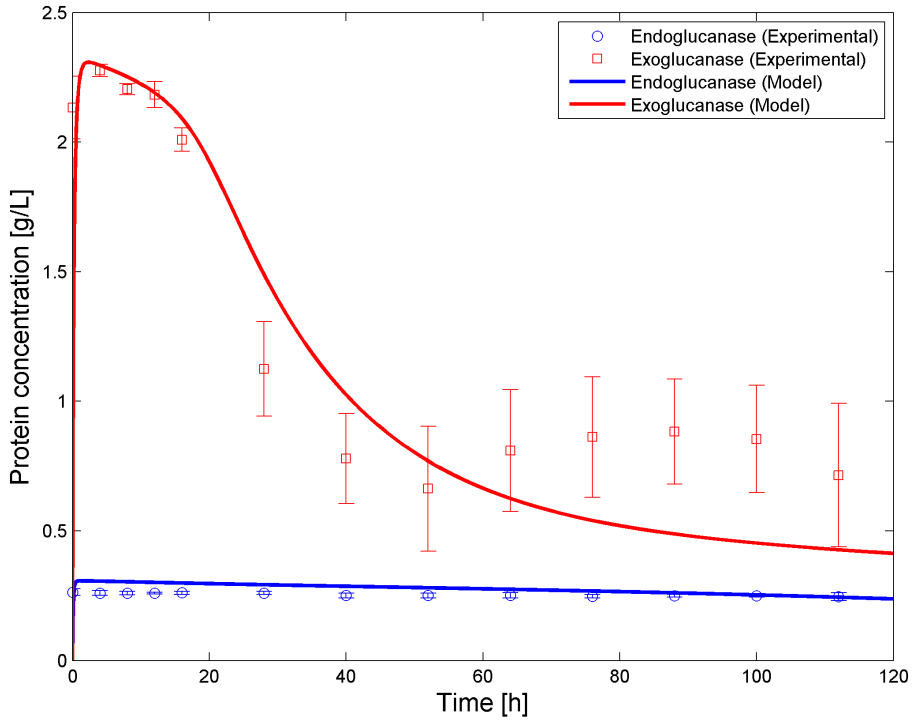

Figure 3-3: Adsorbed cellulase concentrations

However, the adsorption models could not be used to predict the apparent increase in adsorbed exoglucanase recorded after approximately 55 h. This apparent trend of increased adsorption was found to be inconclusive as a result of the large scatter on the experimental measurements.

3.4.4 SSF of Avicel

SSF of 100 g/L Avicel supplemented with Spezyme CP and Novozym 188 was conducted to verify the numerical model. Experimental results (Figure 3-4) show that after 112 h, approximately 72.6 % of the Avicel was converted to ethanol, glycerol, CO_2 and yeast biomass. Furthermore, there appears to be a delay in the initial conversion of the Avicel (first 8 h) after which it is converted at a significantly higher rate. The numerical model accounts for this delay in enzymatic conversion by enforcing a ramping function $\tanh(t/\tau_c)$ to the exoglucanase reaction rate. The maximum error between the predicted and experimental values was 3.8 %.

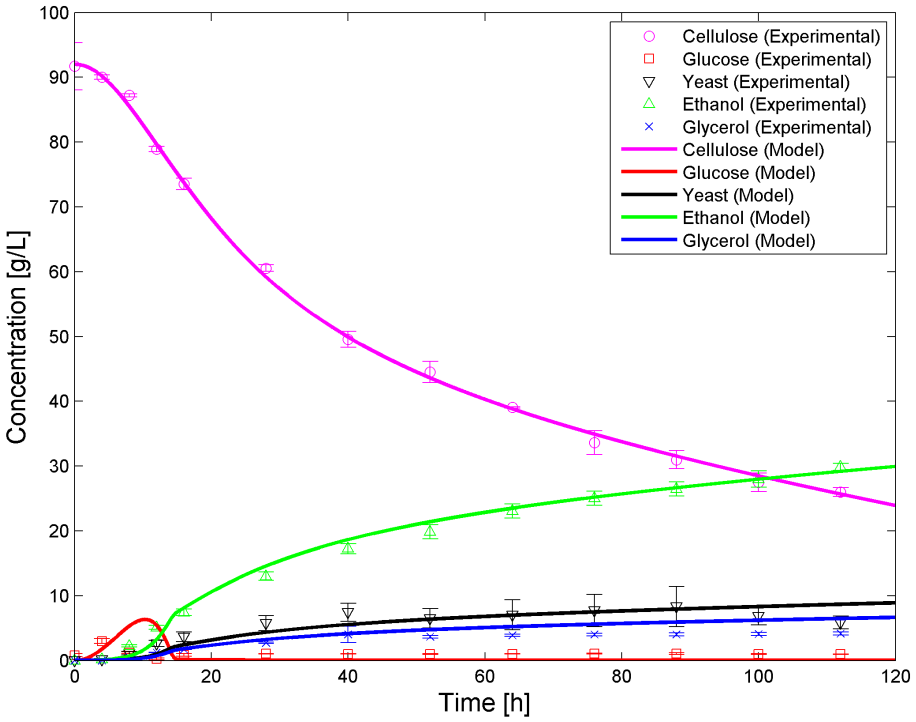

Figure 3-4: Avicel enzymatic hydrolyses and fermentation by *S. cerevisiae*

HPLC measurements indicated no trace of soluble cellobiose accumulation during the experiment indicating that all cellulose was fully converted to glucose and fermented. The numerical model correctly predicts this rapid hydrolysis of cellobiose to glucose by β-glucosidase (Equation 3-8).

A small glucose peak of approximately 3 g/L was detected at approximately 4 h, rapidly decreasing to approximately 1 g/L for the remainder of the experiment. The numerical model however predicts a glucose peak of 6.3 g/L at 10 h before the fermentation thereof by the yeast (Equation 3-9) decreases the concentration to 0 g/L.

Parameter fitting was performed on the remaining model constants for the SSF of Avicel (Equations 3-2 to 3-14). These values are presented in Table 3-2, with the specific hydrolyses rates k_{endo}, k_{exo}, equilibrium constant K_{exo} and the yields Y_{CO2_G}, Y_{Eth_G} and Y_{Gly_G} determined empirically in this study. The sensitivity analysis (Table 3-3) indicated that the maximum enzyme capacity σ_{exo} and reaction rate k_{exo} of the exoglucanase had the greatest influence on the hydrolysis rate of cellulose, while the maximum ethanol yield from glucose Y_{Eth_G} and ethanol inhibition constant could affect the maximum ethanol yield significantly. The remaining parameters had little or no effect on the final ethanol concentration, indicating that the model is insensitive to these parameters, therefore literature values were applied.

Table 3-2: Model constants for SSF of Avicel

Symbol	Value	Source
k_{endo}	0.110 h^{-1}	This Work
k_{exo}	0.07 h^{-1}	This Work
K_{endo}	1.84 L/g	Kumar and Wyman (2008)
K_{exo}	55 L/g	This Work
k_{fc}	1.8366 L/(g·h)	Shao *et al.* (2008)
K_{C_Cb}	5.85 g/L	Phillippidis *et al.* (1992)
K_{C_Eth}	50.35 g/L	Phillippidis *et al.* (1992)
K_{Cb}	0.02 g/(U·h)	Gusakov and Sinitsyn (1985)
K_{Cb_G}	0.62 g/L	Phillippidis *et al.* (1992)
K_G	0.476 g/L	Ghose and Tyagi (1979)
K_m	10.56 g/L	Phillippidis *et al.* (1992)
K_{X_Eth}	87 g/L	Ghose and Tyagi (1979)
Y_{CO2_G}	0.4	This Work
Y_{Eth_G}	0.419	This Work
Y_{Gly_G}	0.091	This Work
Y_{X_G}	0.12	Ghose and Tyagi (1979)
μ_{max}	0.4 h^{-1}	Ghose and Tyagi, (1979)
σ_{endo}	0.084	Kumar and Wyman (2008)
σ_{exo}	0.084	Kumar and Wyman (2008)
τ_c	8 h	This Work

Table 3-3: Sensitivity analysis for model parameters

Parameter	10 % decrease	10 % increase	50 % decrease	50 % increase
k_{endo}	3.238 %	3.085 %	17.63 %	13.76 %
k_{exo}	0.662 %	0.493 %	8.061 %	1.621 %
K_{endo}	0.580 %	0.495 %	4.455 %	1.920 %
K_{exo}	0.004 %	0.004 %	0.041 %	0.013 %
k_{fc}	0.057 %	0.047 %	0.512 %	0.173 %
K_{C_Cb}	0.012 %	0.010 %	0.101 %	0.036 %
K_{C_Eth}	1.072 %	0.927 %	7.855 %	3.661 %
K_{Cb}	0.012 %	0.010 %	0.100 %	0.036 %
K_{Cb_G}	0.007 %	0.006 %	0.058 %	0.021 %
K_G	0.002 %	0.001 %	0.009 %	0.006 %
K_m	0.011 %	0.010 %	0.054 %	0.051 %
K_{X_Eth}	0.002 %	0.001 %	16.55 %	0.003 %
Y_{CO2_G}	0.000 %	0.000 %	0.000 %	0.000 %
Y_{Eth_G}	9.078 %	8.934 %	47.10 %	43.41 %
Y_{Gly_G}	0.000 %	0.000 %	0.000 %	0.000 %
Y_{X_G}	0.004 %	0.004 %	0.025 %	0.018 %
μ_{max}	0.017 %	0.012 %	0.302 %	0.034 %
σ_{endo}	2.692 %	2.431 %	15.57 %	9.960 %
σ_{exo}	0.083 %	0.094 %	0.234 %	0.516 %
τ_c	0.051 %	0.050 %	0.264 %	0.240 %

3.5 Discussion

3.5.1 Glucose fermentations

The maximum growth rate (μ_{max}) for *S. cerevisiae* MH-1000 was calculated to be 0.38 h^{-1}, which compares favourably with anaerobic growth rates of approximately 0.4 h^{-1} obtained from literature (Ghose and Tyagi, 1979).

Figure 3-1 indicates that glucose is the limiting factor for yeast growth and ultimately ethanol production. Discrepancies between the numerical predictions and experimental results of ethanol concentration (Figure 3-1) are partially due to ethanol evaporation in the reactor during the course of the experiment (approximately 0.2 g/L) and cell maintenance functions not included in the model (Nissen *et al.*, 1997). A carbon balance of 96.4 % was calculated for cultivations in this study. Furthermore, the stoichiometric approximation used in the numerical model captured the trends of the experimental results well.

3.5.2 Enzyme activities

Yeast fermentations were conducted at an optimal temperature of 30 °C, which ensured that the enzymes remained thermally stable (Erikson *et al.*, 2002). Ooshima *et al.* (1990) and Erikson *et al.* (2002) found that protein enzymes in solution remain active and that the primary cause of reduced activity occurs on the substrate surface because enzymes become entrapped.

It is necessary to note that it was assumed that the difference between the added and free enzymes is equal to the number of enzymes adsorbed to the Avicel (Figure 3-2) based on findings by Ooshima *et al.* (1990). This assumption is reasonable, as a control test verified that negligible quantities of the enzyme adsorbed to the glass and metal surfaces within the reactors. The small amount of enzymes adsorbed to the fermenter surfaces is however further reduced as particulates within the reactor continuously knock these enzymes from the surface, either releasing them back into solution or allowing the enzyme to attach to the particle.

For the purpose of this study protein constituents for Spezyme CP were calculated from *Trichoderma reesei* studies performed by Goyal *et al.* (1991). This is however an approximation and additional analyses of the added enzymes are required to improve accuracy for both adsorbed protein concentrations and specific activities of these enzymes.

Determined enzyme preparation activities of the Spezyme CP compared favourably to values found from literature (Kumar and Wyman, 2008). Kumar and Wyman (2008) reported values of 59 FPU/mL and 123 mg/mL protein concentration, while the mixture used in this study measured 64.5 FPU/mL with a protein concentration of 195.4 mg/mL. A cellulase loading of 10 FPU/g cellulose was selected based on common practice from literature (Ramos *et al.*, 1993, Kaar

and Holtzapple , 2000) and to ensure that no cellobiose would accumulate in the reactors, which would severely inhibit the hydrolysis of Avicel, 50 CbU/g cellulose of β-glucosidase was added to the solution.

3.5.3 Enzyme adsorption to Avicel

Langmuir equations are often used to determine adsorbed enzymes to cellulose (South *et al.* 1995, Ooshima *et al.* 1990 and Scheiding *et al.* 1984). These equations require multiple iterations and are unsuitable for use with computational fluid dynamics software (Shao *et al.* 2008). Dynamic adsorption equations were thus adopted to model the enzyme-substrate bonding (Shao *et al.*, 2008).

The free cellulase enzymes in solution (Figure 3-2) indicate that nearly all exoglucanase enzymes initially adsorb onto the Avicel. After approximately 20 h these enzymes started dissociating back into solution. Approximately 75 % of the endoglucanase enzyme initially adsorbed onto the Avicel. This adsorbed concentration remained nearly constant throughout the fermentation. This may indicate that initially there were many available bonding sites for both enzymes on the Avicel surface. As the exoglucanase enzymes hydrolysed the long cellulose chains, the number of available active sites decreased causing the exoglucanase enzymes to disassociate back into solution. However, as only 75 % of the endoglucanase is adsorbed at any given time, it may indicate a limited number of exposed endoglucanase sites.

This behaviour could be explained by the synergism between endoglucanases and exoglucanases. Assuming an almost even distribution of endoglucanase and exoglucanase sites on the surface of Avicel, both enzymes readily bond to the active sites and start hydrolysing the cellulose. The endoglucanase thus quickly cut the exposed amorphous regions to form new reducing end for the exoglucanase, but constantly experience limited sites. As the exoglucanase enzymes cut the crystalline chains of cellulose, stripping them away from the substrate surface, new amorphous regions are exposed allowing the endoglucanase enzymes to move in and cut new active sites for the exoglucanase. The number of available ends for exoglucanase were therefore limited by the rate at which endoglucanase could provide new free ends. This limit in sites caused the excess exoglucanase to detach from the surface and return to solution.

The adsorbed cellulases calculated from the difference in total and free cellulase in solution was compared with predictions from the numerical model (Figure 3-3). The model used to predict adsorption was capable of capturing the trends measured experimentally, but tends to under-predict the adsorbed exoglucanase concentrations during the later stages of the fermentation. However, the model was used to predict the adsorbed endoglucanase concentrations with reasonable accuracy.

Conversion rates of Avicel were calculated using constant specific activities for the two enzymes (Figure 3-3). This suggests that Avicel reactivity is primarily a

function of available sites and competition between enzymes for these sites. From restart experiments, Yang *et al.* (2006) concluded that if Avicel is routinely stripped of enzyme and re-exposed to fresh enzyme cultures, the Avicel reactivity remains constant for substrate conversion of less than 70 %. This supports the theory of substrate conversion rates being influenced by the number of available sites on the substrate surface.

3.5.4 SSF of Avicel

The initial (<10 h) conversion rate of Avicel (Figure 3-4) is found to be significantly lower than expected. The delay may be a result of non-productive bonding by the exoglucanase enzymes with its reaction rate increasing as the endoglucanase enzymes cut available chains revealing more chain ends to which the exoglucanase enzyme can bond and initialise hydrolysis. This delay was accounted for in the numerical model by adding a ramp function ($\tanh(t/\tau_c)$) to the exoglucanase reaction rate. This initial delay in conversion rate, measured experimentally, explains the overestimation of the initial glucose peak predicted by the numerical model (Figure 3-4). This phenomenon requires further investigation to determine its precise cause.

The specific cellulase activities for converting Avicel (k_{endo}, k_{exo}), along with the enzyme equilibrium constant (K_{exo}) for exoglucanase, were determined by parameter fitting from the numerical model and required further experimentation to confirm.

Should this model be applied to a lignocellulosic substrate, various considerations are required: Firstly the presence of lignin in the fermenters will result in enzymes adsorbing to the lignin structure. Lignin can not be converted by endoglucanase or exoglucanase enzymes, resulting in the inactivation of these lignin adsorbed enzymes. This reduces the availability of especially the endoglucanase enzyme, requiring an increased initial loading to obtain similar performance.

Feedstock selection also determines the parameters for the kinetic model. Substrates containing less crystalline cellulose would be more reactive increasing the overall hydrolysis and hence conversion rate of the system. The primary parameters which would be affected are the enzyme activities for the endoglucanase and exoglucanase enzymes along with the initial crystalline and amorphous cellulose ratios present in the substrate.

3.6 Conclusion

A numerical model was presented to predict the conversion of Avicel to glucose and the fermentation thereof, and a model for predicting the adsorbed cellulase to the Avicel was provided. This model accounts for the synergistic effects between the endoglucanase and exoglucanase enzymes. It was proposed that the primary limiting factor in cellulose conversion is the availability of bonding sites. Both experimental measurements and numerical predictions indicated a significant decrease in adsorbed exoglucanase after 20 h. This was attributed to the depletion of free cellulose chain ends early (< 20 h) in the reactions.

4 VISCOSITY MODEL FOR SSF OF AVICEL PARTICLES

4.1 Abstract

Cellulose hydrolysis and fermentation have received an increasing level of attention over recent decades, with the primary focus on the development of improved enzymes and organism performance. Little literature is available on the effects of various fermentation components on the bulk viscosity of the fermentation broth for use in reactor design and use in fluid analysis software such as CFD. This study investigates density and settling properties of Avicel PH-101 particles and the effects of Tween 80, synthetic minimal medium, yeast concentration, oligosaccharides and cellulose particles on the apparent dynamic viscosity of the fermentation mixture. Viscosity measurements were obtained using a rotational rheology meter equipped with a DG 26.7 double gap concentric cylinder measuring system. Results indicated that Avicel particles experience nearly three-fold the drag force compared to similar sized spherical particles and have a measured density of 1 605.7 kg/m^3. Furthermore, Avicel particles contributed most significantly to the viscosity of a typical hydrolysis and fermentation broth. The Ostwald-de Waele formulation was used to describe the effects of these particles due to its shear-thinning nature. The correlation between the predicted particle effects and experimental results deviated with an average error of 11.1 %.

4.2 Introduction

Lignocellulosic bioethanol is a second-generation ethanol fuel technology approaching commercialisation. It has the potential to reduce world dependency on fossil fuels. This technology has many benefits over its first-generation counterpart. Most significantly it utilises cellulose, the most abundant renewable carbon resources on Earth, thereby eliminating the political debate on food versus fuel. Most literature on this technology primarily focuses on organism characteristics, enzyme development, kinetic models (Converse,1987; Caminal *et al.*,1984; South *et al.* 1995; Shao *et al.* 2008; Phillippidis *et al.*, 1992 and van Zyl *et al.*, 2010) and pretreatment processes (Ha et al., 2010; Kuo and Lee, 2009 and Coughlan, 1992). Limited literature is available on the properties of fermentation media (Converti *et al.*, 1999), especially cellulose particles (Staniforth *et al.*, 1988 and Luukkonen *et al.*, 2001), in terms of dynamic viscosity and particle properties.

Viscosity plays an important role in optimising mixing conditions, which in turn can improve reactions and fermentation processes by ensuring particle suspension and increased contact between constituents. It is imperative to understand that as reactions occur, the fluid dynamics of the system is affected, either improving or decreasing the efficiency of the system. There are many factors that influence the

dynamics of a particle-fluid system, including particle size, density, shape and volume fraction, fluid composition and temperature. All of these affect the viscosity which in turn determines agitation and turbulence intensity. Estimating the apparent dynamic viscosity of the fermentation media thus requires the knowledge and understanding of the effect of each component present in the mixture.

S. cerevisiae is widely used in the food and wine industry. Due to its industrial robustness, this fermenting microbe is ideally suited for the conversion of cellulose into ethanol. Various studies including Reuß *et al.* (1979), Malinowski *et al.* (1987) and Mancini and Moresi (2000) investigated the effects of yeast concentrations on the apparent dynamic viscosity of fermentation broths. Results from these studies indicate that high cell concentrations increase the bulk viscosity exponentially, and that pure yeast cultures display Newtonian type behaviour. In a typical saccharification and fermentation process, the effects of the base nutrients, yeast concentrations, oligosaccharides, surfactants, fermentation products such as ethanol and glycerol and feedstock are required for realistic estimations and simulations.

This study discusses the particle and fluid properties in a bioreactor during the simultaneous saccharification and fermentation of crystalline cellulose particles (Avicel PH-101, Fluka Analytical, Steinheim, Germany). This work focused on determining an average effective Stokes diameter which would capture the drag properties of Avicel particles and determine a correlation between the concentration of cellulose particles and effective viscosity of the bulk fluid. Furthermore, the effects of the base medium, oligosaccharides, Tween 80, ethanol and glycerol were investigated within the parameters of a typical batch fermentation configuration (van Zyl *et al.*, 2010) to determine the influence of these components on the dynamic viscosity. This model allows the estimation of the apparent dynamic viscosity of the reactor medium for use in commercial CFD codes.

4.3 Methods and Materials

4.3.1 Particle properties

The Avicel particle density (ρ_P) was required to determine particle drag characteristics and volume fraction. It was determined using Archimedes principle, where 20 g and 40 g of Avicel particles was added to a 500 mL measuring cylinder containing 300 mL of reverse osmosis (RO) water. Particles were agitated to ensure full suspension to fill all the surface air pockets before the displaced volume was measured. The particle density (ρ_P) was calculated using:

$$\rho_P = \frac{\text{Mass added}}{\text{Volume displaced}} . \tag{4-1}$$

The average settling terminal velocity ($V_{P,term}$) of Avicel particles were captured in

high definition video at 30 frames per second (fps) using a Sony HD video recorder (HDR-XR 100). Multiple samples were taken of Avicel particles settling in a 1.3 L measuring cylinder containing 1.3 L of RO water at room temperature (21 °C). The average settling velocity was determined by measuring the distance travelled in 10 frames for a sample size of 256 randomly selected particles. The frames used for analysis were captured using the open-source VLC media player 1.1.4 (VideoLAN, Paris, France). Image analyses was conducted with ImageJ 1.44c (National Institute of Health, USA), using its image overlay capabilities. Measurements were taken at a sufficient depth to ensure terminal velocity ($V_{P,\,term}$) was achieved, which was calculated with:

$$V_{P,\,term} = \frac{\text{Distance travelled}}{\text{Time}} . \tag{4-2}$$

Volume fractions for these experiments were kept very low to avoid particle interaction.

Avicel particles vary greatly in shape and size (Figure 4-1). For numerical modelling purposes, the particles were conveniently approximated as spheres using Stoke's Law:

$$D_{eff} = \sqrt{\frac{18\,\mu_w V_{P,\,term}}{\boldsymbol{g}\left(\rho_P - \rho_w\right)}} , \tag{4-3}$$

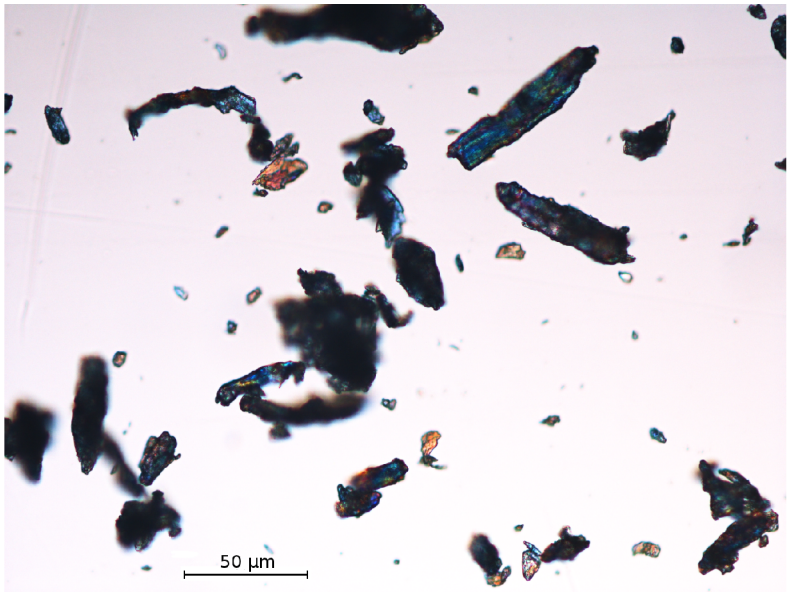

Figure 4-1: Avicel particles seen under a microscope at 400-fold magnification

to calculate an effective particle diameter (D_{eff}), which provided similar drag coefficients compared to the original particles. This approximation is only valid for Reynolds numbers:

$$Re_d = \frac{\rho_w V_{P,term} D_{eff}}{\mu_w} \tag{4-4}$$

of less than 1 (Çengel and Cimbala, 2006) to ensure particles remain within the creep flow regime.

4.3.2 Viscosity

Dynamic viscosity was measured using a Physica MCR 501 (Anton Paar, Österreich, Austria) viscometer with a DG 26.7 double gap measuring system (Figure 4-2). The temperature of the samples was maintained at 30 °C using a Viscotherm VT2 (Anton Paar, Österreich, Austria) water bath. Viscosity versus shear-rate was recorded with the Rheoplus v2.81 software supplied with the machine.

The double gap measuring system (Figure 4-2) is operated by adding the sample fluid to the cylindrical cup indicated by the blue shaded region. A second cylindrical cup, represented by the red shaded region, is lowered into the first.

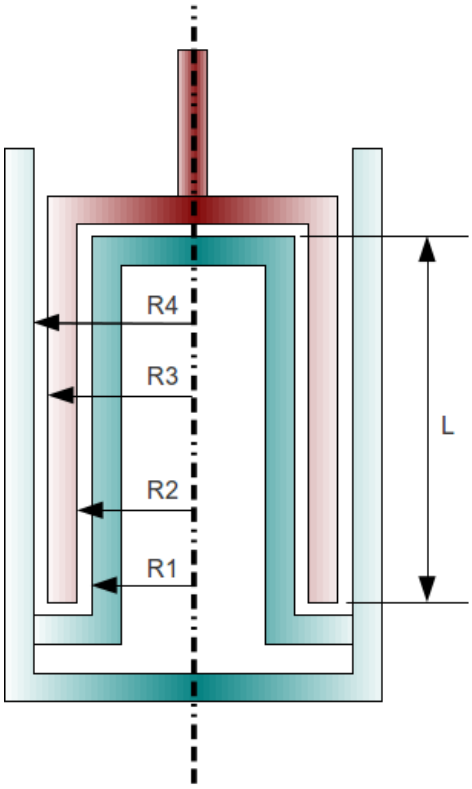

Figure 4-2: Double gap configuration for measuring viscosity

The sample fluid thus fills the gap between the two cylinders such that the entire length (L) is submersed. The torque acting on the red shaded cup while rotating is measured and the dynamic viscosity calculated based on the gap distances between R1 and R2, and R3 and R4.

To estimate the bulk viscosity of the fermentation medium, the fermentation mixture of Van Zyl *et al.* (2010) was analysed and the effect of each component on the apparent dynamic viscosity isolated. The base medium consisting of 5.95 g/L yeast nitrogen base (synthetic minimal medium) without amino acid and $(NH_4)_2SO_4$ supplementation (Difco, Becton, Dickinson and Company, Franklin Lakes, NJ) and 17.5 g/L $(NH_4)_2SO_4$ dissolved in RO water was autoclaved at 121 °C for 15 min. Its viscosity was measured at shear-rates that ranged from 0 to 350 s^{-1}.

High concentrations of oligosaccharides in solution may have a large effect on the viscosity of a solution (Chirife and Buera, 1997). To determine whether oligosaccharides are present in a sufficiently high concentration to affect the viscosity of the fermentation mixture, two experiments were conducted. Firstly, 20 g of Avicel particles were mixed with RO water to a final volume of 200 mL and autoclaved along with a control sample consisting only of RO water at 121 °C for 15 min. These samples were thoroughly agitated and placed in an oven set to 75 °C to allow free oligosaccharides to detach from the particles and enter the solution. The second test included the partial hydrolysis of cellulose to determine whether the amount of oligosaccharides released during this process is sufficient to influence the medium's viscosity. This was done by mixing 20 g of Avicel particles with 200 mL of 0.05 mol/L citrate buffer at pH 5.0 and autoclaving the mixture at 121 °C for 15 min. After the mixture had cooled sufficiently, 3 mL filter-sterilised Spezyme CP enzymes were added. The control sample consisted of 200 mL autoclaved citrate buffer with 3 mL added filter-sterilised enzymes. The experiment ran for 20 h with samples taken at 2 h, 4 h and 20 h. The samples were centrifuged at 5000 rpm for 3 min to remove the Avicel particles from suspension. Viscosity measurements were performed on both the control and sample supernatant.

Polysorbate 80 (also known as Tween 80), is a surfactant and emulsifier often used in the food and pharmaceutical industry to from emulsions and reduce the liquid surface tension. Tween 80's effect on the viscosity of the particle-fluid interaction was determined by mixing 10 g of Avicel with RO water to a volume of 200 mL. To each mixture 0.28 mL Tween 80 was added, except to the control sample and the viscosity measured.

The properties and effects of ethanol and glycerol on viscosity were calculated using experimental data and correlations obtained from Alkindi *et al.* (2008), González *et al.* (2007) and Adamenko *et al.* (2006). Moreira *et al.* (2009) proposed an equation:

$$v = v_{e/w} + a\left[e^{(b\,x_g)} - 1\right] \tag{4-5}$$

for predicting the kinematic viscosity (m^2/s) of ternary aqueous ethanol-glycerol solutions. This equation utilises the kinematic viscosity of the binary ethanol-water solution:

$$v_{e/w} = x_e v_e + (1 - x_e) v_w + x_e (1 - x_e) F_T \tag{4-6}$$

$$F_T = \left[e^{\left(\frac{3255}{T} - 9.41\right)} + (1 - 2x_e) e^{\left(\frac{3917}{T} - 11.44\right)} + (1 - 2x_e)^2 e^{\left(\frac{5113}{T} - 16.6\right)} \right], \tag{4-7}$$

which is adjusted to include effects of glycerol through:

$$a = -1.39 + 5.64\, e^{\frac{(273.1 - T)}{62.03}} + \left[3.56 - \frac{89.18}{(T - 273.1)^{1.5}} \right] x_e - 8.80 x_e^2 + 5.91 x_e^3 \tag{4-8}$$

$$b = 4.11 + 5.54\, e^{\frac{(273.1 - T)}{25.03}}, \tag{4-9}$$

where $v_{e/w}$, v_e, v_w, x_e, x_g and T are the kinematic viscosity (m^2/s) of the ethanol-water binary solution, pure ethanol and water, the molar fraction of ethanol and glycerol and the temperature (K), respectively.

An experiment was conducted with only Avicel (microcrystalline particles) in RO water at concentrations of 0, 20, 25, 30, 40, 60, 80 and 100 g/L to isolate the effects of particles in suspension of a known fluid. The viscosity of each mixture was measured at shear-rates ranging from 0 s^{-1} to 350 s^{-1}.

The kinematic viscosity from equation 4-5 was converted to a dynamic viscosity by multiplying it with the mass weighted average of the solution density (kg/m^3):

$$\rho_{eff} = \frac{m_w \rho_w + m_e \rho_e + m_g \rho_g}{m_{total}}. \tag{4-10}$$

Where m_w, m_e and m_g are the mass components and ρ_w, ρ_e and ρ_g the respective densities of water, ethanol and glycerol and m_{total} is the total mass of the ternary solution. This is a non-exact equation due to molecular interactions. However, this approximation was calculated to deviate from the true dynamic viscosity with less than 2 %.

The effects of yeast suspensions on the dynamic viscosity was calculated using Einstein's Law of viscosity:

$$\mu = \mu_0 (1 + 2.5\ \alpha_x), \tag{4-11}$$

with:

$$\alpha_x = \frac{\text{mass concentration}}{\text{yeast density}} \tag{4-12}$$

and μ the final dynamic viscosity and μ_0 the base dynamic viscosity of the fermentation medium. This formulation captures the influence of small, solid and non-interacting particles on the dynamic viscosity of a fluid and is only valid at particle volume fractions much lower than 1 ($\alpha_x << 1$). Cell concentrations from SSF experiments used in this study remained below 3.6 g/L and using the cell density for *S. cerevisiae* obtained from Mancini and Moresi (2000) as ρ_x=1432 kg/m^3, resulted in a volume fraction of approximately $\alpha_x = 2.5\text{x}10^{-3}$, which satisfies the condition for use of the Einstein's Law of viscosity.

All experiments were performed at least 4 times to confirm repeatability.

4.3.3 Modelling

Particle effects in the fermentation broth were modelled using the Ostwald-de Waele formulation:

$$\tau = \mu_P \dot{\gamma} , \tag{4-13}$$

with:

$$\mu_P = K \dot{\gamma}^{n-1} , \tag{4-14}$$

also known as the viscosity power-law (Sanin, 2002). The addition of particles increase the bulk viscosity of the fluid through particle interaction and the shear forces required to transport them through the flow field. The final viscosity (μ) can therefore be estimated using the base fluid viscosity, which includes the effects of the significant fermentation medium components and the contribution of the particles to the mixture:

$$\mu = (1-\alpha_P)\mu_0 + (\alpha_P)\mu_P . \tag{4-15}$$

Where, μ_o is the base viscosity of the solution, $\dot{\gamma}$ the shear-rate and K and n functions of the particle volume fraction (α_p). Parameter estimation for the K and n variables used in the Ostwald-de Waele formulation were obtained through power-law regression to best fit the experimental measurements relating the K and n variables to the volume fraction of cellulose particles present in the fermentation mixture:

$$K = \begin{cases} \dfrac{201(\alpha_P - 0.0125)}{[1+49(\alpha_P - 0.0125)]} & for\ \alpha_P > 0.0125 \\ 0 & for\ \alpha_P \leq 0.0125 \end{cases} \text{ and} \tag{4-16}$$

$$n = -2.764\,\alpha_P + 0.369 . \tag{4-17}$$

This was achieved using SigmaPlot 2001 for Windows version 7 (Systat Software Inc., San Jose, USA).

A sensitivity study was conducted on the μ_0, m_e and m_g, K and n variables (Table 4-2) using a cellulose particle volume fraction of 0.025 and shear-rate of 100 s^{-1} at a concentration of 35 g/L and 5 g/L for ethanol and glycerol, respectively. The target function was the final dynamic viscosity (μ) with variables evaluated at ±10 % and ±50 %.

4.4 Results

4.4.1 Particle properties

Particle density of the microcrystalline cellulose was determined using the Archimedes principle as ρ_P=1 605.7 kg/m^3 with a standard deviation of 56.3 kg/m^3. Particle settling experiments revealed an average terminal velocity of approximately $V_{P,\,term}$=6.53x10^{-3} m/s, with a standard deviation of 3.44x10^{-3} m/s.

The average effective particle diameter (D_{eff}) was determined as D_{eff} = 1.41x10^{-4} m with a standard deviation of 1.02x10^{-4} m. Using the known properties of water at 21 °C, with μ = 9.83x10^{-4} kg/m·s and ρ_W = 998 kg/m^3 (Çengel and Cimbala, 2006) along with D_{eff} = 1.41x10^{-4} m, the Reynolds number was calculated as Re_d = 0.9.

4.4.2 Viscosity

The viscosity of the base medium displayed Newtonian fluid behaviour with an average viscosity of 8.64x10^{-4} ± 1% kg/m·s. The reference viscosity of the RO water control was 8.31x10^{-4} kg/m·s, indicating a 3.8 % increase. This increase is primarily attributed to the presence of the 17.5 g/L $(NH_4)_2SO_4$ in solution.

Avicel particle effects on the viscosity proved most significant. Particle concentrations of 100 g/L Avicel increased the apparent dynamic viscosity to approximately 10^{-2} kg/m·s, decreasing with reduced concentrations as expected. The fluid viscosity with added particles displayed a shear-thinning effect in relation to the shear-rate (Figure 4-3). Further investigation indicated that particle concentrations below 20 g/L had negligible effects on the viscosity of the medium.

The viscosity results from the oligosaccharides tests for both the Avicel particles in water and the hydrolysis experiments indicated no significant variation. The results from the Tween 80 test indicated no significant effect on the viscosity, except in the shear-rate range of 0 to 50 s^{-1} where the average Tween 80 viscosity was 6 % - 26 % lower than the control results.

Results for the ethanol and glycerol effects were calculated from Equations 4-5 to 4-9 and found to increase the viscosity of the base medium to a maximum of 0.943x10^{-3} kg/m·s, with ethanol contributing most significantly as indicated by the sensitivity analysis (Table 4-2).

The contribution of the yeast cells to the viscosity of the medium proved negligible, as the total volume fraction occupied by the cells was calculated as 2.52x10^{-3}, which equated to a relative viscosity increase of 0.6 %.

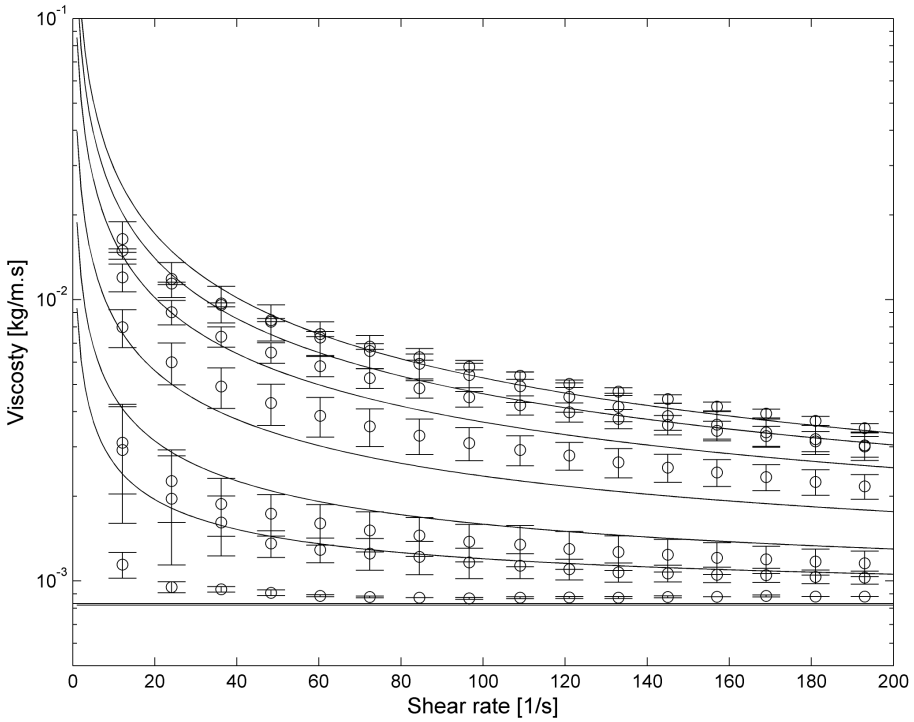

Figure 4-3: Apparent dynamic viscosity for Avicel particles in solution

4.4.3 Modelling

K and *n* variables were determined through a power regression (Table 4-1) methodology applied to the particle suspension viscosity measurements indicated in Figure 4-3. The hyperbolic regression (Equation 4-16) best fitted the experimental values for *K*, with a maximum error of 94.9 % occurring at the concentration of 30 g/L (volume fraction of 0.0188) Avicel particles. The parameter fit for the *n* variable was linear (Equation 4-17) with a maximum error of 13.05 %.

Table 4-1: Regression values for the K and n variables

Volume Fraction	Experimental		Numerical		Error%	
g/L	*K*	*n*	*K*	*n*	*K*	*n*
0.0125	0	0	0	N/A	0	N/A
0.015625	0.568	0.310	0.545	0.326	-4.155	5.16
0.01875	0.493	0.396	0.962	0.317	94.923	-19.9
0.025	1.904	0.312	1.558	0.300	-18.153	-3.85
0.0375	2.102	0.312	2.259	0.265	7.468	-15.1
0.05	3.172	0.205	2.657	0.231	-16.214	-3.245
0.0625	2.532	0.195	2.914	0.196	15.097	-0.106

Applying the K and n numerical estimation parameters into Equation 4-14 and Equation 4-15, predictions for the effects of the particles on the dynamic viscosity (Figure 4-3) displayed a reasonable correlation with an average error of 11.1 %. The largest error found in the final viscosity predictions was 26.4 % found at the particle concentration of 30 g/L.

Results from the sensitivity study (Table 4-2) indicated that the power coefficient (n) has the most influence, with a 252 % on the final viscosity when its value is reduced by 50 %. The ethanol and glycerol concentrations have the least effect on the dynamic viscosity, with 2.6 % and 0.28 % respectively.

Table 4-2: Sensitivity analysis for selected parameters

Variable	Variable effect in percentages			
	50%	90%	110%	150%
μ_0	-18.61	-3.72	3.72	18.61
K	-31.39	-6.28	6.28	31.39
n	252	23.88	-17.3	-50.26
x_e	-2.6	-0.521	0.522	2.61
x_g	-0.28	-0.056	0.056	0.28

4.5 Discussions

4.5.1 Particle properties

Variations in the density measurements may be attributed to small compositional variations between the crystalline and amorphous regions of the particles. However, the resulting density of 1 605.7 kg/m^3 was found to correlate well with literature (Sun, 2005). The results from the investigation of particle settling velocity indicated a wide range of settling rates. These variations are attributed to variations in density, size and particle topology. The average value of $V_{P,\,term} = 6.53\text{x}10^{-3}$ m/s was found to best represent the settling behaviour.

The calculation of the equivalent spherical diameter for the particles resulted in a particle size ($D_{eff} = 1.41\text{x}10^{-4}$ m) of nearly triple the average size stated by the manufacturer ($D = 5\text{x}10^{-5}$ m). This is due to the irregular particle shapes (Figure 4-1), structure water (Matthews, 2006) and surface effects (Zheng, 2003) which cause higher drag forces than typical spherical objects of similar size, thus increasing the effective drag force each particle experiences. The Reynolds number for the average particle size and terminal settling velocity was calculated as $Re_d = 0.9$, which indicated that the Stoke's Law approximation is valid since the particle remain in the creeping flow regime.

4.5.2 Viscosity

Microcrystalline cellulose particles proved to have the largest influence on the bulk fluid viscosity. It was also noted that particle concentrations below 20 g/L had negligible effects on the viscosity of the fermentation medium due to a lack of

significant particle interaction. The prediction model for the particle influence on the dynamic viscosity correlated well at high shear-rates, but deviated from the experimental data at lower shear-rates. This error could be reduced with higher order regression models, but this is not necessary, as most industrial mixing occurs at higher shear-rates and turbulent conditions, therefore simpler models are preferred.

Viscosity effects of the base medium, Tween 80, yeast cell concentrations and oligosaccharides in the solution were shown to be insignificant compared to the effect of the particles. The deviation between Tween 80 and control sample results at low shear-rates is a strong indication that Tween 80 reduces the frictional drag which occurs during particle interaction. However, at high shear-rates this deviation disappears, possibly indicating that interaction time between particles are significantly reduced, thus diminishing any effect of this surfactant.

Ethanol and glycerol have been recorded to have a large effect on the viscosity of binary and ternary solutions. However, during most fermentation processes the concentrations of these two products are relatively low, with ethanol not exceeding 10 % w/w, thereby having little effect on viscosity.

4.5.3 Modelling

Over-estimation of viscosity at 30 g/L by an average of 13 % is a result of the error caused by the *K*-parameter regression equation over-estimating the parameter with 94.9 %. The sensitivity analysis suggests that the cellulose particles are the significant factor when calculating the dynamic viscosity of a saccharification and fermentation reactor. The effects of the cultivation medium and the by-products ethanol and glycerol are negligible compared to the particles. Ethanol and glycerol, however, play a larger role once the particle concentration falls below 25 g/L. The numerical model for estimating the dynamic viscosity within a cellulose conversion reactor showed reasonable correlation to the experimental data, having an average error of 11.1 %. The model was also capable of predicting the system behaviour and capture the primary trends observed.

The implication for using this type of modelling is the ability to predict viscosity within a cellulosic-ethanol reactor. With lignocellulosic ethanol technology rapidly approaching commercialisation, the possible effects of other particles such as lignin on the viscosity should also be investigated. The inclusion of lignin in the fermentation reactors is not ideal, though practically unavoidable given current technology and economic aspects thereof. This type of modelling scheme can be used and its parameters adjusted to account for most cellulosic particulate substrates, including paper-pulp, pretreated soft and hard woods, and any other cellulosic particulates. Under industrial conditions it would be reasonable to expect high substrate loading, thus increasing the particle effects even more. Further studies would benefit the community to design and model these industrial processes more significantly.

5 PREPARING FOR COMPUTATIONAL FLUID DYNAMICS

5.1 Abstract

In addition to the kinetic and viscosity models presented in Chapter 3 and Chapter 4 respectively, preparing for CFD requires an understanding of boundary conditions and physical models used to represent the virtual problem. Discussed in this chapter are the mesh geometry and various models used in this study including the cell-types, boundary conditions and physics. Particle physics was validated in terms of a maximum packing factor, a rheological replication of the experimental results discussed in Chapter 4 and the total particle suspension height. Furthermore, surface effects were investigated numerically and compared to experimental observations, along with grid independence checks for required mesh resolution and appropriate turbulence model selection. Solid packing factor results suggested the requirement of a solid pressure force model. The standard model proposed in literature was established to be extremely unstable and prone to large error at the low packing factor required, namely 0.21. A new version of this model was proposed, which improved the numerical stability and significantly reduced the error at low packing factors. Results for the rheological validation simulations indicated that due to the lack of particle interaction models, CFD was incapable of correctly predicting the particle distribution under laminar conditions. Particle suspension comparisons suggested that although the turbulence in the fermenters improved the particle transportation, the assumption of an effective particle diameter produces discrepancies with experimental observations. This was probably caused by the large variation in particle size, leading to smaller particles reaching higher levels of suspensions while larger particles settle more rapidly. Limitations in the commercial CFD code compelled the use of the realisable k-ε turbulence model. Grid independent studies suggested a minimum cell-resolution of 200 000 cells to correctly capture the dominant flow characteristics within 1 L fermenters.

5.2 Introduction

CFD is an extremely useful engineering tool which involves the numerical simulation of continuous fluid domains. This tool has over recent decades expanded to include thermodynamic and stress solvers for solids as well as fluid structure interface capabilities. Applications for CFD is widespread with use in geological, nuclear, aerodynamics, petrochemical, automotive and thermodynamic industries.

In terms of mixing vessels CFD has successfully been utilised in analysing particle suspensions and bubble transport through these systems (Martın et al., 2010, Hristov *et al.*, 2004). Relevant CFD capabilities to analyse mixing and reaction conditions for bioethanol production through simultaneous saccharification and fermentation are discussed in this chapter. It investigates the

advantage and disadvantage of each feature and identifies the best solution for the numerical analyses conducted in Chapter 6. Verification case studies are presented to confirm the accuracy of various model predictions and discuss possible causes of any discrepancies.

CFD is a finite volume based numerical simulation tool requiring the fluid or solid domain to be discretised into smaller volumes known as cells. Presented in Figure 5-1 is a simple example for creating a cell mesh to analyse flow through a pipe: (1) The geometry of the pipe is required, (2) the region occupied by the fluid is extracted, in this case the inside of the pipe, (3) this fluid occupied region is discrestised into smaller cells, presented in (4). For each of these cells the governing differential equations are solved. These include the momentum equation:

$$\rho \frac{\mathrm{D}\boldsymbol{V}}{D t} = \rho \boldsymbol{g} - \nabla p + \nabla \cdot \tau_{ij}^{'} + \boldsymbol{F}_{\text{intern,s}} + \boldsymbol{S}_{\text{interphase}} , \tag{5-1}$$

Continuity equation (mass conservation):

$$\frac{\mathrm{D}\rho}{D t} + \rho \operatorname{div} \boldsymbol{V} = 0 , \tag{5-2}$$

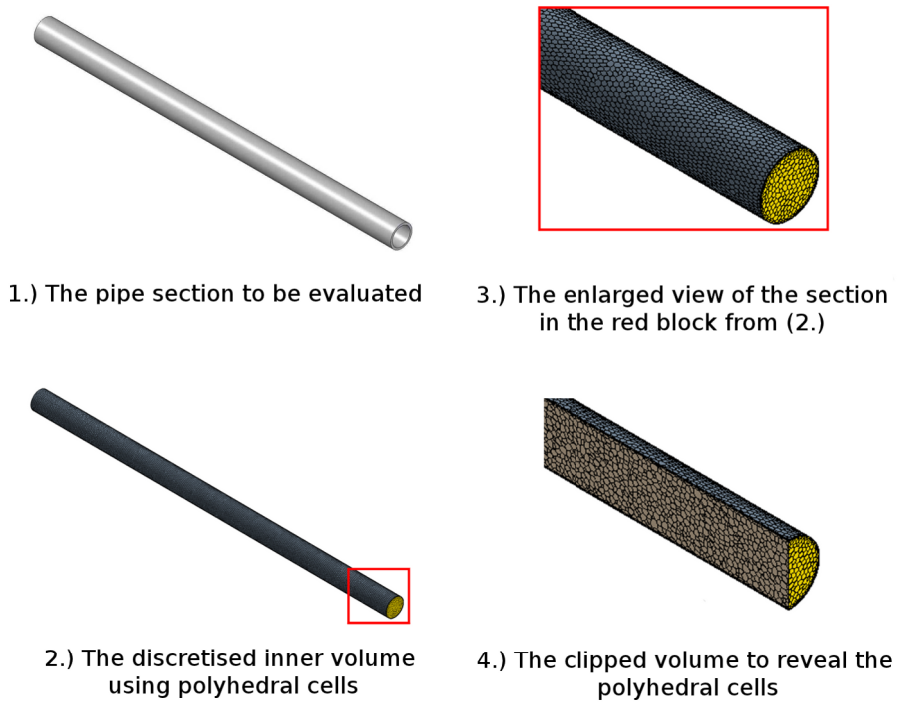

Figure 5-1: Discretizing the inner pipe volume for CFD evaluation

Energy conservation equation (White, 1991):

$$\rho \frac{Dh}{Dt} = \frac{Dp}{Dt} + \mathrm{div}(k_t \nabla T) + \tau'_{ij} \frac{\partial u_i}{\partial x_j} , \tag{5-3}$$

For a Newtonian fluid (White, 1991):

$$\tau'_{ij} = \mu \left(\frac{\partial u_i}{\partial x_j} + \frac{\partial u_j}{\partial x_i} \right) + \delta_{ij} \lambda \, \mathrm{div} \, V \quad \text{and} \tag{5-4}$$

Equation of state (Versteeg and Malalasekera, 1995):

$$p = p(\rho, T) . \tag{5-5}$$

presented in tensor form.

Additional to the fundamental fluid equations presented above, models describing phenomenons such as non-Newtonian fluids, turbulence and chemical reactions can be included. This is discussed in Chapter 5. This modular approach results in near limitless possibilities for the use of this numerical tool, provided the computational resources are available.

Turbulence modelling is an extensively researched field of study. The need for turbulence modelling arises as a result of the large variation in the scale of eddies present in the flow. Eddies are formed when large shear energies cause the flow to become unstable and form vortices. Large eddies tend to break-up due to viscous effects transferring its energy to its smaller eddies, which in turn break-up further into smaller eddies. This process continues down to a near molecular level and capturing these minute eddies directly is extremely computationally expensive and in most cases not feasible. Various models therefore exist, each having different applications and intended to capture different turbulent eddy scales and effects. It is the CFD user's responsibility to select the turbulence model appropriate for the flow problem investigated.

- Direct Numerical Simulation (DNS) involves the solving of the Navier-Stokes equation without the use of a turbulence model. These solutions are capable of producing very accurate predictions at the cost of extreme computational effort. The only requirement of such a simulation is that it must be transient, as the solutions to the Navier-Stokes equation are exact at any instantaneous moment in time (Paul *et al.*, 2004). This method is not feasible for most flow problems due to limited computational resources.

- Reynolds Averaged Navier-Stokes (RANS) eddy viscosity models are intended for obtaining an average velocity field, free of instantaneous

fluctuations. This is done by time averaging the Navier-Stokes equation, which results in the nine Reynolds turbulent stresses tensor:

$$\text{Reynolds stresses} = -\rho \overline{u_i' u_j'}\,, \tag{5-7}$$

representing the instantaneous fluctuations. Capturing the effects of these stresses require additional closure models (Paul *et al.*, 2004). Many variations and formulations for these closure models have been proposed, of which the simplest is the Boussinesq approximation:

$$-\rho \overline{u_i' u_j'} = 2\mu_t \mathbf{S} - \tfrac{2}{3}(\mu_t \nabla \cdot \boldsymbol{v} + \rho k)\boldsymbol{I} \tag{5-8}$$

where **S** is the strain tensor:

$$\boldsymbol{S} = \tfrac{1}{2}(\nabla \boldsymbol{V} + \nabla \boldsymbol{V}^{\mathrm{T}}) \quad . \tag{5-9}$$

Most commonly used closure formulations for the eddy viscosity (μ_t) include the single-parameter Spalart-Allmaras and two-parameter *k*-ω turbulence models, which are well suited for aerospace applications such as flows over wing profiles and aircraft fuselage. The two-parameter *k*-ε turbulence models, which provide an acceptable compromise between model robustness, computational cost and accuracy, are generally well suited for most industrial-type applications that contain complex recirculation regions (CD-Adapco, 2011). These are discussed in more detail below.

- A second type of RANS model is the Reynolds stress models, which take into account all six Reynolds stresses. The equations for these models are highly coupled and to obtain convergence is challenging. These models are mainly suitable for highly anisotropic flows, such as those found in cyclones (Paul *et al.*, 2004).
- Large Eddy Simulation (LES) is similar to the DNS approach as the governing transient equations are solved directly on a larger scale, thus allowing coarser grids with the smaller sub-grid turbulent effects modelled. This method is much less computationally demanding than the DNS method but can still capture the macro-scale effects (Paul *et al.*, 2004).
- Detached Eddy Simulation (DES) is the newer model receiving attention. This model combines the LES and RANS models to form a model which uses LES in the bulk flow, but a RANS model in the boundary layer.

5.3 Methods and Materials

The commercially available CFD software package, STAR-CCM+ version 6.02.007 (CD-Adapco, London, UK, 2011), was selected for this study and incorporates an automatic mesh generator and multiple advanced engineering reporting capabilities.

5.3.1 Mesh generation

Mesh generation used to be a tedious procedure with each discretised volume cell requiring manual description in the numerical code. This included the physical shape, boundary conditions and position of each cell in the fluid domain. It often required months to construct, while actual simulations required only days to perform.

With the introduction of more powerful computers and the development of grid generation codes, fluid domains could be created with user friendly graphical interfaces, which significantly reduced the time required to develop a quality volume mesh. Development of computer aided design (CAD) packages and automated grid generation software further reduced the user time required to develop a full domain mesh allowing construction of larger and more complex grids. This technology continued to improve until the present, where automatic grid generation software is capable of importing a large variety of three-dimensional CAD formats and create a high quality grid for use in CFD solvers. The advantage of these codes is the rapid modifications which are capable with a minimum cost of time. The latest commercial codes have integrated the CAD and grid generation software into the CFD interface allowing grids to be modified without losing the domain fluid flow solutions, while decreasing the time for performing grid independence tests significantly.

Three primary cell-types are available in modern CFD packages (Figure 5-2). These are tetrahedral, hexahedral and polyhedral cell-types. Tetrahedral cells were originally the preferred cell-type for automatic grid generators and are capable of filling any complex geometry. However, due to the large number of acute angles and inherently non-flow aligned faces, this cell type is highly prone to numerical instability and significant false diffusion. It is seldom recommended for most present applications.

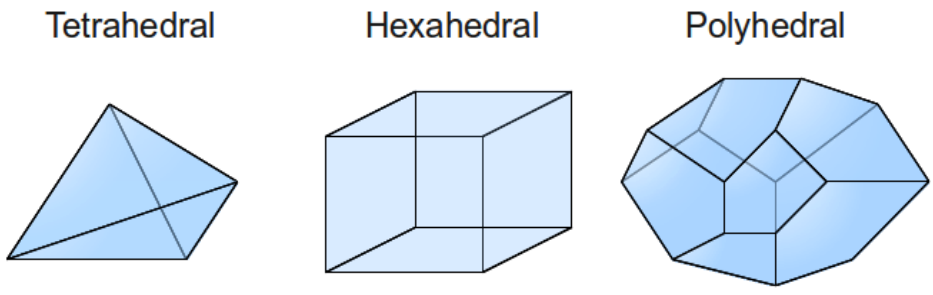

Figure 5-2: Cell-types available for discretisation in CFD codes

Hexahedral cells have a significant increase in stability over tetrahedral cells if aspect ratios are limited, and they offer the highest efficiency of all cell-types. For flow conditions with single directionality and low gradients, these cells offer the least amount of false diffusion. If structured correctly, these cells allow for high convergence rates and simulation throughput due to the reduced complexity of the cell geometry. However, for flows with large gradients, and non-directionality, hexahedral cells suffer from increased false diffusion and numerical convergence rates may decrease.

Polyhedral cells are a more recent development in the finite volume method formulation and can comprise of a large number of faces. Polyhedral cells provide a compromise between the tetra- and hexahedral cell-types. These cells have a significant advantage over the previous two cell-types. Polyhedral cells are capable of forming any complex shapes like the tetrahedral cells, but due to the large internal angles, false diffusion in flow-fields with high gradients are significantly reduced, allowing similar solutions to tetrahedral cells types with a fraction of the grid resolution required. The disadvantage of polyhedral cells is the increased mathematical complexity and thus an increase in computer time required per cell. Thus for cases with simple, low gradient flows hexahedral cells are recommended. However, for highly variable flow directions and complex shapes, the polyhedral cells can reach grid convergence more rapidly, thus reducing the difference in simulation time between hexahedral and polyhedral cells.

5.3.2 Boundary conditions

Multiple boundary conditions are available for selection in most CFD codes, each with a specific intention and numerical formulation. This section describes and discusses the wall, symmetry plane and interface boundaries as presented in the commercial CFD code STAR-CCM+.

Boundary conditions are required in any numerical finite element or finite volume simulation. In finite volume codes these conditions are applied primarily to the faces of cells which are not shared by another (wall and symmetry boundaries), although certain boundary conditions (interface boundaries) are applied to internal cell faces (Figure 5-3).

Wall boundaries are the most common boundary condition used in most fluid simulations and represent an impenetrable obstruction to flow. Depending on the required conditions, these boundaries may be assigned a slip or no-slip wall shear stress condition. The default no-slip condition allows the development of boundary layers. These boundaries further permit the specification of a tangential velocity which represents a boundary movement relative to the flow.

A symmetry plane is generally employed to indicate symmetry in the geometry investigated. These boundaries form an impenetrable interface forcing flow to remain in the domain, effectively generating a solution which could be mirrored across the symmetry plane to obtain the full solution. This provides an important

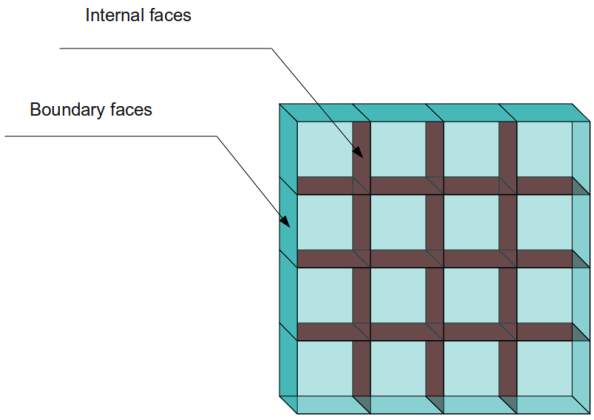

Figure 5-3: Boundary and internal faces in a finite volume grid

benefit of reducing the volume to be meshed, allowing higher cell-resolutions to be used to obtained equivalent solutions.

Interface boundaries primarily divide the flow domain into regions and provided a connection between these flow regions. Different physics models can be applied to each region while maintaining a fully connected flow domain. The most commonly used interface boundaries are the in-place and periodic boundary conditions. In-place boundaries (Figure 5-4) provide a conformal connection to different regions in the flow-field. An example of this is a mixing vessel with the inner region rotating while the outer region remains stationary. Communication between these regions requires an in-place boundary be placed as to effectively couple the two regions. A second example where an in-place boundary is required is to transition between two different flow types such as porous and non-porous regions.

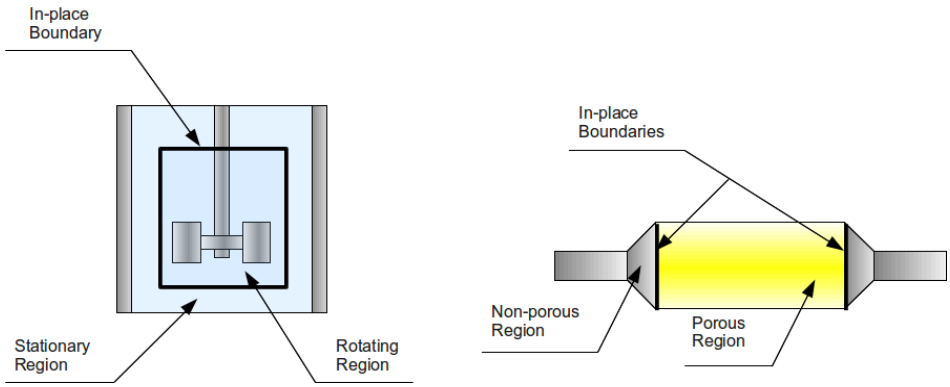

Figure 5-4: In-place boundary applications for distinguishing domain regions

Periodic boundary conditions allow the mapping of one boundary face to another in a flow domain, forming an endless loop, which presents a larger domain. A prime example is the analyses of a helicopter blade, which is cyclic. Defining the fluid domain correctly around a selected blade provides an equivalent solution to modelling the entire rotor as indicated in Figure 5-5. The basic principle is that the flow exiting one boundary is mapped to the corresponding boundary. However, caution should be taken to ensure that these boundaries are placed in the correct position to ensure the physical representation and reality remains valid.

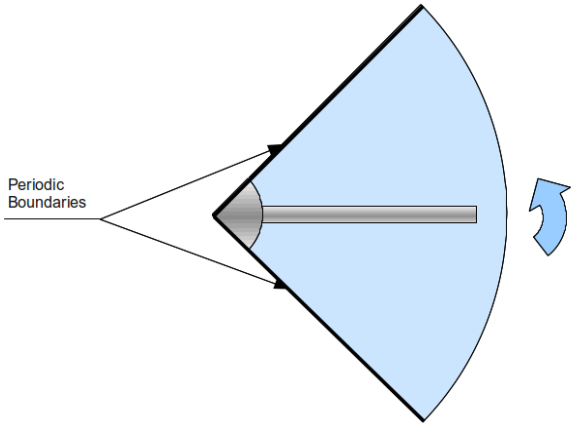

Figure 5-5: Periodic boundary condition applied to helicopter rotor

5.3.3 Physical models

Rigid body motion

Rigid body motion and moving reference frames are used to calculate the effects of an impeller on the fermenter flow field. Moving reference frames are mostly used for steady-state simulations and utilise a single impeller position for each solution. Rigid body motion on the other hand allows the vertices of the mesh to move from one time step to the next, effectively solving the flow field at different impeller positions, effectively capturing transient effects. Both these formulations use

$$G_f = \left(\boldsymbol{A} \cdot \boldsymbol{v}_g \right)_f \tag{5-10}$$

to describe the mass grid flux and

$$\mathbf{F}_r = \rho \, \boldsymbol{\omega} \times \boldsymbol{v} \tag{5-11}$$

for the rotational body force respectively, with the grid velocity $\boldsymbol{v}_g$, face area $\boldsymbol{A}$, and angular velocity $\boldsymbol{\omega}$.

Multiphase conservation equations

Multiphase segregated flow solves a set of conservation equations for each Eulerian phase present in the simulation. During these simulations the pressure is assumed to be the same in all phases with the volume fraction specifying the ratio of species present in each cell. This solver uses a SIMPLE-type approach consisting of separate pressure and velocity solvers.

Continuity from (Equation 5-2) is specified for multiphase flow by:

$$\frac{\partial}{\partial t}(\alpha_i \rho_i)+\nabla\cdot(\alpha_i \rho_i \boldsymbol{v}_i)=0 \tag{5-12}$$

and $$\sum_i \alpha_i = 1 \quad , \tag{5-13}$$

with α_i the volume fraction, ρ_i the species density and $\boldsymbol{v}_i$ the velocity of phase *i*.

The multiphase conservation of momentum from (Equation 5-1) is calculated by:

$$\frac{\partial}{\partial t}(\alpha_i \rho_i \boldsymbol{v}_i)+\nabla\cdot(\alpha_i \rho_i \boldsymbol{v}_i \boldsymbol{v}_i)=-\alpha_i \nabla p+\alpha_i \rho_i \boldsymbol{g}+\nabla\cdot\left[\alpha_i(\tau_i+\tau_i^t)\right]+\boldsymbol{M}_i \tag{5-14}$$

and $$\sum \boldsymbol{M}_i = 0 \quad , \tag{5-15}$$

with p the pressure, **g** the gravity vector τ_i and τ^t_i the molecular and turbulent shear stresses respectively, and $\mathbf{M}_i$ the inter-phase momentum transfer per unit volume. The inter-phase models include effects such as drag, lift, virtual mass and turbulence dispersion interaction between the Eulerian phases.

Drag force

The inter-phase drag force follows the derivation of Gosman *et al.* (1992), with the continuous phase modelled as

$$F_{ij}^{D} = A_{ij}^{D}(\boldsymbol{v}_c - \boldsymbol{v}_d) \quad , \tag{5-16}$$

with the linearised coefficient generally expressed as

$$A_{ij}^{D} = \frac{3\,\alpha_d(\alpha_c)^{n_v}\rho_c C_D}{4\,l_{cd}}|\boldsymbol{v}_r| \quad . \tag{5-17}$$

There are four widely used drag models for a rigid spherical particle (Figure 5-6). The Schiller and Naumann (1933) model was developed for isolated particles in a flow field, with a drag coefficient C_D as expressed in

$$C_D = \begin{cases} \frac{24}{Re_d}(1+0.15\,Re_d^{0.687}); & 0 < Re_d \leqslant 1000 \\ 0.44 \quad ; & Re_d > 1000 \end{cases} \quad . \tag{5-18}$$

Due to the high number of particles present in the reactor and the significant interaction between these particles, a high particle loading model is necessary for calculating the drag forces on the particles by the medium and the momentum transfer associated with the fluid. The Gidaspow drag model (Gidaspow, 1994) was developed for use with fluidised beds and utilises the Ergun equation:

$$A_{ij}^D = \frac{150\,\alpha_d^2\,\mu_c}{\alpha_c\,l_{cd}^2} + \frac{1.75\,\alpha_d\,\rho_c\,|\boldsymbol{v}_r|}{l_{cd}} \tag{5-19}$$

for high particle concentrations ($\alpha_d > 0.2$) and a modified Stokes law:

$$A_{ij}^D = \frac{3}{4} C_D \frac{\alpha_d \rho_c}{l_{cd}} |\boldsymbol{v}_r|\,\alpha_c^n \tag{5-20}$$

for regions with lower particle concentrations ($\alpha_d \leq 0.2$).

The Syamlal and O'Brien drag model was developed for use with particle settling, utilising a modified drag equation:

$$A_{ij}^D = \frac{3\,\alpha_c\,\alpha_d\,\rho_c\,C_D}{4\,V_{rs}^2\,l_{cd}} |\boldsymbol{v}_r| \quad , \tag{5-21}$$

to account for the effects of terminal velocity, where:

$$V_{rs} = 0.5\,[A - 0.06\,Re_d + \sqrt{(0.0036\,Re_d)^2 + 0.12\,Re_d(2\,B - A) + A^2}] \quad , \tag{5-23}$$

$$A = \alpha_c^{4.14} \quad \text{and} \tag{5-24}$$

$$B = \begin{cases} 0.8\,\alpha_c^{1.28}; & \alpha_c < 0.85 \\ \alpha_c^{2.65} \quad ; & \alpha_c \geqslant 0.85 \end{cases} \quad . \tag{5-25}$$

The drag coefficient:

$$C_D = \frac{24}{Re_d} + \frac{6}{(1+\sqrt{(Re_d)})} + 0.4 \quad , \tag{5-22}$$

proposed by White (1991) was used to calculate drag for all Reynolds Numbers less than 2×10^{-5}.

Where $\boldsymbol{v}_r = \boldsymbol{v}_d - \boldsymbol{v}_c$ is the relative velocity between the continuous and dispersed

phases, C_D is the standard drag coefficient for a solitary particle and l_{cd} is the interaction length scale representing the particle diameter.

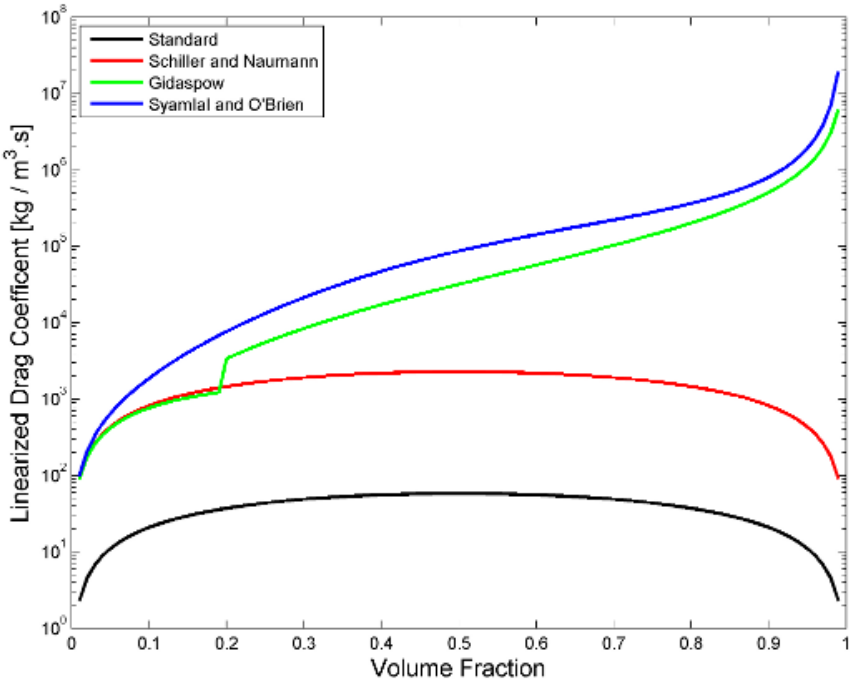

Figure 5-6: Comparison of more prominent drag models

Lift force

Lift was calculated using the Auton *et al.* (1988) derivation:

$$\boldsymbol{F}_L = C_L \alpha_d \rho_c [\boldsymbol{v}_r \times (\nabla \times \boldsymbol{v}_r)] \quad , \tag{5-26}$$

where C_L is the lift coefficient, assumed as 0.25 (Lance *et al.* (1991), due to non-uniform or swirling flow.

Virtual mass

Virtual mass force accounts for additional resistance experienced by a bubble undergoing acceleration in a flow field (Auton *et al.,* 1992) in:

$$\boldsymbol{F}_{cd}^{VM} = C_{VM} \alpha_d \rho_c \left[\left(\frac{D\boldsymbol{v}}{Dt} \right)_d - \left(\frac{D\boldsymbol{v}}{Dt} \right)_c \right] \quad , \tag{5-27}$$

where C_{VM} is the virtual mass coefficient with a default value of 0.5. This model

is only applicable where there is a large density difference between two Eulerian phases.

Turbulent dispersion

Turbulent dispersion forces account for interaction between particles and turbulent eddies in the continuous fluid and are modelled as:

$$\boldsymbol{F}_{\mathrm{cd}}^{\mathrm{TD}}=\left(-A_{\mathrm{cd}}^{\mathrm{D}}\right)\frac{\nu_{\mathrm{c}}^{\mathrm{t}}}{\sigma_{\alpha}}\left(\frac{\nabla\alpha_j}{\alpha_j}-\frac{\nabla\alpha_i}{\alpha_i}\right) \quad . \tag{5-28}$$

Volume fraction is a scalar parameter used in multiphase fluid flow simulations to determine the ratio of various species within a specific cell:

$$\alpha_i=\frac{V_i}{V} \tag{5-29}$$

with V_{i} the volume of species i and V the total volume of the cell.

Solid particle force

Particles have a limited packing density, which prevents solid particles from completely occupying a volume and is accounted for by a solid pressure force. STAR-CCM+ uses:

$$\boldsymbol{F}_{i,s}=-e^{\left[-600\left(\alpha_{\max,\mathrm{s}}-\alpha_{\mathrm{s}}\right)\right]}\nabla\alpha_{\mathrm{s}} \tag{5-30}$$

to represent the force per volume (N/m^3) of particles acting upon each other and preventing the solids volume fraction from exceeding the allowable particle packing density.

This model was found to be highly unstable at low solid packing densities and tends to overshoot the maximum solids volume fraction specified. This instability is caused by errors in the particle packing fraction, which exceed the maximum packing density, resulting in large pressure jumps within these volume cells. The flow field then attempts to counter this large pressure gradient by adjusting the velocity, leading to large oscillating and non converging solutions. To reduce overrun produced by this formulation, the solid pressure force should be limited to atmospheric pressure as indicated by:

$$\boldsymbol{F}_{i,\mathrm{s}}=\min\left\{-e^{\left[-600\left(\alpha_{\max,\mathrm{s}}-\alpha_{\mathrm{s}}\right)\right]}\nabla\alpha_{\mathrm{s}},101\ 325\nabla\alpha_{\mathrm{s}}\right\} \quad . \tag{5-31}$$

This does not, however, improve the stability of the model at low packing fractions, as pressure discontinuities occur as the code jumps between the two equations.

An alternative formulation was proposed by the author, limiting the maximum

pressure force to atmospheric pressure while producing a continuous gradient through all possible volume fractions, as given by:

$$\boldsymbol{F}_{i,\mathrm{s}} = -\frac{101325}{2}\{\tanh[200(\alpha_{\mathrm{max,\,s}} - \alpha_{\mathrm{s}})] - 1\}\nabla\alpha_{\mathrm{s}} \quad . \tag{5-32}$$

This model further proved significantly more stable at all volume packing densities when compared to Equation 5-31. Figure 5-7 presents a comparison between the original solid pressure force equations (Equations 5-30 and 5-31) available in STAR-CCM+, and the new solid pressure force formulation proposed in this work.

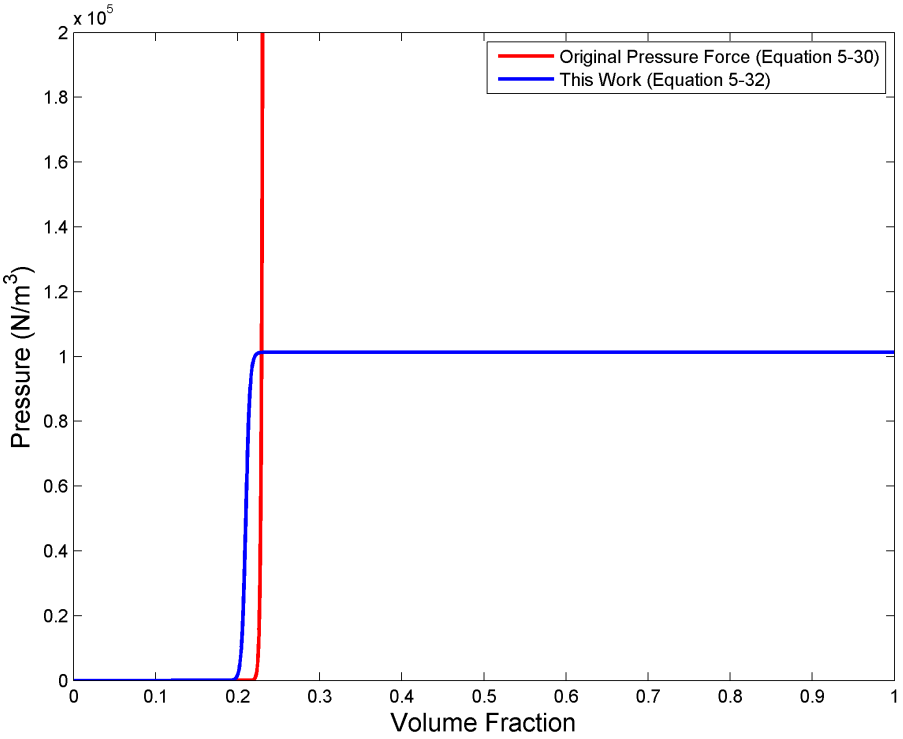

Figure 5-7: Comparison between solids pressure force models

Shear-rate

Shear-rate has a significant influence on a particulate fluid in terms of its viscosity and should thus be taken into account (Equation 4-13). For a three-dimensional Cartesian domain, the representative shear-rate is calculated as a function of the various velocity gradients:

$$\dot{\gamma} = 2\sqrt{\frac{1}{2}\left[\left(\frac{\mathrm{d}u}{\mathrm{d}x}\right)^2 + \frac{1}{2}\left(\frac{\mathrm{d}u}{\mathrm{d}y} + \frac{\mathrm{d}v}{\mathrm{d}x}\right)^2 + \frac{1}{2}\left(\frac{\mathrm{d}w}{\mathrm{d}x} + \frac{\mathrm{d}u}{\mathrm{d}z}\right)^2 + \frac{1}{2}\left(\frac{\mathrm{d}w}{\mathrm{d}y} + \frac{\mathrm{d}v}{\mathrm{d}z}\right)^2 + \left(\frac{\mathrm{d}v}{\mathrm{d}y}\right)^2 + \left(\frac{\mathrm{d}w}{\mathrm{d}z}\right)^2\right]} \quad , \tag{5-33}$$

derived from Fung (1994).

Turbulence

Laminar flow is the condition where no turbulence occurs. Under these conditions the Navier-Stokes (NS) equations can be solved exactly, as no turbulence models need to be employed. True laminar flow conditions can thus be solved using coarse mesh resolutions. The complete NS equations can also solve turbulent conditions. However, this is not common practice, as the grid resolution required to resolve the turbulent eddies are excessively fine such that computational time and memory requirements are not justified. Various turbulent models have been proposed to overcome the high grid resolution requirements for solving the complete NS equations. At the time of writing only the two-parameter *k*-ε class of RANS models were available for multiphase flows in STAR-CCM+.

The multiphase standard *k*-ε model used in STAR-CCM+ (CD-Adapco, 2011) involves a two-equation formulation to solve the transport equations for the turbulence kinetic energy (*k*):

$$\begin{aligned}&\frac{\mathrm{d}}{\mathrm{d}t}\int_V \alpha_i \rho_i k_i \,\mathrm{d}V + \int_A \alpha_i \rho_i k_i (\boldsymbol{v}_i - \boldsymbol{v}_g)\cdot \mathrm{d}\boldsymbol{a} = \\ &\int_A \alpha_i \left(\mu_i + \frac{\mu_i^t}{\sigma_k}\right)\nabla k_i \cdot \mathrm{d}\boldsymbol{a} + \int_V \alpha_i [G_i^k - \rho_i(\varepsilon_i - \varepsilon_0) + S_i^k]\,\mathrm{d}V\end{aligned} \tag{5-34}$$

and turbulent kinetic energy dissipation rate (ε)

$$\begin{aligned}&\frac{\mathrm{d}}{\mathrm{d}t}\int_V \alpha_i \rho_i \varepsilon_i \,\mathrm{d}V + \int_A \alpha_i \rho_i \varepsilon_i (\boldsymbol{v}_i - \boldsymbol{v}_g)\cdot \mathrm{d}\boldsymbol{a} = \\ &\int_A \alpha_i \left(\mu_i + \frac{\mu_i^t}{\sigma_\varepsilon}\right)\nabla \varepsilon_i \cdot \mathrm{d}\boldsymbol{a} + \int_V \frac{1}{T}[\alpha_i (C_{\varepsilon 1} G_i^k - C_{\varepsilon 2}\rho_i(\varepsilon_i - \varepsilon_0)) + S_i^\varepsilon]\,\mathrm{d}V\end{aligned} \tag{5-35}$$

within a flow domain (Jones and Launder, 1972).

where the turbulent production term (G_i^k), modulus of the mean strain rate (S_i) are given by

$$G_i^k = \mu_i^t S_i^2 - \frac{2}{3} i \rho_i k_i \nabla\cdot\boldsymbol{v}_i - \frac{2}{3}\mu_i^t (\nabla\cdot\boldsymbol{v}_i)^2 \quad , \tag{5-36}$$

$$S_i = \sqrt{2\boldsymbol{S}_i : \boldsymbol{S}_i} \quad \text{and} \tag{5-37}$$

$$\boldsymbol{S}_i = \dot{\gamma} = \frac{1}{2}(\nabla \boldsymbol{v}_i + \nabla \boldsymbol{v}_i^T) \quad . \tag{5-38}$$

The turbulent eddy-viscosity (μ_i^t) is calculated using:

$$\mu_i^t = \rho_i C_\mu k_i T_i \quad , \tag{5-39}$$

with the turbulent time scale presented calculated as:

$$T_i = \max\left(\frac{k_i}{\varepsilon_i}, C_t\sqrt{\frac{\nu_i}{\varepsilon_i}}\right) \quad . \tag{5-40}$$

The remaining coefficients were proposed by Launder and Sharma (1974) as $C_{\varepsilon 1} = 1.44$, $C_{\varepsilon 2} = 1.92$, $C_\mu = 0.09$, $\sigma_k = 1.0$, $\sigma_\varepsilon = 1.3$ and $C_t = 1.0$.

The realizable *k-ε* turbulence model is an adjusted form of the standard *k-ε* model with the new transport equation for the turbulent kinetic energy dissipation rate (ε) as proposed by Shih *et al.* (1994):

$$\begin{aligned}&\frac{\mathrm{d}}{\mathrm{d}t}\int_V \alpha_i\rho_i\varepsilon_i \mathrm{d}V + \int_A \alpha_i\rho_i\varepsilon_i(\boldsymbol{v}_i - \boldsymbol{v}_g)\cdot\mathrm{d}\boldsymbol{a} = \\ &\int_A \alpha_i\left(\mu_i + \frac{\mu_i^t}{\sigma_\varepsilon}\right)\nabla\varepsilon_i\cdot\mathrm{d}\boldsymbol{a} + \\ &\int_V \frac{1}{T}\left[\alpha_i\left(C_{\varepsilon 1}S_i\varepsilon_i - \frac{\varepsilon_i}{k_i + \sqrt{\nu_i\varepsilon_i}}C_{\varepsilon 2}\rho_i(\varepsilon_i - \varepsilon_0)\right) + S_i^\varepsilon\right]\mathrm{d}V\end{aligned} \quad , \tag{5-41}$$

with the turbulent eddy-viscosity given by:

$$\mu_i^t = \rho_i C_i^\mu \frac{k_i^2}{\varepsilon_i} \quad . \tag{5-42}$$

This new model includes a modified C_i^μ coefficient, which is a function of the mean flow and turbulence *k* and *ε* values rather than assumed constant, as in the standard model:

$$C_i^\mu = \left(A_0 + A_s\sqrt{\boldsymbol{S}_i:\boldsymbol{S}_i - \boldsymbol{W}_i:\boldsymbol{W}_i}\frac{k_i^2}{\varepsilon_i}\right)^{-1} \quad , \tag{5-43}$$

with $A_0 = 4.0$ and A_s given by:

$$A_s = \sqrt{6}\cos\left[\frac{1}{3}\cos^{-1}\left(\sqrt{6}\frac{S_i^{ij}S_i^{jk}S_i^{ki}}{S_i^3}\right)\right] \tag{5-44}$$

The remaining model coefficients for the realizable k-ε model are:

$$C_{\varepsilon 1} = \max\left(0.43, \frac{Sk}{\varepsilon\left(5 + \frac{Sk}{\varepsilon}\right)}\right) \quad , \tag{5-45}$$

$C_{\varepsilon 1} = 1.9$, $\sigma_k = 1.0$ and $\sigma_\varepsilon = 1.2$.

These equations form the basis of the commonly used two-parameter k-ε turbulence models within the RANS class. The effective viscosity ($\mu_{eff} = \mu + \mu_t$) is incorporated directly into the Navier-Stokes equation (Ferziger and Perić, 2002).

STAR-CCM+ provides a further the two-layer formulation within the boundary layer, which blends an one-parameter model (that solves for k, but prescribes ε algebraically with distance from the wall), with the two-equation k-ε models:

$$\varepsilon_i = \frac{k_i^{\frac{3}{2}}}{l_\varepsilon} \quad , \tag{5-46}$$

using the blending function (λ) prescribed by Jongen (1998):

$$\lambda = \frac{1}{2}\left[1 + \tanh\left(\frac{\mathrm{Re}_y - \mathrm{Re}_y^*}{A}\right)\right] \quad , \tag{5-47}$$

with:

$$A = \frac{|\Delta \mathrm{Re}_y|}{\tanh 0.98} \quad , \tag{5-48}$$

where $\mathrm{Re}_y = \frac{\sqrt{k_i}\, y}{\nu_i}$, $\mathrm{Re}_y^* = 60$ and $\Delta \mathrm{Re}_y = 10$ in STAR-CCM+ (CD-Adapco, 2011). The turbulent viscosity from the k-ε model are blended with the two-layer value:

$$\mu_i^t = \lambda\left(\mu_i^t\right)_{k-\varepsilon} + (1-\lambda)\mu_i\left(\frac{\mu_i^t}{\mu_i}\right)_{2\ \mathrm{layer}} \quad . \tag{5-49}$$

STAR-CCM+ further allows the implementation of an all-y+ wall treatment formulation using the blending function:

$$g = e^{\left(\frac{-\mathrm{Re}_y}{11}\right)} \quad , \tag{5-50}$$

with the reference velocity u* calculated depending on the model formulation selected:

$$u_i^* = \sqrt{\left(C_i^\mu\right)^{\frac{1}{2}} k_i} \qquad \text{; high-y+}$$

$$u_i^* = \sqrt{g\,\nu_i \frac{u_i}{y} + (1-g)\left(C_i^\mu\right)^{\frac{1}{2}} k_i} \qquad \text{; low-y+} \tag{5-51}$$

$$u_i^* = \sqrt{g\,\nu_i \frac{u_i}{y} + (1-g)\left(C_i^{\mu}\right)^{\frac{1}{2}} k_i} \qquad \text{; all-y+}$$

along with the wall-cell turbulence production:

$$G_i^k = \frac{1}{\mu_i}\left(\rho_i u_i^* \frac{u_i}{u_i^+}\right)^2 \frac{\partial u_i^+}{\partial y_i^+} \qquad \text{; high-y+}$$

$$G_i^k = \mu_i^t S_i^2 \qquad \text{; low-y+} \qquad (5\text{-}52)$$

$$G_i^k = g\,\mu_i^t S_i^2 + (1-g)\frac{1}{\mu_i}\left(\rho u_i^* \frac{u_i}{u_i^+}\right)^2 \frac{\partial u_i^+}{\partial y_i^+} \qquad \text{; all-y+}$$

and wall-cell turbulence dissipation with $\kappa = 0.42$:

$$\varepsilon_i = \frac{u_i^{*3}}{\kappa y} \qquad \text{; high-y+}$$

$$\varepsilon_i = \frac{2\nu_i k_i}{y^2} \qquad \text{; low-y+} \qquad (5\text{-}53)$$

$$\varepsilon_i = g\frac{2\nu_i k_i}{y^2} + (1+g)\frac{u_i^{*3}}{\kappa y} \qquad \text{; all-y+}$$

$$\varepsilon_i = \frac{k_i^{\frac{3}{2}}}{l_{\varepsilon}} \qquad \text{; two-layer all-y+ .}$$

5.4 Validations

CFD code validation and its applicability to solving particulate mixing in a mixing vessel was investigated by using various baseline simulations. These included settled particle volume fractions, replication of the rheology experiments, grid resolution effects on the numerical flow field predictions, turbulence model applicability, surface effects and particle suspension heights.

5.4.1 Settled volume fraction

Settled volume fraction determines the density of particles which settle naturally. In Eulerian-Eulerian type simulations all species are assumed to behave like a liquid or gas which completely settles out to a maximum volume fraction of $\alpha_{max} = 1$. Pressure force models are implemented to prevent complete particle settling from occurring and to limit the solid volume fraction occupied by the particle species. Both pressure force models (Equation 5-30 and Equation 5-32) were evaluated with a cylinder initially filled with solids to a particle volume fraction of $\alpha_p = 0.15$, and allowed to settle.

5.4.2 Rheology validation

Flow between concentric cylinders was modelled with the inner cylinder rotating at a strain-rate of 350 s^{-1}. The rheology machine geometry described in Chapter 4 (Figure 4-2), was used where *R1*= 11.9 mm, *R2*=12.3 mm, *R3*=13.3 mm and *R4*=13.8 mm and the effective length (*L*) of 40 mm. Particle concentrations of 20 g/L and 100 g/L were evaluated to determine the accuracy of CFD to reproduce experimental results.

5.4.3 Grid independence

Grid independence determines whether the mesh resolution used to represent the domain is fine enough to capture the significant flow field features and whether the discretised equation set solved the original differential equation set adequately. This implies that the grid resolution must be fine in regions with high velocity and pressure gradients and coarse in regions of low velocity and pressure gradients. Three grid resolutions were applied to the fermenter domain to determine at which resolution the significant flow features were sufficiently captured. This steady state simulation was conducted with only water present and the realisable k-ε model activated. Although these simulations do not invoke all the models used in the final investigations, the results are nonetheless highly relevant, as any number of phases in a mixture will experience similar flow fields, thus requiring similar grid resolutions and configurations.

The Bioflow 110 new Brunswick 1.3 L fermenter geometry (Figure 5-8) was used for the grid independent study. Simulations were done with the impeller rotating at 150 rpm with baffles in-place. They were conducted with 4 different polyhedral meshes containing 90 381, 164 898, 215 400 and 411 158 cells with maximum cell sizes of 6 mm, 4.5 mm, 4.0 mm and 3 mm respectively, where cell sizes are defined as the average distance across faces of the polyhedral cell. Hereafter these meshes are respectively referred to as coarse, medium, fine and finest.

5.4.4 Turbulence models

Turbulence models account for the Reynolds shear stresses and boundary layer effects in order to reduce the computational effort required to solve the stresses directly. This means that the assumptions of the model introduce errors to the flow field solution. Selecting the correct model is therefore crucial for obtaining the correct results. STAR-CCM+ v 6.02.007 provides a limited number of turbulence models for its segregated multiphase Eulerian simulations, with only the *k-ε* turbulence models available. There are three variations of the model available in the current version of the code. These are the so-called low Reynolds, standard high Reynolds and realizable models which can be applied to a high y^+, low y^+ and hybrid (all-y^+ two-layer approach) meshes, respectively.

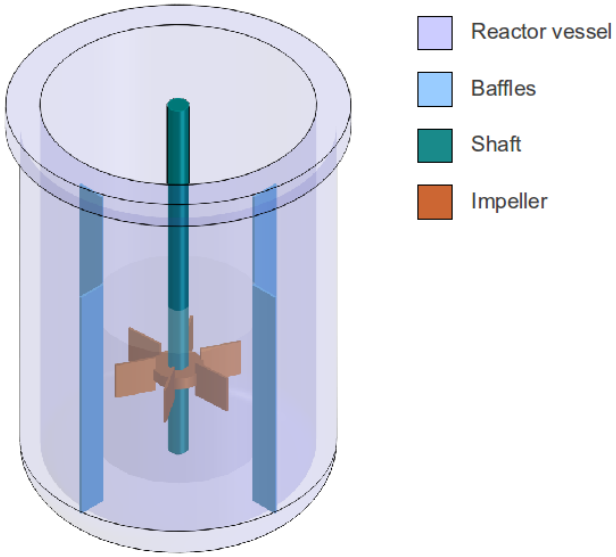

Figure 5-8: Computer aided design drawing of the reactor geometry

The characteristic feature of the low Reynolds approach is that the boundary layer is resolved, therefore providing increased boundary layer accuracy. However, these models require approximately 15 or more prism layers within the boundary layer region with the first wall node centroid situated at a location distance from the wall to ensure a y^+ value of near 1. This method requires excessive computational effort and is for most engineering applications unnecessary.

High Reynolds models overcome the requirement of resolving the boundary layer directly by using wall functions, which assumes a turbulent boundary layer profile within the first wall cell centroid. The primary requirement is that the y^+ values for turbulent flow must be between 30 and 100, or in the logarithmic sub-layer. Thus only 1 prism layer is required to apply the assumed boundary layer profile at the wall nodes, with an additional layer preferred to transition the bulk flow into the boundary layer profile. While this model may in certain flow conditions be less accurate, it does significantly reduce the computational effort requirements to such an extent to allow reasonable computational turnover.

The hybrid scheme, or all $y+$ two-layer approach, combines the best of both worlds by blending the two afore-mentioned models to resolve the boundary layer where the mesh is sufficiently fine, or impose a wall-function where the mesh is too coarse. This approach is at least as accurate - if not more - as the standard high Reynolds approach due to the enhanced turbulence damping within the boundary layers when blending occurs and was selected for all turbulence simulations.

The Reynolds number for the fermenter operating conditions is in the transition flow region $10 < Re_d < 2\text{x}10^4$. To determine which turbulence models is most

appropriate, three steady-state simulations where conducted on a single-phase reactor mixing case. The first was performed with a laminar flow assumption, and the remaining two simulations were conducted with the standard and realizable k-ε models respectively. These simulations where conducted on a fine mesh with 215 400 polyhedral cells. A further transient simulation was conducted for the laminar model. An estimate of the Kolmogorov length-scale was calculated according to Nere *et al.* (2003).

5.4.5 Surface effects

Free-surface effects have the potential to significantly influence the flow field of a mixing vessel due to the pulsating pressure variations at this interface. To determine whether capturing of the free-surface is necessary, two simulations were conducted and compared to experimental footage. The first included a liquid viscosity of 0.831×10^{-3} kg/m·s to simulate the case where only the nutrient rich medium was present in the fermenter. The second assumed an extremely viscous liquid with a dynamic viscosity of 1.0 kg/m·s, to determine the worst case scenario. Both simulations were conducted utilising a sliding grid methodology, with the impeller rotating at 150 rpm.

5.4.6 Particle suspensions

The primary purpose for agitating a fermenter is to distribute the constituents thereof throughout the vessel and maintaining sufficient particle suspension. Three simulations were conducted at impeller velocities of 0 rpm, 75 rpm and 150 rpm and compared to experimental observations. Both the latter simulations were conducted using the sliding grid methodology with 100 g/L of microcrystalline cellulose particles, initialised as a complete homogeneous mixture. Time required for a steady type solution was found to be 8 s for the 150 rpm case and 32 s for the 75 rpm case.

5.5 Results

5.5.1 Settled volume fraction validation

The results from the settling simulation with no pressure force models enabled allow the particles to settle completely to a volume fraction of α_s=1. Two pressure force models were evaluated to determine the effectiveness of each in limiting the particle volume fraction during settling. The standard pressure force model provided by STAR-CCM+ is based on the pressure model proposed by Symlal (1985). This model was capable of preventing excessive settling, but is highly unstable and overruns the predetermined maximum settling value by almost 10 %. The pressure force model proposed in this dissertation (Equation 5-37) proved significantly more stable and under-predicted the maximum settling volume fraction by less than 5 %, (Figure 5-9).

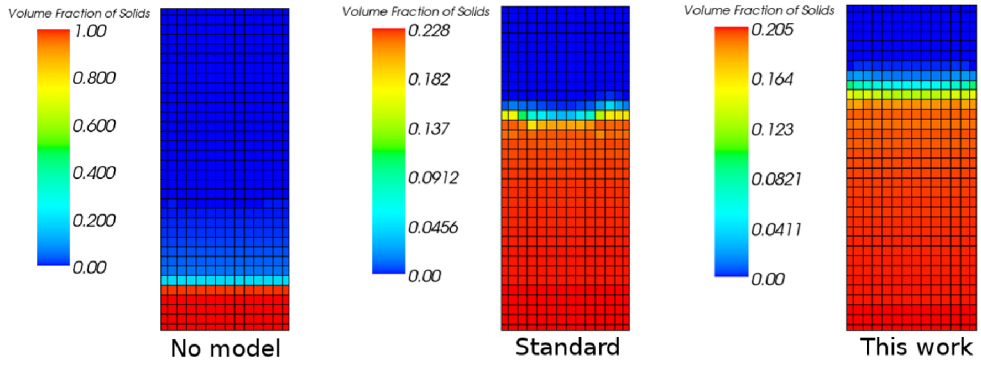

Figure 5-9: Comparison of the pressure force settling models

5.5.2 Rheology validation

Rheology experiments were performed starting from a shear-rate of 350 s^{-1} and decreasing it stepwise to 0.01 s^{-1}. This ensured a complete homogeneous particle distribution within the rheology chamber. Rheological simulations were conducted and compared to the experimental results to evaluate whether the CFD was capable of capturing the same physical phenomenon.

Two particle concentrations were selected, namely 20 g/L and 100 g/L, which were both simulated at a shear-rate of 350 s^{-1} (Figure 5-10). Both simulations indicated settled particles at the base of the rheology chamber. It is expected that some particle settling may occur due to the 2 mm base gap, however, the simulations suggested a continuous settling of particles, which was not observed in the experimental results. Furthermore, the CFD simulations indicates a non-homogeneous particle distribution surrounding the rotating cylinder head. These distribution patterns are caused by settling and centripetal forces.

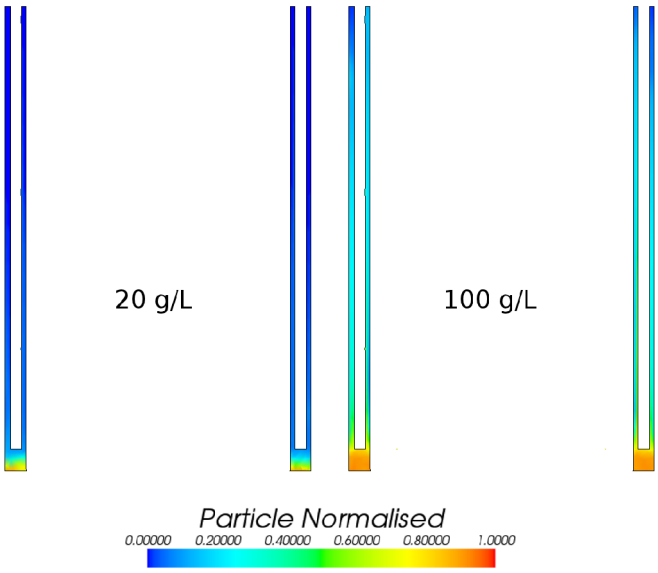

Figure 5-10: Particle distributions in a rheometer at a shear-rate of 350 s^{-1}

Comparison of the experimentally measured torque of 28.65 µNm and 68.66 µNm and CFD predicted torque of 25.3 µNm and 58.3 µNm for the 20 g/L and 100 g/L respectively indicated that the effect of the non-homogeneous particle distribution was significant.

5.5.3 Grid independence

Velocity (Figure 5-11 and Figure 5-12) and pressure (Figure 5-13 and Figure 5-14) profiles from the four line probes indicated that grid resolutions of 215 400 polyhedral cells or more are sufficient to capture the dominant flow fields which develop in the reactor geometry used in this study. Furthermore it is observed that the expected symmetry of the results from opposite line probes are only achieved at resolutions of 215 400 or higher.

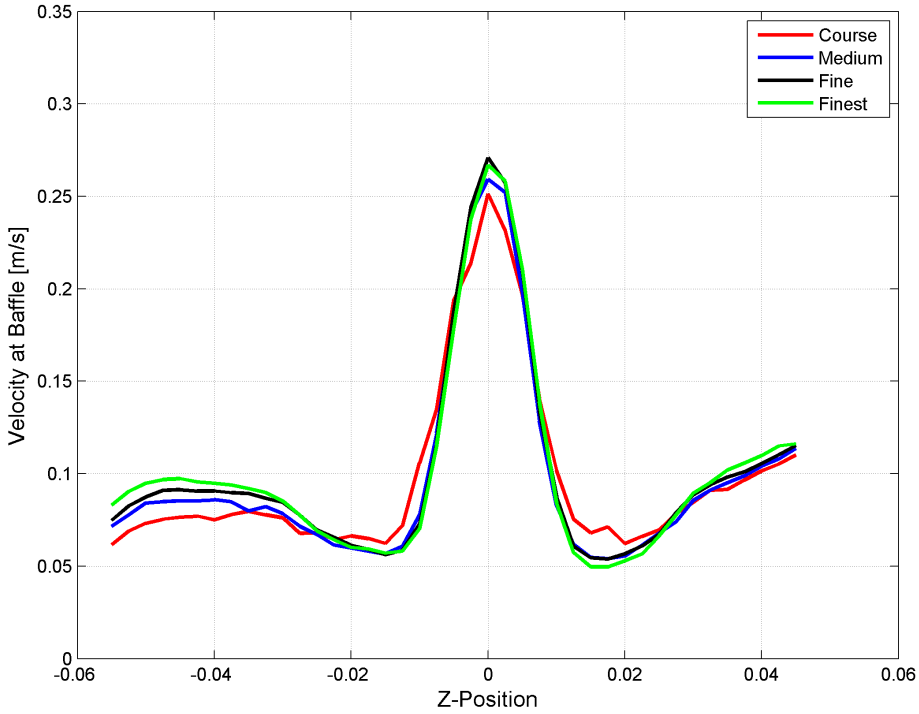

Figure 5-11: Velocity profile between impeller blade tip and baffle plate

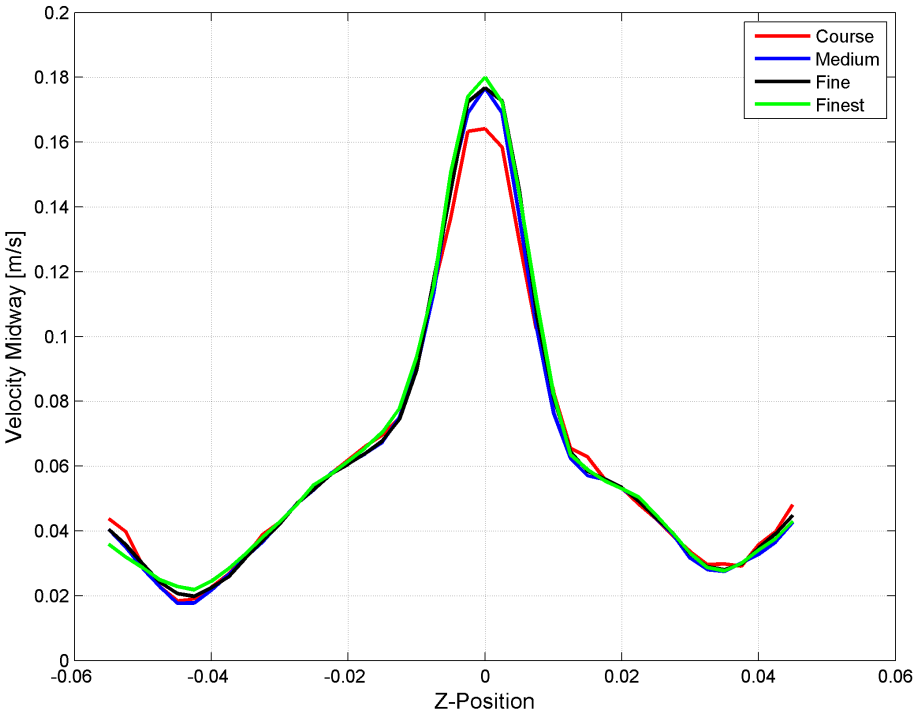

Figure 5-12: Velocity profile midway between baffles

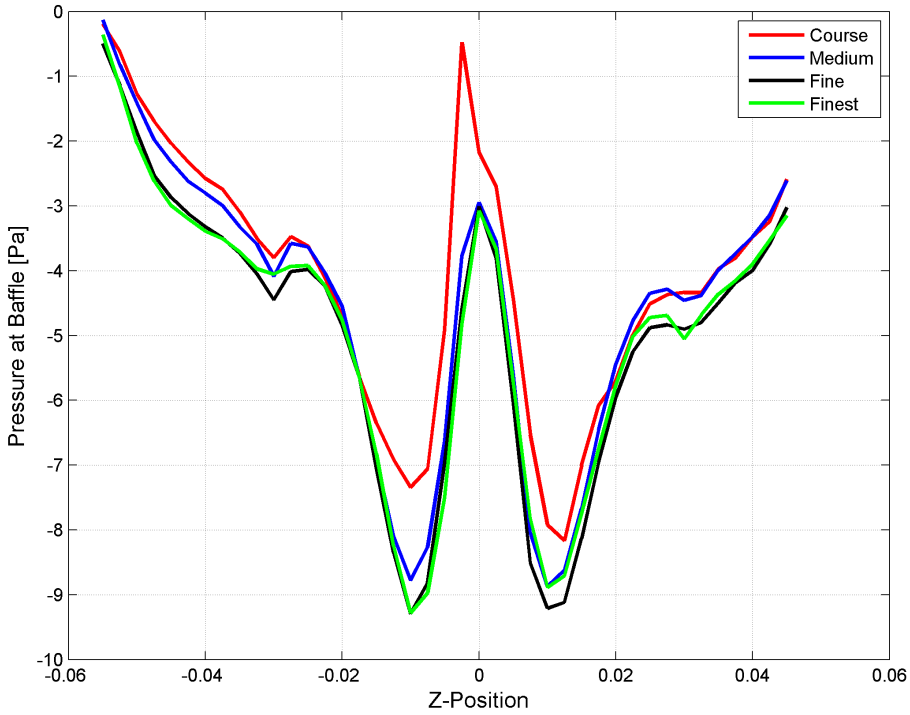

Figure 5-13: Pressure profile between the impeller blade tip and baffle

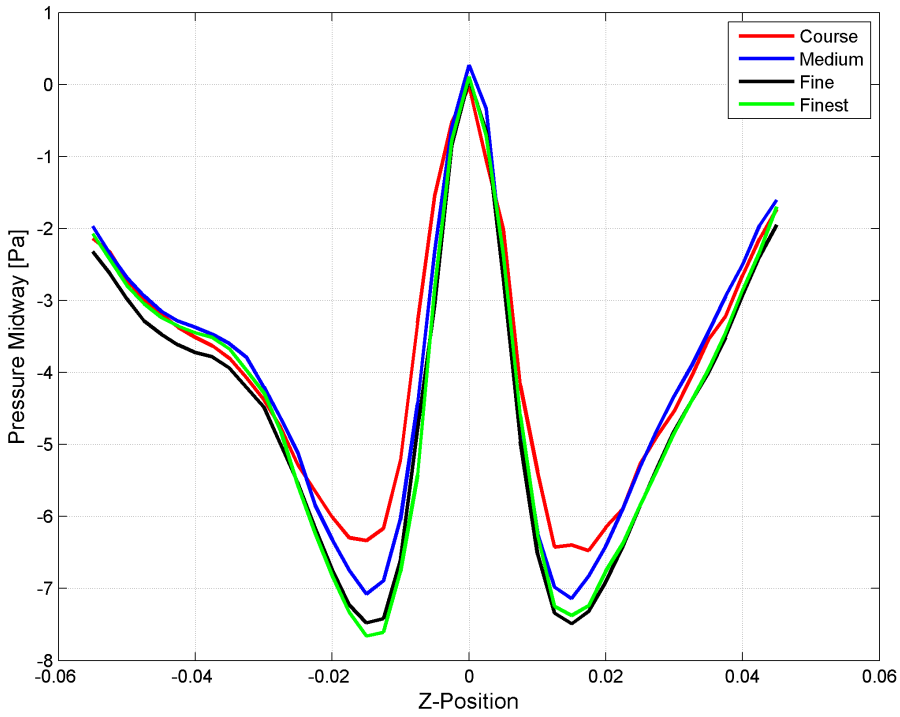

Figure 5-14: Pressure profile midway between baffles

5.5.4 Turbulence model

Results from the steady-state simulations indicated that the laminar and standard k-ε model simulations were unable to obtain a steady-state condition, while the realizable k-ε model provided consistent steady-state results on multiple grid sizes.

A transient laminar simulation was conducted on a mesh grid of 170 000 cells using a time-step of 0.001 s and 100 internal iterations per time-step. These settings proved sufficient to obtain converged solutions at each time-step. However, the results from this simulation indicated a highly chaotic flow pattern with large pressure pulses and no consistent repetition of flow patterns. This was indicative of insufficient grid resolution, as a mixing vessel will have a repetitive cycle as the blades rotate, which was not observed in the simulation results.

An approximation of the Kolmogorov length scale for the conditions within the reactor indicated that a cell size of less than 0.066 mm (across flats) would be required for laminar transient simulations to provide accurate solutions. This cell-size would require approximately 3.2 x10^9 cells, which would require a currently unavailable computational resources.

5.5.5 Surface effects

Surface effects are important during fermenter design, as excessive sloshing and splashing exposes the fermenting organism or enzymes to the violent forces and possible air exposure which may lead to severe organism stress or enzyme inactivation. Two simulations were conducted to examine the effects of viscosity on the free-surface to determine whether sloshing or splashing was a risk. Both simulations were conducted at 150 rpm with the low viscosity case displaying signs of rippling (indicated by the red arrows), but no splashing or sloshing. This is consistent with the experimental observations (Figure 5-15). Higher viscosities increase the resistance to inertial forces, effectively damping the ripple effect diminishing almost all free-surface effects.

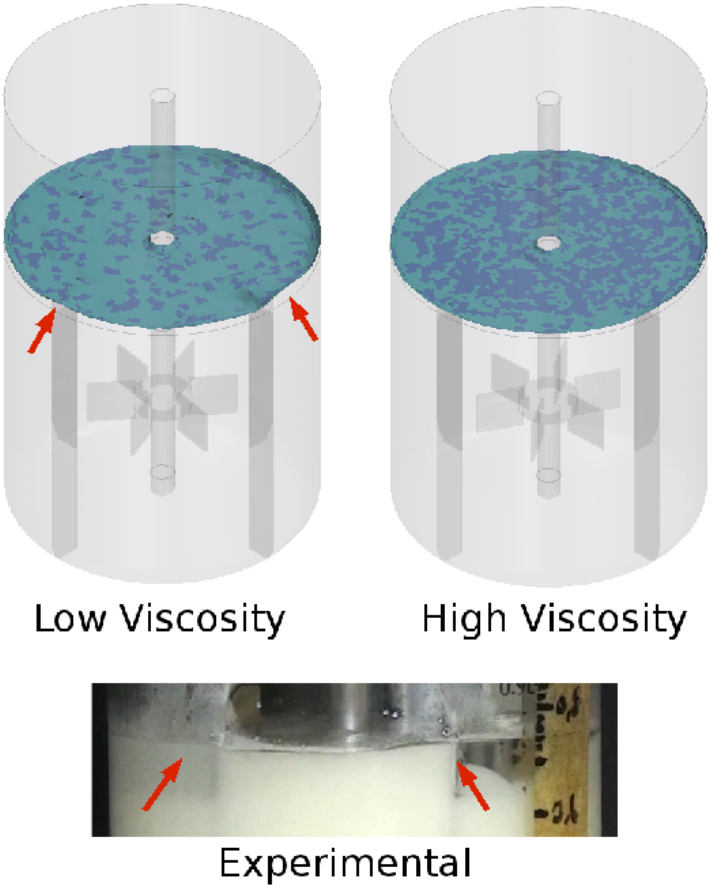

Figure 5-15: Effects of viscosity on free-surface

5.5.6 Particle suspensions

Comparison of the simulated particle suspension and fluid flow field results for 0 rpm, 75 rpm and 150 rpm impeller agitation speeds (Figure 5-16) with experimental observations (Table 5-1) indicated that CFD was capable of correctly predicting the occurrence of particle settling. These simulations predicted the particle settling pattern correctly 0 and 75 rpm, with the particles

settling on the outskirts of the fermentation vessels near the baffles at 75 rpm agitation speeds. These patterns were confirmed through visually observation of experimental video. The simulation for the 150 rpm case correctly predicted full off-bottom suspension which was consistent with the total particle suspension height observed experimentally. The case for 150 rpm agitation thus presented ideal conditions for maximum enzyme-substrate interaction and overall cellulose to ethanol conversion.

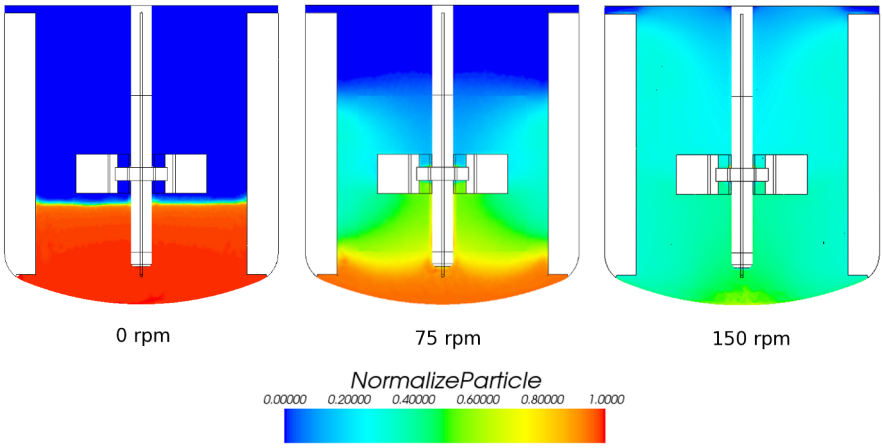

Figure 5-16: Comparison of simulations at various impeller speeds

Table 5-1: Experimental particle suspensions and surface effect observations

Impeller speed [RPM]	Surface effects	Particle suspension
300	Large waves with sloshing	Homogeneous
200	Medium size ripples	Complete off-bottom
150	Small ripples	Complete off-bottom
75	No visible effects	Partial suspension
50	No visible effects	Partial suspension
0	No visible effects	Complete settled

5.6 Discussions

5.6.1 Settled volume fraction validation

The model released with the STAR-CCM+ code (Equation 5-18) proved to be highly unstable and even with high relaxation factors and extremely small time steps, stability remained challenging. This work proposed an alternative formulation for the pressure force model (Equation 5-32) which proved to be more stable and remained on the conservative side of the maximum specified settled volume fraction.

5.6.2 Rheology validation

Rheology studies indicated that the CFD simulations under-predicted the torque compared to experimental results. This suggests that a set of physical models are missing: in this case it is the physics which describes particle interactions. Particle interaction models exist in literature, however, it was outside the scope of this specific project to evaluate the various particle interaction models. It was further determined that the incorporation of such a model is not a necessity due to the k-ε model which artificially induces a viscosity increase to model turbulence. The viscosity increase caused by the turbulence model far exceeded the effects of the particles in regions of high turbulence.

5.6.3 Grid independence

A grid independence study was conducted using four mesh resolutions. The results indicated that cell resolution in excess of 200 000 cells proved sufficient to resolve the dominant flow field using the Reynolds Averaged Navier-Stokes realizable k-ε turbulence model.

A pressure spike is observed Figure 5-13 for the coarse mesh. This spike was caused by the large difference between two adjacent cell sizes leading to a poor interpolation at the probe point. This error was resolved at the higher grid resolutions.

5.6.4 Turbulence model

Comparison of the laminar, standard k-ε and realizable k-ε models using the two-layer all-y+ wall treatment methodology, indicated that for the current study the latter model is more appropriate. This model provides the best compromise between the laminar and turbulent conditions and was found to provide consistent results under a wide variety of conditions.

Simulations using the laminar model approach revealed that the grid resolution was too coarse. Calculations were conducted to approximate the correct grid resolution required for laminar simulations. The results indicated that approximately 3.2×10^9 cells are required, which was impossible to achieve with the available computational resources. The standard formulation of the k-ε model proved incapable of obtaining a converged solution and was thus rejected.

5.6.5 Surface effects

Surface effects can have a significant influence on the performance of a fermenter, as it may result in a hostile environment for the fermenting microbes or simply disrupt the flow. Surface effects may be caused by the introduction of baffles into the fermenter. However, the introduction of baffles are essential to disrupt the vortex effect caused by rotating impellers. However, excessive mixing may lead to splashing and sloshing which aerates the medium, possibly leading to enzyme deactivation (Kim *et al.*, 1982).

Results from this study indicated that for the operating conditions of 150 rpm in a

1.3 litre reactor with a baffle configuration, the surface effects were negligible. This permits a simplification of the free-surface as a flat non-slip wall boundary.

5.6.6 Particle suspensions

Particle suspension is a requirement to maximise the particle surface exposure to the soluble components in the medium. Insufficient agitation may lead to particles depositing on the bottom of the fermenter. If this sedimentation becomes thick enough, contact between underlying particles and the bulk medium decreases, reducing the overall performance of the fermenter.

The CFD simulations correctly predicted the primary characteristics of the particle suspensions, specifically when complete settling, partial suspension and complete off bottom suspension occurred. This confirmed the applicability of the drag and segregated multiphase Eulerian flow approach.

5.7 Conclusions

Various physical models and aspects on CFD were discussed with primary focus on drag, solid pressure force, rheology, grid independence and turbulence models.

Four drag modelling schemes were evaluated and it was found that the Syamlal and O'Brien (1988) model was applicable to the present study.

Solid pressure force models were investigated using the standard and modified model provided by the STAR-CCM+ version 6.02.007. These models proved to be highly unstable and prone to over-predict the maximum settling density of the particles. It was thus proposed to use a different formulation of the model, which proved more stable over a larger range of settling densities while higher resistance to overrun was introduced.

CFD results of the rheological flow conditions indicated that a significant percentage of the particles settles out of the active region resulting in lower torque prediction than expected from experimental results. These discrepancies could possibly be attributed to the lack of particle interaction models. Nonetheless, results compared favourably with experimental results, indicating that the viscosity models proposed in Chapter 4 are valid for the current study.

The grid independence study indicated that mesh resolutions in excess of 200 000 cells are sufficient for capturing the prominent flow fields of the 1.3 L reactor in this study. This is however using a Reynolds Averaged Navier-Stokes approach with the realisable k-ε turbulence model. This falls well within the range of resolutions reported by other studies, which range from as low as 60 000 cells (Moilanen *et al.*, 2005) to as high as 1 640 000 cells (Meroney and Colorado, 2008). Turbulence modelling schemes such as large eddy simulations (LES) and detached eddy simulations (DES) require significantly higher resolutions, as the large scale eddies are resolved directly. These models were not available in the multiphase solver of STAR-CCM+ at the time of writing and could therefore not be evaluated.

The effects of various turbulence models on the flow predictions of CFD methods are important as different models are designed for specific situations. Only the k-ε turbulence models were available for use with the multiphase solver and differences in the standard, realizable and laminar models were investigated.

6 MODELLING A FERMENTATION VESSEL

6.1 Abstract

The development of reaction kinetics and particle transport models for reactor design is necessary to capture all the significant physical effects and to determine their interactions. The influence of the kinetic reactions on the particle sizes and mixture's molecular viscosity as well as the influence of particle distribution on the effective reaction rates are discussed. The agitation power requirement based on conventional similarity laws are also examined. Results indicated that as cellulose conversion occurs, the average particle diameter decreases. This reduced the drag forces required to suspend the particles, and thereby increased the homogeneity of the particle distribution. The particle distribution was found to influence the reaction rates significantly. The agitation rate of 150 rpm produced a complete off-bottom particle distribution, with the reaction rates nearly identical to the homogeneous case. The case where agitation was 75 rpm, settling had occurred, which significantly reduced the rate of ethanol production indicative that enzyme inhibition was occurring. The final case where no agitation was applied the particle had completely settled resulting in a significant reduction in reaction rates due to product inhibition.

6.2 Introduction

By combining the results from the kinetics model (Chapter 3) with the mixing conditions determined by a CFD package and the apparent dynamic viscosity model from Chapter 4, engineers are able to investigate and improve the design of cellulose to ethanol fermenters. It is primarily not feasible to design large fermenter units which operate at high impeller revolutions with large impeller geometries, as this increases the shear-rates which the organisms experience. This may result in possible decreased production yields and inefficient conversion of cellulose to ethanol. This is not the case in this study and was not further investigated.

6.3 Methods and Materials

6.3.1 Software

STAR-CCM+ version 6.02.007 (CD-Adapco, London, UK) was used to perform the CFD simulation present in this study. The kinetic reactions (Chapter 3) were calculated using a separate user code written in C and compiled using GCC, an open source GNU C compiler. Limitations within STAR-CCM+ did not permit the kinetic reaction models to be directly incorporated into the CFD software.

6.3.2 Geometry

The Bioflow 110 New Brunswick 1.3 L fermenter geometry was utilised for the simulations. Simulations included the impeller, impeller shaft and baffles (Figure

5-8), with the free-surface modelled as a frictionless wall. The impeller was set at one impeller diameter height from the bottom of the fermenter. This proved sufficient to provide a fully off-bottom suspended fermentation environment at impeller speeds in excess of 150 rpm. Agitation was maintained at the recommended rate of 150 rpm. Higher agitation rates were observed to induce excessive splashing and foaming, which is undesirable as it may accelerate enzyme deterioration.

Mesh Generation

Polyhedral cells were selected for the simulations due to their reduced numerical false diffusion errors in unstructured flow environments and their ability to automatically produce fully conformed internal interface coupling in complex geometries. The discretised grid generated for the simulations contained 463 333 cells with a minimum and maximum cell size limit of 0.15 mm and 2.5 mm respectively. The mesh was further grown from the geometry surfaces with the finer cells situated near regions of high gradients, such as around the impeller and baffles. Complex geometry could thus be captured while sufficiently resolving the average velocity and pressure fields present in the reactors.

The domain of the geometry was divided into two regions (Figure 6-1): an inner rotating region (indicated by the red tinted region), which included the impeller and a part of the shaft and an outer stationary region (grey region), which houses the baffles as well as the remaining rotor shaft and reactor shell.

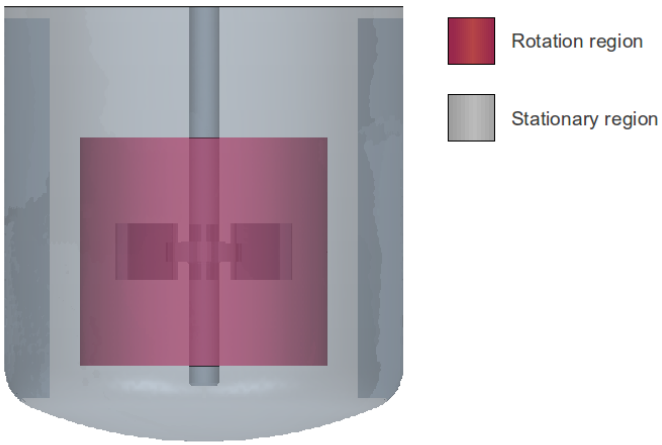

Figure 6-1: Inner rotating and stationary regions for the mixing vessel

6.3.3 Physics models

Multiphase model

Simulations were conducted in a three-dimensional representation of the fermentation vessel, using a full Eulerian-Eulerian model approach utilising the segregated multiphase flow formulation (Equations 5-10 to 5-15). The volume fraction imbalance option was invoked to improve the stability of the volume solver by ensuring that the linear solver always received a diagonally dominant matrix at every iteration. The method used to ensure the diagonally dominant matrix was not available from the software company CD-Adapco. The volume fraction imbalance option requires significant computational power but reduces the necessity for excessive numerical relaxation.

The reactor contents was divided into two discrete phases: the continuous phase which represents the fermentation medium and the solids phase which represented the Avicel (cellulose) particles. The continuous phase was modelled as a liquid with the density and viscosity determined by (Equation 4-5 to Equation 4-10), as ethanol and glycerol were found to significantly affect the liquid phase properties. The concentration of yeast remained low and its effects were therefore not included. The Avicel was modelled as dispersed particles, with the average diameter specified as 1.41×10^{-4} m at the initial state. The diameter was modified according to:

$$D_{\text{eff}} = D_0 \sqrt[3]{(1 - x_c)} \tag{6-1}$$

to account for the change in inter-phase forces, such as drag lift and turbulent dispersion throughout the reactions. Where D_0 is the initial diameter of solids present in the fermenter, and x_c is the degree of conversion for the Avicel particles. Conversion is therefore modelled as a shrinking core mechanism, with the particle size decreasing as conversion occurs.

The effects of the particle concentration on the apparent viscosity was modelled with Equation 4-14, Equation 4-16 and Equation 4-17. This formulation proved effective, as the CFD code uses Equation 4-15 to determine the apparent dynamic viscosity of the each cell.

The inter-phase models for drag, lift and turbulent dispersion were modelled using the Syamlal and O'Brein (1988) drag correlation (Equations 5-21 to 5-25), Auton *et al.* (1988) lift equation (Equation 5-26) and Equation 5-28 for the turbulent dispersion respectively. The pressure force experienced by the particles in the flow when settling was accounted for by Equation 5-32.

Reaction model

To account for the non-homogeneous particle distribution within the reactor, kinetic models were calculated on a per cell basis. Concentrations of each reactor constituent was calculated for each cell at every time-step. All the soluble constituent concentrations were averaged between each time-step, while maintaining the insoluble cellulose particle distribution. The averaging was performed to ensure that soluble constituents remain homogeneous throughout the fermenter (Figure 6-2), as measured experimentally. This averaging step was, however, not performed during the stationary fully settled simulation as no convective transport forces were present. The reaction rates within the reactor were calculated from Equation 3-2 to Equation 3-14 (Chapter 3).

Turbulence model

At the time of writing STAR-CCM+ only provided two options for modelling turbulence within the segregated Eulerian flow model. These options were: laminar or the RANS eddy-viscosity k-ε models. The latter was divided into the low Reynolds, standard high Reynolds and the realizable high Reynolds number models. Investigations in Chapter 5 indicated that for this study the realizable k-ε model performed best in capturing the average velocity and pressure profiles.

Discretization

Rigid body motion and the sliding methodology was used in all CFD simulations presented in this chapter. A first-order implicit unsteady formulation was utilised to simulate the time-stepping through each simulation.

Transport equations were discretised with a second-order upwind scheme and solved with an algebraic multi-grid solver. This was the highest order scheme available with the segregated Eulerian multiphase solver in STAR-CCM+. Relaxation factor selected for velocity, pressure and volume fraction was 0.5, 0.3 and 0.3, respectively.

6.3.4 Boundary and initial conditions

All surfaces were assigned the non-slip wall boundary condition, except the free-surface, which was modelled as a frictionless (slip) wall (see section 5.6.5). The sections of the shaft not included in the rotating region was assigned a tangential rotational velocity of either 0 rpm, 75 rpm or 150 rpm, respectively.

Sliding grid simulations required rigid body motion, which physically rotates a portion of the geometry to mimic the effect of a rotating impeller. This was achieved by assigning a rotational motion and an associated reference frame of 0 rpm, 75 rpm or 150 rpm, respectively, around the central axis of the shaft to the rotating domain in the mesh.

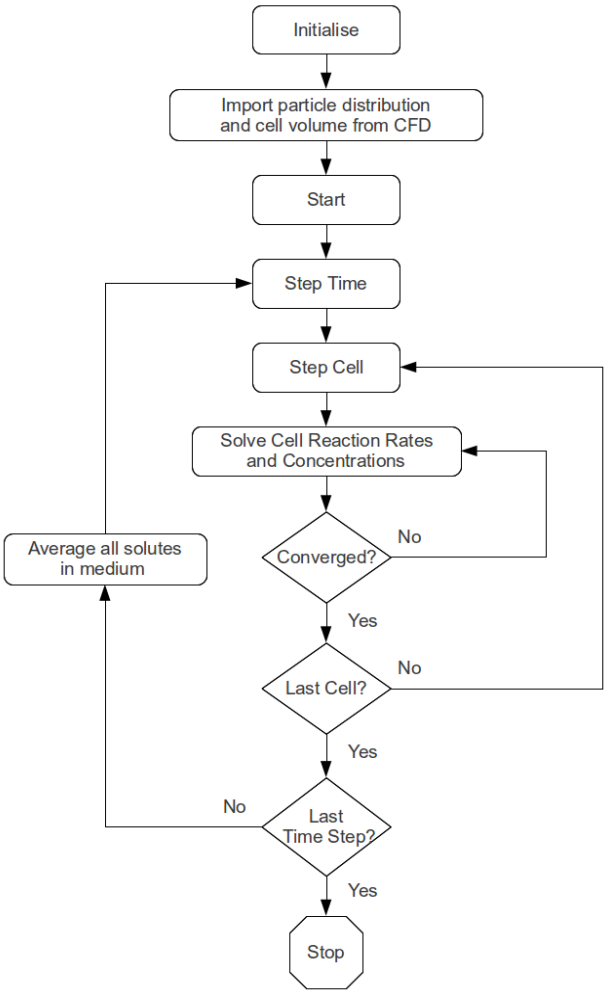

Figure 6-2: Flow diagram of the reaction kinetic algorithm used in this study

Simulations were initialised at atmospheric pressure (101 325 Pa). A rotational velocity of 0.001 m/s in the circumferential direction of impeller rotation, with all other velocity components initialised at 0 m/s. Turbulence was initialised with an intensity of 1 %, a velocity scale of 1 m/s and a maximum viscosity ratio of $\mu_t / \mu = 10$. All simulations were run for 2 000 steady-state iterations with the volume fraction solver frozen to calculate an approximate flow and pressure field. Thereafter the volume solver was released and the simulations continued with transient sliding grid conditions for 8 s (150 rpm impeller speed) or 30 s (75 rpm impeller speed) at a time-step of 6.67×10^{-3} s with each time step requiring 50 iterations to reach convergence. Reference values for gravity, minimum allowable wall distance (minimum cell thickness near the wall), density and pressure were assigned as 9.81 m/s^2, 10^{-6} m, medium density determined from Equation 4-10, and 101 325 Pa , respectively.

6.3.5 Case studies

The benefits of simultaneously modelling the distribution of particles and reaction rate influences are demonstrated with three case studies. The first case evaluates the effects of particle conversion on the distribution of particles throughout the fermentation vessel. The methodology followed included performing a CFD simulation using the initial particle properties to determine the distribution of particles throughout the vessel. This information was fed into the external reaction kinetics model to determine the new average particle size and fluid composition at 20 % conversion intervals. These properties were fed back to the CFD simulation to compute the new distribution of particles. This process was repeated until a theoretical complete conversion was obtained.

The second case study involved the effect of the distribution of particles on the reaction rates within the vessel. The initial particle distribution was determined for perfect homogeneous mixing and for 0 rpm, 75 rpm and 150 rpm agitation rates. This information was fed to the external kinetics model, which calculated the reaction rates at these three initial states without updating the CFD for new distributions of the particles.

The third case was a theoretical comparison of power requirements for various agitation rates based on the results of the first two cases and typical agitation rates for cell cultures used in literature. The calculations were performed using turbo-machinery laws for power (Paul *et al.*, 2004). The Reynolds number for the impeller was calculated using the impeller rotational rate and diameter:

$$\mathrm{Re} = \frac{\rho N D_i^2}{\mu} \quad . \tag{6-2}$$

Power was further calculated from the power equation using the approximate turbulent power number (N_p) of 5 for the Rushton type impeller:

$$P_o = N_p \rho N^3 D_i^5 \quad . \tag{6-3}$$

6.4 Results

6.4.1 Effects of reaction on particle distribution

Hydrolysis of the cellulose particles caused the average cellulose particle diameter to decrease while increasing the concentrations of ethanol and glycerol in the mixture. These effects resulted in an improvement of particle homogeneity as the reactions continued (Figure 6-3), as smaller particles possess less mass and therefore require less force to transport.

Flow through the fermenters at 150 rpm agitation (Figure 6-4) during the course of the cellulose conversion process remains mostly constant, except near the bottom of the fermenter. Here the flow is significantly retarded during the initial stages of the reaction by a higher concentration of particles. As the conversion process continues, the particle concentration near the bottom of the fermenter reduces allowing more fluid flow to occur.

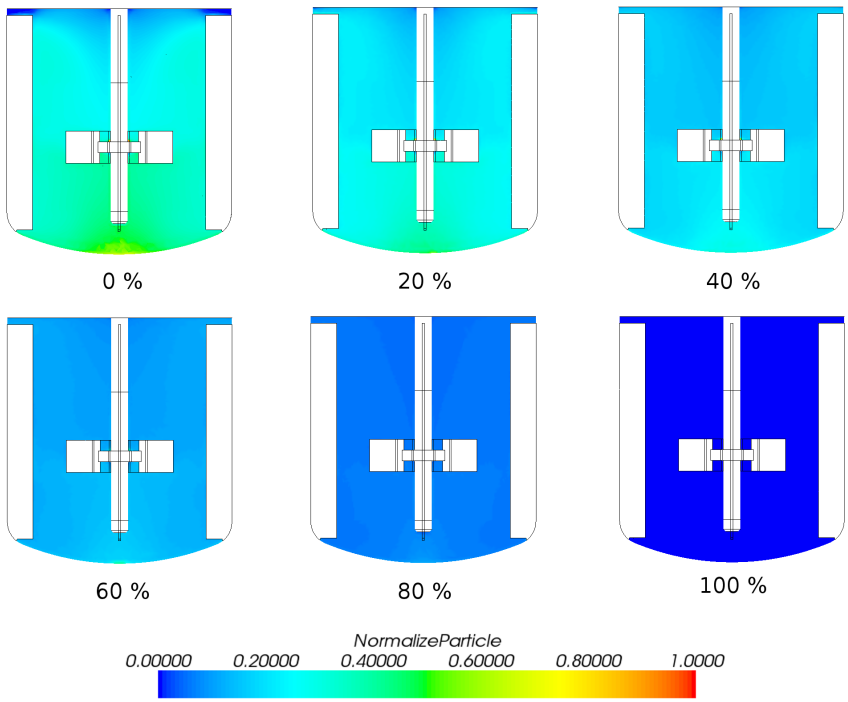

Figure 6-3: Avicel particle distributions as predicted by CFD at various state of conversions of conversion at 150 rpm

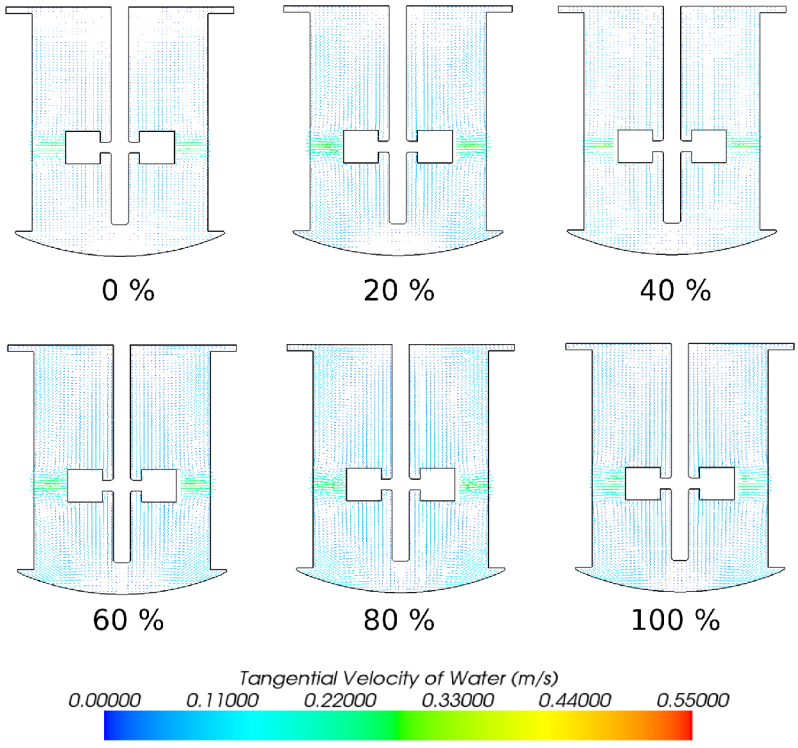

Figure 6-4: Velocity vectors for flow through the fermenters at 150 rpm

6.4.2 Effects of the particle distribution

Four particle suspension profiles were investigated, namely fully homogeneous particle suspension, as well as the initial particle distribution for the 0 rpm, 75 rpm and 150 rpm mixing conditions. This isolated the particle distribution as the only influence on the reaction rates. Results indicated that at 150 rpm the reaction rates were almost identical to the homogeneous case (Figure 6-5 and Figure 6-6).

A significant decrease in the ethanol production rate was observed for the cases of 0 rpm and 75 rpm (Figure 6-6). For the fully settled case, where no agitation occurred, ethanol concentrations will reached the critical inhibition concentration (Figure 6-6) for the yeast. In the 75 rpm agitation case, cellulose conversion rates appeared to exceed the homogeneous theoretical maximum (Figure 6-5). The average ethanol concentration in the reactor was predicted to reduce (Figure 6-6), as less enzymes and yeast cells are available at the higher cellulose concentration, compared to the homogeneous case, resulting in lower ethanol production.

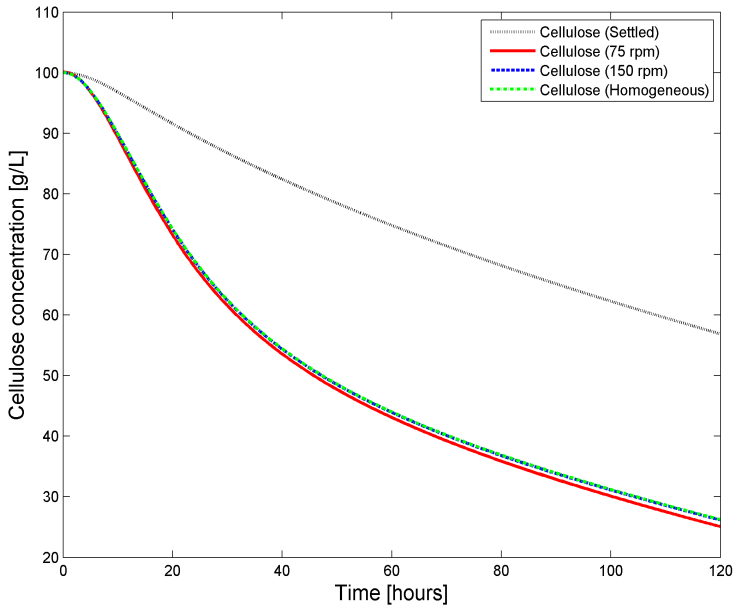

Figure 6-5 Cellulose concentration for settled and 75, 150 and homogeneous agitation rates

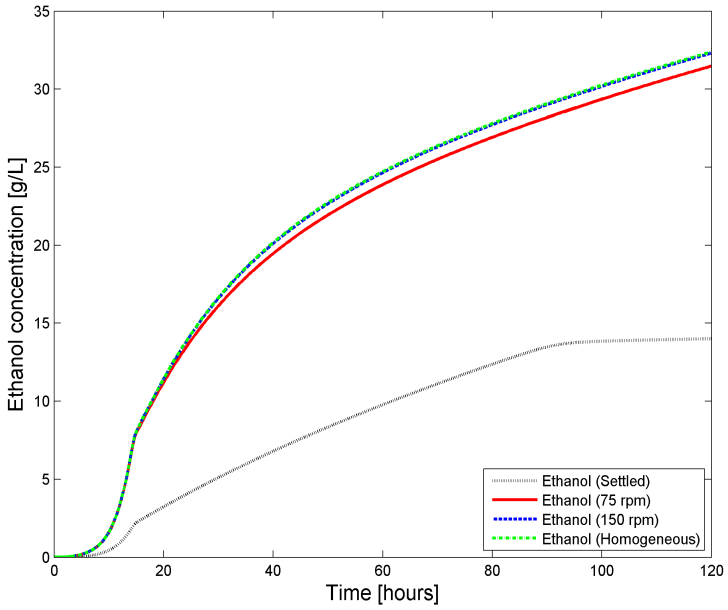

Figure 6-6: Ethanol concentration for settled and 75, 150 and homogeneous agitation rates

Investigation of the adsorbed enzyme concentrations indicate that the averaged number of attached enzymes throughout the fermentation vessel were lower for the case of 0 rpm and 75 rpm than for the homogeneous and 150 rpm conditions (Figure 6-7 and Figure 6-8). The fully settled case adsorbed enzyme are significantly lower than the agitated simulations.

6.4.3 Power requirements

Agitation power is a critical parameter for the design of efficient fermenters. Using the Equation 6-3 to estimate the power requirement and varying the impeller rotation rate and impeller diameter, whilst the remainder of the parameters are kept constant, provides insight into the sensitivity of a fermentation vessel to size and speed (Figure 6-9). Comparisons indicate that for an impeller twice the size in diameter operating at the same rotation rate, the power requirements would increase 30 fold, while doubling the impeller speed and keeping the impeller diameter constant would require a power 7 times greater.

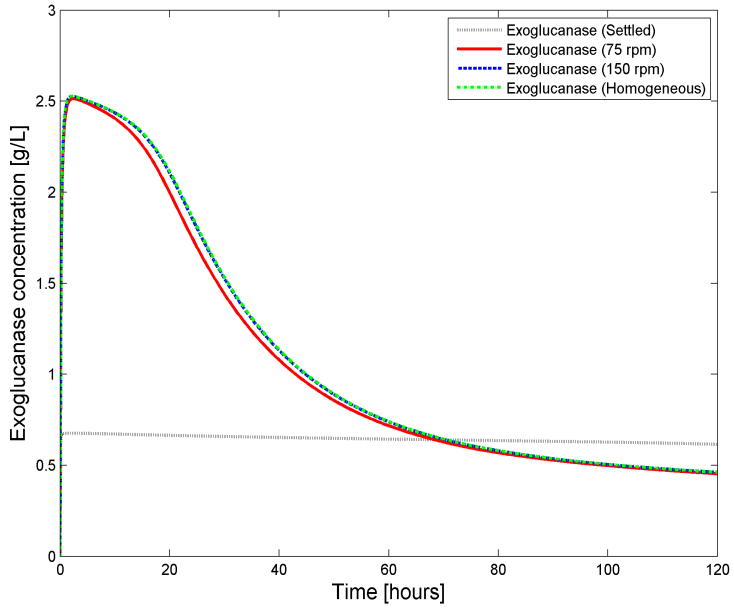

Figure 6-7: Exoglucanase protein concentration for settled and 75, 150 and homogeneous agitation rates

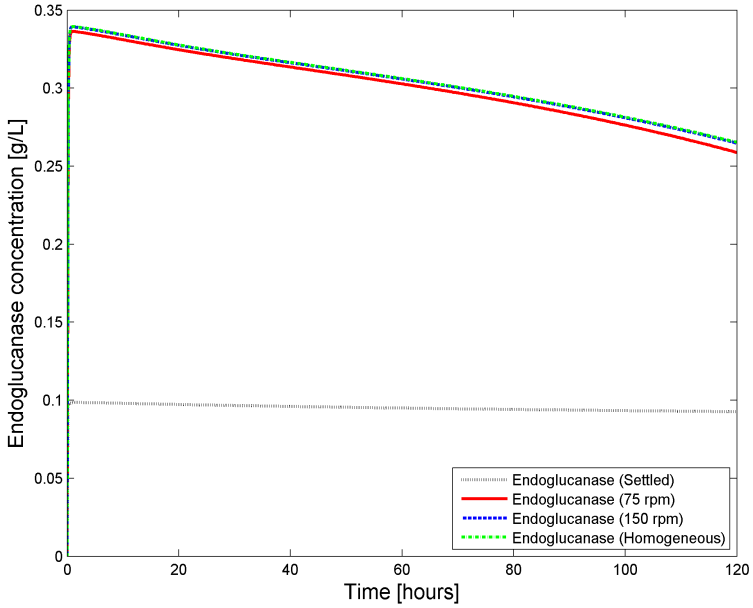

Figure 6-8: Endoglucanase protein concentration for settled and 75, 150 and homogeneous agitation rates

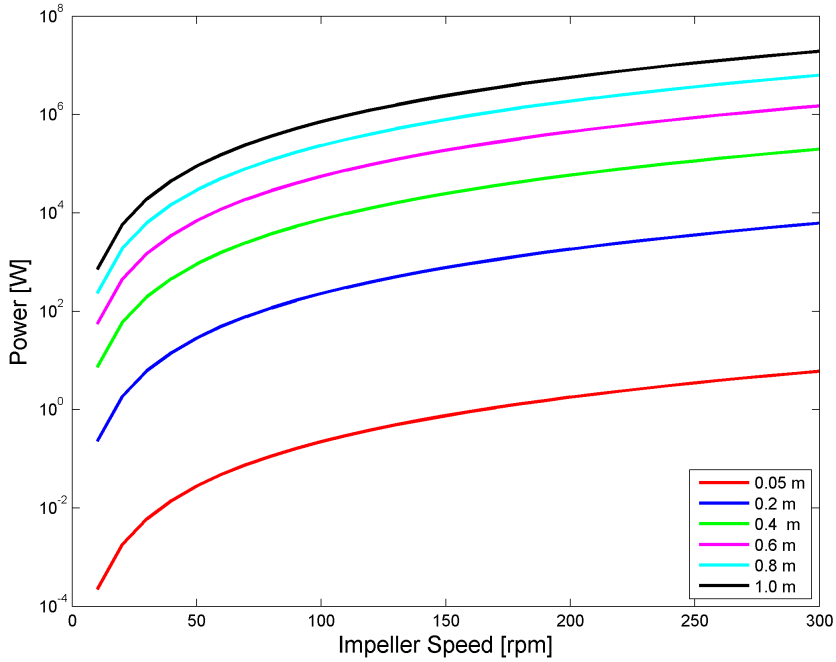

Figure 6-9: Effect of impeller speed and diameter on the power requirement of a Rushton type impeller

6.5 Discussion

6.5.1 Effects of reaction on particle distribution

Conversion of the cellulose particles had two primary effects on the Avicel particles. The first is the reduction in the average particle diameter. These smaller particles required less drag forces to be transported throughout the fermentation vessel. The secondary effect of the particle conversion is the redistribution of the cellulose particles throughout the vessel. This causes the particles to be transport higher up with the flow fields in the reactor as gravity forces are reduced. The production of ethanol and glycerol in the mixture further increases the viscosity of the fermentation medium, this improves the transport capability of the flow for particles.

This observation provides the possibility to develop a control system which could actively adjust the impeller rotation rate during the course of the reactions to ensure the minimum particle suspension required without negatively influencing the conversion rates of the system, while simultaneously limiting the impeller power consumption.

6.5.2 Effects of the particle distribution

Three different agitation conditions were investigated to determine the effect of particle distribution on the effective reaction rates of the fermentation process. Theoretically, a perfect homogeneous particle distribution would deliver the highest possible average reaction rates and conditions throughout the fermentation vessel. Homogeneous conditions are often the target during reactor design, which results in excessive agitation.

On a laboratory scale, impeller rotation rates of between 150 rpm and 350 rpm have been documented for cell culture systems. Results from this study indicated that the difference in reaction rates for the 150 rpm case was negligible compared to the homogeneous condition. This suggests that for particulate substrates, designing for complete off-bottom suspension is the minimum condition required to obtain near perfect reactions.

The second agitation rate investigated was for an impeller rotation rate of 75 rpm. Results indicated that partial settling had occurred, causing a diminish exposure of the settled particles to the free enzymes in solution. Cellulose conversion rates appear to exceed the homogeneous theoretical maximum (Figure 6-5). This effect was as a result of the increase concentration of particles near the bottom of the reactor, which increased the amount of cellulose available in those cells and a local increase in conversion rates. These higher conversion rates influence the averaging process, predicting a greater average cellulose conversion. However, the average ethanol concentration in the reactor are predicted to reduce (Figure 6-6), as less enzymes and yeast cells are available at the higher cellulose concentration, compared to the homogeneous case, resulting in lower ethanol production.

The final agitation rate investigated was for an impeller rotation rate of 0 rpm. Results indicated that complete settling had occurred. The lack of convective transportation of particles caused the accumulation of inhibition products including ethanol and glucose to reach maximum levels between the particles, resulting in a ineffective reaction to occur.

6.5.3 Power requirements

Power requirements are directly proportional to $\rho N^3 D_i^5$ (Equation 6-2), indicating that the impeller diameter has the greatest influence on the power requirements. The impeller rotational rate is the second most significant parameter to consider. This suggests that efficient fermenters should be tall and narrow with multiple impellers mounted vertically a short distance above one another, rather than short and bulky. This permits smaller impeller diameters which need only operate at the minimum rotational rate. Designing fermenters with this approach, especially large scale fermenters, can reduce operating costs and increase profitability. This however requires further numerical investigation.

A second factor to consider for power requirements is the geometry of the impeller. Radial flow impellers including the Rushton type used in this study may not be ideal for maintaining full off-bottom suspension, an alternative axial flow impeller design may be more suitable for this purpose. The advantage of axial flow impellers including the pitched blade type is a flow with a large mixing vortex at greater speeds. This will ensure greater particle suspension with lower power requirements, with power numbers between 1.2 and 1.8, depending on the impeller design (Paul *et al.*, 2004).

7 DISCUSSION AND CONCLUSIONS

7.1 Discussion

7.1.1 Kinetic model

The first objective of the project was to investigate a simple simultaneous saccharification and fermentation process to convert microcrystalline cellulose to ethanol. This process included modelling the enzymatic hydrolysis of the cellulose particles to polysaccharides, primarily cellobiose, which is further hydrolysed enzymatically to form glucose. The glucose is fermented by the yeast *Saccharomyces cerevisiae* to form ethanol, glycerol and carbon dioxide. This investigation allowed the development of a one-dimensional numerical model of the biological reactions under ideal conditions which could predict the reactor contents under ideal fully suspended conditions.

The heterogeneous nature of the cellulose substrate meant that adsorption models which include site competition between the different enzyme types are necessary. Chapter 3 presented a developed kinetic model, which utilised these requirements by separating the adsorption behaviour of the two enzyme groups. This improved prediction from previous models by capturing the initial high adsorption rate of the exoglucanase along with the rate release thereof as soon as available chain ends are depleted. Thus conversion is primarily limited by the rate of the endoglucanase enzymes to clip and produce new chain ends for the exoglucanase enzymes to process.

The remainder of the kinetic model focused on the fermentation of the glucose sugars to ethanol using well established models from literature. Results from the developed kinetic model compared favourably with experimental values with a maximum error of 3.8 %

The first objective of this study was therefore successfully completed and published (van Zyl *et al.*, 2010).

7.1.2 Mixing parameters

The second objective of the project required the analyses of the apparent dynamic viscosity of the bulk fluid in the reactors throughout such a biological process. Development of a numerical model which could approximate the apparent dynamic viscosity within the reactors was thus required for determining the fluid flow conditions to be used in CFD simulations. Each significant constituent within the reactors was investigated to determine which contributed to the final apparent dynamic viscosity. A simple model was proposed to approximate the final reactor conditions.

Before CFD can be utilised to model particle transportation through a flow field the characteristics of the particles are required. Chapter 4 investigated the effects

of settling and determined that the average particle had similar drag coefficients as a spherical particle with an effective diameter 3 fold larger (0.141 $x10^{-3}$ m) than the actual particle (0.05 $x10^{-3}$ m). This suggested that the irregular shapes (Figure 4-1) of these particles increase the drag experienced. It is also noted that cellulose has a tendency to develop a layer of structured water around its surface, which effectively increases the particle size seen by the continuous fluid (Matthews *et al.*, 2006). It was found that isolated particles had an average settling rate of approximately $6.53x10^{-3}$ m/s and a natural settled volume fraction of 0.21.

Rheological studies on the effects of ethanol, glycerol, base medium, oligomers and Avicel particles indicated that the particles had the greatest influence on the apparent dynamic viscosity of the fermentation medium. The effects of these particles were modelled using the Ostwald-de Waele formulation which proved sufficient with an average error of 11.1 % between experimental average and numerical predicted apparent dynamic viscosities.

When particle concentrations dropped below 20 g/L, the effects thereof in the mixture become negligible and the effects of ethanol and glycerol become more prominent. These effects were modelled using the models proposed by Moreira *et al.* (2009). The second objective for this study was therefore completed and in preparation for publication.

7.1.3 Numerical simulations

The third objective was to model a 1.3 L stirred tank reactor using CFD to evaluate the applicability of this technology to modelling biological systems, with the focus on the effect of the particle transport and distribution on the kinetic reaction models and vice-versa. This included the development of new models and parameter estimation for such simulations.

CFD is a vital tool when designing large mixing vessels for industrial use. CFD was used in this work to evaluate the flow and pressure fields developed within a 1.3 L fermenter vessel. Two momentum equations were solved simultaneously to model the continuous and discrete particle phases. Interaction between these phases where accounted for with a set of drag and turbulence closure equations discussed in Chapter 5.

Particle properties were incorporated into these models, including a solids pressure force equation developed in this study, to improve the stability over previous models for use with low packing factor particles. Furthermore, it was observed that the settling rate of the particles decreased as the concentration of particles increased. This is due to particle hindrance which was accounted for by the Syamlal and O'Brein (1988) model.

Biological reactions were modelled on a per cell basis using user-code written in the C programming language. Particle distribution information was exported from the CFD simulations and imported into the user code, where a set of

reactions was modelled on each cell. After reaction rates and constituent concentrations were calculated in each cell, the solutes were averaged globally throughout the continuous phase, except for the case of fully settled particles. This captured the homogeneous nature of the solutes within the reactor. For increased accuracy the reaction kinetic user code could be run for a predetermined number of time-steps and the new fluid and particle properties fed back to the CFD simulations to recalculated a new particle distribution. This procedure could be repeated at smaller time intervals to increase the accuracy of the predictions.

Results form Chapter 6 indicated that the hydrolysis of the cellulose particles decreased the average particle size. These smaller particles are easier to transport through the fermenter, leading to an increase in particle suspension and therefore fermenter homogeneity.

Decreasing the agitation rate within the fermenter and allowing the particles to partially or fully settled, significantly reduced the hydrolysis and fermentation rates. This is due to decreased enzyme availability and in the case of fully settled particles, trapped products between the particles which caused significant product inhibition. The third and final objective of the project was hereby successfully completed and in preparation for publication.

7.2 Project Limitations and Restrictions

7.2.1 Kinetic models

The objective of the kinetic models were to collect as much information on the conversion rate of cellulose to ethanol, glycerol and yeast cells as possible. This information was further augmented with the adsorption dynamics of the enzymes to the cellulose particle surfaces under real simultaneous saccharification and fermentation conditions. A typical experiment required approximately a week to prepare cultures, clean the reactors, sterilise all fermentation medium and filter sterilise enzyme preparations and essential vitamins before inoculation. Glucose fermentations lasted only 2 days, with the samples analysed and processed within the following 2 weeks. Cellulose conversion experiments last a week, requiring a further 2-3 weeks for sample analysis and enzyme assays and data processing.

7.2.2 Mixing models

Particle properties proved challenging to investigate, due to the irregularity of the particle shapes and sizes. In Chapter 4, it was mentioned that the particles were found to have the highest contribution to the apparent dynamic viscosity of the bulk fluid. These measurements were conducted using an Anton Paar rheology machine situated at the Process Engineering department. The measuring head and chamber for this device are stainless steel and are embedded within a temperature controlled housing. This unfortunately made visual observations to confirm particle distribution within the measuring cylinder impossible.

However, from the torque measured and viscosity versus shear-rate graphs, it was determined that initialising the shear-rate measurements at low shear-rates allowed the particles to settle, causing unrealistically high viscosities and unusual viscosity versus shear-rate relationships. It was further observed that during high shear-rates, these extreme viscosities would plummet down to a viscosity much closer to that of the base medium, suggesting that at a critical rotational rate of the measuring cylinder, the particles are fully suspended. It was thus decided to perform all viscosity measurements, starting at the high shear-rate and slowly retard the measuring cylinder to measure the lower shear-rates. This minimised the error and ensured a fully suspended particle distribution for the majority of the higher shear-rates.

Modelling methods for viscosity was limited by the compatibility required for the CFD models, which determines the cell viscosity based on a volume fraction weighting between the phases. A further restriction posed by CFD is that the models should remain continuous within the range of operation. Although curve-fits could be accurately obtained for each particle concentration, finding a simple equation to predict all concentrations proved challenging. It was decided to remain with the best known power-law equation. The errors generated were considered non-critical as the turbulence viscosity generated by the k-ε turbulence model overshadowed the molecular viscosity 100 fold in most of the domain. Thus the viscosity model only really operated in regions of laminar flow.

7.2.3 Numerical simulations

STAR-CCM+ is a new integrated software package for CFD which combines the computer aided design (CAD), mesh generator, numerical solver and post-processing tools all-in-one. However, during the course of the project it became apparent that this software was still under-development with regard to the Eulerian multiphase models and many of the options required for the project was only made available early March 2011. This limited the time available for debugging of simulations and physics. However, the remaining time allowed for the development and evaluation of critical models which indicated where the weaknesses of CFD remain and can be improved.

Furthermore, as multiphase Eulerian simulations are a relatively new field in terms of particle-fluid interactions, some physical phenomena have not fully been developed to account for irregular shaped particles.

Time-scale differences between mixing and reactions rates are in the order of 1000 fold and solving these two phenomena simultaneously is not feasible on conventional personal computers (PC) or high performance computers (HPC), nor is it necessary. Furthermore, the commercial CFD does not allow other models to operate once the momentum equations have been frozen under multiphase conditions. Currently, the only method of separating the reaction kinetics from the mixing simulations, but still allow an exchange of information, is through external user coding as implemented in this study.

7.3 Conclusions

This study investigated the applicability of CFD to simulate particulate-biological processes using the Eulerian-Eulerian multiphase approach. During the course of the research various new contributions were made to the field of biological process engineering.

Chapter 3 discussed the experimental research and results from simultaneous saccharification and fermentation of microcrystalline cellulose. From the enzyme dynamics recorded, it was observed that the traditional method of assuming Langmuir adsorption was insufficient for capturing the adsorbed enzymes to the substrate. It was therefore proposed to separate the enzyme kinetics of exoglucanase and endoglucanase and allow for adsorption site competition. This model further assumed that the enzyme activity remained constant once attached to the cellulose chain. This approach was capable of predicting similar enzyme adsorption trends as was observed experimentally. This site competition and constant enzyme activity presenting an alternative theory to enzyme inactivation, and was in agreement with decreased substrate reactivity with respects to reduced surface area, as a result of decreased adsorption site availability.

Chapter 4 investigated the properties of the microcrystalline cellulose in terms of averaged density, particle size and drag characteristics. Results indicated an average particle density of 1605.7 kg/m^3 which agreed with values previously recorded in literature. The average effective particle size and drag characteristics were determined from a particle settling test using Stokes law. It was found that the particles behaved similar to a spherical particle which had an average diameter 3 times that of the mean particle diameter indicated by the suppliers. Literature indicated studies which investigated the effects of structure water on cellulose and boundary effects around all solid surfaces. The scale of these effects are similar in scale to the size of the particles, suggesting that the increased effective drag may be a result of these phenomena. Free settled packing of the particles were measured using a predetermined volume of particles and mixing with water in measuring cylinder and allowed to settle. A packing density of 0.21 was measured. This value is approximately 3 times lower than the random packing factor for spheres of similar size as the particles. This phenomenon, coupled with the increased drag, provided strong evidence of a micro-scale compact water boundary surrounding the particles. It was observed that boiling the settled particles increased the packing factor to near the theoretical value of approximately 0.67, indicating that the compact water boundary layer was removed.

Chapter 4 further investigated the effects of the fermentation constituents on the apparent dynamic viscosity of the fermentation medium. Results indicated that the particles had the greatest effect with all other constituents negligible in comparison. A viscosity model was developed based on the Ostwald-de Waele formulation weighted by the volume fraction of the solids. This maintained consistency with the formulation of the commercial CFD code used. This model

is to this authors' knowledge the first such model applied to microcrystalline cellulose for the purpose of CFD.

Chapter 5 investigated and validated a set of numerical models for application in CFD. Results indicated that traditional solid pressure models were developed for packing factors exceeding 0.6 and were unsuitable and highly unstable for packing factors 0.4 and below. An alternative formulation was proposed in this work which increased the stability of these models at lower packing factors. This model was later found to remain stable at nearly all packing factors and depending on the flow conditions, refrain from excessive overrun as was found with the previous model.

Rheology validations were found to be in reasonable agreement with experimental results, but, particle settling proved troubling. This excessive settling was not found during the rheological experiments. However, the error was determined to be the lack of a particle interaction model for the Eulerian-Eulerian simulations. It was considered beyond the scope of this project to research and develop particle interaction models to correct this problem. In the case of the fermentation vessel used in this study, it was found that the turbulence viscosity effects increased the drag influences on the particles, which resulted in the particle interactions not being necessary.

Chapter 6 presented the interaction of particle distribution and biological reaction. Conversion of the cellulose particles reduced the average particle size, causing the effects of drag to allow the particles to be suspended more consistently throughout the fermentation vessel. The cellulose particle distribution within the reactor was found to affect the reaction rate of the fermentation processes. For fully off-bottom suspensions, the reaction rates appeared near identical to the theoretically perfect homogeneous case. This indicated that perfect mixing is not a requirement for optimal biological reactions to occur. However, a second case was evaluated where the agitation rate was insufficient to maintain full off-bottom suspension and settling occurred. The reaction rates for this case indicated a significant decrease in the average attached enzymes, which resulted in lower conversion and ethanol production rates. The final case where all particles remained fully settled, resulted in a highly inefficient fermentation system as products remain trapped between the packed particles thus causing significant product inhibition.

From the above two cases it could be deduced that fermenters should be designed to operate at full off-bottom suspension, with a preferable agitation control system which could reduce the agitation rate as the conversion process progresses. This minimises the impeller speed and reduces the power in the order of $P_o \propto N^3$, where P_o is power and N the rotational speed of the impeller. Further investigations of the power requirements indicated that efficient fermenter designs require tall, slender reactors with preferably multiple impellers. This reduces the power requirement $P_o \propto D_i^5$, with D_i the impeller diameter.

8 FUTURE WORK

In Chapter 3 a kinetic reaction model was developed for the simultaneous saccharification and fermentation of microcrystalline cellulose for use in conjunction with CFD. This model requires modification of its coefficients for application to other cellulosic substrates, including bagasse and paper sludge, along with the use of alternative enzymes and fermenting microbe combinations. Future investigations will include these alternative substrates with the goal of developing a unified model for applications to most cellulosic substrates.

In Chapter 4, the cellulose particle properties were investigated to determine parameters such as effective Stokes diameters and density. Furthermore, a viscosity model was developed to approximate the apparent dynamic viscosity within the fermenters for use in CFD simulations. Validations of these models and properties in Chapter 5 indicated that the CFD results deviated significantly from the experimental measurements during the rheology replication simulations. This deviation was due to the excessive settling of the particles in the numerical simulations, which did not occur in reality. A possible cause for this deviation is the lack of a particle interaction model during the simulations. It was beyond the scope of this project to investigate this phenomenon further. However, for future work it is recommended that a thorough review of existing particle interaction models be conducted to select and include the most appropriate set of equations to capture these interactions.

Validations of particle suspension height in Chapter 5 indicated that the CFD was under-predicting the total suspension height of the particles compared to experimental measurements. The reason for this deviation was the average particle size methodology used in this study. In reality, particle sizes vary greatly, leading to smaller particles being suspended higher and larger particles settling sooner. To overcome this problem two more phases are required in the numerical simulations. These include an effective particle size for the smaller and larger particles. This will ensure more accurate predictions. However, such simulations will require significantly more computational resources.

During scale-up investigations the effects of high shear-rates on the fermenting microbes will become more significant. Additional investigation to determine the effects of high shear-rates on these microbes are required and necessary to establish the constraints of a cellulose to ethanol fermentation process.

Power consumption and the performance of a fermenter is important for industrial success. These parameters can now be effectively evaluated using the tools developed in this study. Thus future work will include the investigation of various fermenter designs in terms of power requirement and performance, as well as the effects of each on the reaction rate and biological ecosystems.

During the course of this study, only cellulose was considered. Lignocellulose,

however, further consists of lignin, hemicellulose and other organic substances which may influence the performance of the hydrolysis process. These effects require further investigation to determine the minimum pre-treatment requirements for efficient and effective conversion.

APPENDIX A: MATLAB CODE FOR KINETIC MODEL

```
%--------------------------------------------------------------------------%
%                 Clearing all plots graphs and errors                     %
%--------------------------------------------------------------------------%

close all;
clear all;
clc;

%--------------------------------------------------------------------------%
%                        Defining the variables                            %
%--------------------------------------------------------------------------%


sig_C=0.084;                    % g/g   Maximum enzyme Capacity
sig_C1=0.084;                   % g/g   Maximum enzyme Capacity

Funct1=-0.11;                   % g/L.h Maximum Endoglucanase activity
Funct2=-0.07;                   % g/L.h Maximum Exoglucanse activity
dt=0.0005;                      % h     Time step
tau=8;                          % h     Delay time for exoglucanase

k_Cb=640;                       % 1/h
k_G=0.476;                      % g/L

K_c=1.84;                       % L/g
K_c1=55;                        % L/g

K_m=10.56;                      % g/L

k_CbG=0.62;                     % g/L
k_CCb=5.85;                     % g/L
k_CEt=50.35;                    % g/L
k_XEt=50;                       % g/L

k_fc=1.8366;                    % L/g.h
k_rc=k_fc/K_c;                  % 1/h
k_rc1=k_fc/K_c1;                % 1/h

mu_max=0.4;                     % 1/h

Vt=0.8;                         % L

Y_XG=0.12;                      % g/g
Y_EtG=0.4048;                   % g/g
Y_GLG=0.09;                     % g/g
Y_CO2G=0.3872;                  % g/g
Y_OG=0;                                         % g/g

%--------------------------------------------------------------------------%
%                          Predefining  Arrays                             %
%--------------------------------------------------------------------------%

itermax=120/dt;

EC=zeros(itermax+1,1);          % g
EA=zeros(itermax+1,1);          % g
CC=zeros(itermax+1,1);          % g
CA=zeros(itermax+1,1);          % g
C=zeros(itermax+1,1);           % g
Cb=zeros(itermax+1,1);          % g
G=zeros(itermax+1,1);           % g
B=zeros(itermax+1,1);           % g
X=zeros(itermax+1,1);           % g
Et=zeros(itermax+1,1);          % g
V=zeros(itermax+1,1);           % m^3
O=zeros(itermax+1,1);           % g
```

```
CO2=zeros(itermax+1,1);          % g
GL=zeros(itermax+1,1);           % g
H2O=zeros(itermax+1,1);          % g


r_ec=zeros(itermax+1,1);         % g/h
r_ea=zeros(itermax+1,1);         % g/h
r_ca=zeros(itermax+1,1);         % g/h
r_x=zeros(itermax+1,1);          % g/h
r_cb=zeros(itermax+1,1);         % g/h
r_g=zeros(itermax+1,1);          % g/h
r_et=zeros(itermax+1,1);         % g/h
r_co2=zeros(itermax+1,1);        % g/h
r_gl=zeros(itermax+1,1);         % g/h
r_o=zeros(itermax+1,1);          % g/h
r_c=zeros(itermax+1,1);          % g/h

C_ecf=zeros(itermax+1,1);        % g/L
C_eaf=zeros(itermax+1,1);        % g/L
C_ccf=zeros(itermax+1,1);        % g/L
C_caf=zeros(itermax+1,1);        % g/L
C_ca=zeros(itermax+1,1);         % g/L
C_cc=zeros(itermax+1,1);         % g/L
C_ec=zeros(itermax+1,1);         % g/L
C_ea=zeros(itermax+1,1);         % g/L
C_exo=zeros(itermax+1,1);        % g/L
C_endo=zeros(itermax+1,1);       % g/L

x=zeros(itermax+1,1);            % # Conversion fraction
t=zeros(itermax+1,1);            % h

%--------------------------------------------------------------------------%
%                            Initial Conditions                            %
%--------------------------------------------------------------------------%

C_c_in=92;                       % g/L cellulose
FPU=10;                          % FPU cellulase
CBU=50;                          % IU Beta-glucosidase

ii=1;                            % Initial iterator

CA(ii)=(45/100*C_c_in)*Vt;       % Crystalline Substrate
CC(ii)=C_c_in*Vt-CA(ii);         % Amorphous Substrate

C(ii)=CA(ii)+CC(ii);             % Total cellulase

%--------------------------------------------------------------------------%
%                             Simulation Runs                              %
%--------------------------------------------------------------------------%

for ii=1:itermax

    V(ii)=Vt-C(ii)/1600;                                        % L
    B(ii)=148.06/586.2*CBU*C_c_in*Vt/V(ii)/1000;                % g
    C_Exo_max=195.4/64.5*FPU*C_c_in*Vt/V(ii)*0.8/1000;          % g/L
    C_Endo_max=195.4/64.5*FPU*C_c_in*Vt/V(ii)*0.12/1000;        % g/L
    C_exo(ii)=C_Exo_max;                                        % g/L
    C_endo(ii)=C_Endo_max;                                      % g/L

    C_Beta_max=148.06/586.2*CBU*C_c_in*Vt/V(ii)/1000;           % g/L
    t(ii+1)=(ii)*dt;                                            % h
    X(1)=0.03*V(1);                                             % g

    Err=1;

    while Err >=0.00000001

        Err2=1;

        while Err2 >=0.00000001
```

```
C1=C(ii+1)^2+Cb(ii+1)^2+G(ii+1)^2
    +Et(ii+1)^2+CO2(ii+1)^2+X(ii+1)^2+H2O(ii+1)^2
    +(EC(ii+1)/(1+sig_C))^2;                              % g

E1=(EC(ii+1)*V(ii)*sig_C/(1+sig_C))^2
    +(EA(ii+1)*V(ii)*sig_C1/(1+sig_C1))^2;                % g

%*********************************%
%      Reactor Concentrations     %
%*********************************%


C_c=C(ii)/Vt;                                 % g/L Cellulose
C_cb=Cb(ii)/V(ii);                            % g/L Cellubiose
C_g=G(ii)/V(ii);                              % g/L Glucose
C_x=X(ii)/V(ii);                              % g/L Yeast Cells
C_et=Et(ii)/V(ii);                            % g/L Ethanol
C_b=B(ii)/V(ii);                              % g/L Beta-glucosidase
C_cc=CC(ii)/Vt;                               % g/L Amorphous cellulose
C_ca=CA(ii)/Vt;                               % g/L Crystalline cellulose
C_ec=EC(ii)/V(ii);                            % g/L Exoglucanase
C_ea=EA(ii)/V(ii);                            % g/L Endoglucanase

C_ecf=C_Endo_max-C_ec*sig_C/(1+sig_C);        % g/L
C_eaf=C_Exo_max-C_ea*sig_C1/(1+sig_C1);       % g/L
C_ccf=C_cc-C_ec/(1+sig_C);                    % g/L
C_caf=C_ca-C_ea/(1+sig_C1);                   % g/L

%*********************************%
%         Reaction Rates          %
%*********************************%

r_ec(ii)= r_ca(ii)*(1+sig_C)
          +(k_fc*C_ecf*(1+sig_C)*C_ccf-k_rc*C_ec);            % g/L.h

r_ca(ii)=Funct1*C_ec/(1+sig_C)
          *(k_CCb/(C_cb+k_CCb))*(k_CEt/  (C_et+k_CEt));       % g/L.h

r_ea(ii)= r_c(ii)*(1+sig_C1)
          +(k_fc*C_eaf*(1+sig_C1)*C_caf-k_rc1*C_ea);          % g/L.h

r_c(ii)=tanh(t(ii)/tau)*Funct2*C_ea/(1+sig_C1)
          *(k_CCb/(C_cb+k_CCb))*(k_CEt/(C_et+k_CEt));         % g/L.h

r_cb(ii)=-342/324*r_c(ii)
          -(k_Cb*C_cb*C_b/(K_m*(1+C_g/k_CbG)+C_cb));          % g/L.h

r_x(ii)=((C_x*mu_max*C_g)/(C_g+k_G))*(1-C_et/k_XEt);          % g/L.h
r_g(ii)=(-342/324*r_c(ii)-r_cb(ii))*360/342-r_x(ii)/Y_XG;     % g/L.h
r_et(ii)=r_x(ii)*Y_EtG/Y_XG;                                  % g/L.h
r_co2(ii)=r_x(ii)*Y_CO2G/Y_XG;                                % g/L.h
r_gl(ii)=r_x(ii)*Y_GLG/Y_XG;                                  % g/L.h

%*********************************%
%         Reactor Content         %
%*********************************%

EC(ii+1)=EC(ii)+r_ec(ii)*V(ii)*dt;
EA(ii+1)=EA(ii)+r_ea(ii)*V(ii)*dt;
CC(ii+1)=CC(ii)+r_ca(ii)*Vt*dt;
CA(ii+1)=CA(ii)+(r_c(ii)-r_ca(ii))*Vt*dt;

C(ii+1)=CC(ii)+CA(ii);                                        % g
B(ii+1)=B(ii);                                                % U
Cb(ii+1)=Cb(ii)+(r_cb(ii)*V(ii))*dt;                          % g
G(ii+1)=G(ii)+(r_g(ii)*V(ii))*dt;                             % g
X(ii+1)=X(ii)+(r_x(ii)*V(ii))*dt;                             % g
Et(ii+1)=Et(ii)+(r_et(ii)*V(ii))*dt;                          % g
CO2(ii+1)=CO2(ii)+(r_co2(ii)*V(ii))*dt;                       % g
GL(ii+1)=GL(ii)+(r_gl(ii)*V(ii))*dt;                          % g
H2O(ii+1)=H2O(ii)+18*r_c(ii)/162*V(ii)*dt;                    % g
```

```
            V(ii+1)=Vt-C(ii)/1600;

            %*********************************%
            %            Conversion           %
            %*********************************%

            x(ii+1)=(C_c_in*Vt-C(ii+1))/(C_c_in*Vt);

            %*********************************%
            %          Error Checks           %
            %*********************************%


            Err2=sqrt((EC(ii+1)*V(ii)*sig_C/(1+sig_C))^2
                  +(EA(ii+1)*V(ii)*sig_C1/(1+sig_C1))^2-E1);

         end
         Err=sqrt(C(ii+1)^2+Cb(ii+1)^2+G(ii+1)^2+Et(ii+1)^2
                  +CO2(ii+1)^2+X(ii+1)^2+H2O(ii+1)^2+(EC(ii+1)/(1+sig_C))^2-C1);
    end

end
```

APPENDIX B: RAW DATA

Table B-1a: HPLC results from the glucose fermentation

Time [h]	Glucose [g/L]		Glycerol [g/L]		Ethanol [g/L]		Biomass [g/L]	
	Run 1	Run 2	Run 1	Run 2	Run 1	Run 2	Run 1	Run 2
0	40.00	42.99	0.00	0.00	0.00	0.00	0.06	0.04
2	35.20	36.68	0.00	0.00	0.00	0.00	0.08	0.06
4	36.67	38.83	0.00	0.00	0.37	0.05	0.14	0.12
6	36.05	37.42	0.00	0.00	0.62	0.70	0.25	0.25
8	30.55	29.80	1.07	1.08	1.84	1.43	0.78	0.78
10	26.65	21.76	1.80	1.67	4.27	3.59	1.46	1.54
12	12.99	11.31	2.44	2.87	7.22	8.71	2.60	2.73
14	0.71	0.00	3.71	4.03	13.18	13.83	3.85	3.81
16	0.00	0.00	3.59	4.07	12.51	14.08	4.91	4.84
18	0.00	0.00	3.74	3.29	13.52	10.66	4.87	5.32
24	0.00	0.00	3.70	3.94	13.02	13.86	3.82	4.13

Table B-1b: HPLC results from the glucose fermentation

Time [h]	Glucose [g/L]		Glycerol [g/L]		Ethanol [g/L]		Biomass [g/L]	
	Run 3	Run 4	Run 3	Run 4	Run 3	Run 4	Run 3	Run 4
0	37.93	39.83	0.00	0.00	0.00	0.00	0.01	0.01
3	37.48	39.54	0.00	0.00	0.11	0.14	0.05	0.05
5	36.91	38.55	0.00	0.00	0.39	0.44	0.15	0.15
7	34.50	36.23	0.00	0.00	1.08	1.20	0.37	0.39
9	30.07	31.47	0.87	0.98	2.60	2.90	0.83	0.91
11	22.82	23.09	1.75	2.03	5.61	6.18	1.62	1.72
13	8.21	8.10	3.12	3.47	10.97	11.95	3.26	3.42
15	0.00	0.00	3.84	4.25	14.34	15.58	4.93	5.29
19	0.00	0.00	3.88	3.66	14.39	13.08	5.00	5.02
29	0.00	0.00	3.84	3.84	14.25	14.49	5.17	4.76
38	0.00	0.00	3.84	4.17	14.22	15.01	4.93	5.02

Table B-2a: HPLC results from the Avicel hydrolysis and fermentation

Time [h]	Glucose [g/L]				Glycerol [g/L]				Ethanol [g/L]			
	Run 1	Run 2	Run 3	Run 4	Run 1	Run 2	Run 3	Run 4	Run 1	Run 2	Run 3	Run 4
0	1.004	0.998	0.624	0.592	0.000	0.000	0.000	0.000	0.000	0.000	0.000	0.000
4	3.195	3.335	2.502	2.849	0.000	0.000	0.000	0.000	0.206	0.26	0.01	0.24
8	0.968	1.329	1.160	1.271	0.566	0.468	0.505	0.513	2.47	2.07	2.21	2.15
12	0.330	0.325	0.270	0.000	1.256	1.157	1.208	1.280	5.21	4.95	4.75	5.43
16	1.070	1.049	0.703	0.669	1.650	1.689	1.670	1.794	7.39	7.79	6.70	7.75
28	1.026	1.005	1.051	1.062	2.708	2.609	2.652	2.882	13.29	12.87	12.15	13.64
40	1.006	0.967	0.992	1.035	3.300	5.864	3.330	3.598	17.60	17.24	16.16	17.99
52	0.996	0.939	0.992	1.024	3.626	3.391	3.625	3.909	20.76	18.71	19.11	20.83
64	0.956	0.986	1.004	1.064	3.780	3.767	3.804	4.103	23.57	23.19	21.46	23.92
76	0.982	0.975	1.148	1.038	4.045	3.736	3.980	4.232	25.73	25.57	23.43	25.43
88	0.963	0.948	1.225	1.130	4.072	3.712	4.020	4.301	27.50	26.06	25.10	27.19
100	0.949	0.955	1.117	0.983	4.025	3.796	4.129	4.365	28.98	28.10	26.18	28.67
112	0.955	0.940	0.979	0.987	4.076	3.920	4.240	4.417	30.51	30.11	29.31	29.55

Table B-2b: HPLC results from the Avicel hydrolysis and fermentation

Time [h]	Biomass [g/L]				Avicel [g/L]			
	Run 1	Run 2	Run 3	Run 4	Run 1*	Run 2*	Run 3	Run 4
0	0.02	0.02	0.02	0.03	-	-	94.30	89.14
4	0.19	0.13	0.18	0.14	-	-	89.76	90.26
8	0.91	1.00	1.56	1.01	-	-	87.36	87.03
12	2.00	2.84	3.18	2.46	-	-	79.22	78.64
16	2.59	3.78	4.36	3.89	-	-	74.16	72.92
28	4.23	5.41	6.76	6.53	-	-	60.92	60.19
40	5.87	6.92	9.15	7.79	-	-	50.42	48.68
52	5.00	6.41	8.53	6.10	-	-	45.67	43.38
64	4.89	6.07	10.25	6.97	-	-	39.11	38.98
76	5.05	7.40	11.07	7.33	-	-	34.94	32.35
88	5.10	6.56	9.66	12.02	-	-	31.97	30.01
100	4.89	7.05	8.02	7.38	-	-	28.51	26.49
112	5.53	5.79	7.20	4.89	-	-	26.47	25.51

**Only two Avicel pellet sets were collected as the previous two sets were accidentally removed from storage before sampling*

Table B-3: Avicel adsorption of endoglucanase and exoglucanase enzymes

Time	Endoglucanase				Exoglucanase			
	Run 1	Run 2	Run 3	Run 4	Run 1	Run 2	Run 3	Run 4
0	0.262	0.252	0.282	0.259	2.226	2.228	2.105	1.974
4	0.258	0.248	0.268	0.267	2.241	2.290	2.295	2.278
8	0.254	0.253	0.266	0.265	2.179	2.227	2.214	2.196
12	0.258	0.256	0.259	0.264	2.119	2.217	2.167	2.228
16	0.260	0.253	0.266	0.264	1.952	2.051	1.994	2.040
28	0.256	0.256	0.264	0.266	1.063	1.305	1.233	0.897
40	0.254	0.238	0.260	0.252	0.744	1.031	0.703	0.639
52	0.253	0.237	0.259	0.253	0.711	0.967	0.578	0.395
64	0.258	0.237	0.260	0.251	0.762	1.044	0.932	0.504
76	0.252	0.237	0.251	0.251	0.754	1.139	0.951	0.604
88	0.254	0.242	0.253	0.250	0.913	1.069	0.955	0.596
100	0.241	0.253	0.250	0.253	0.856	1.069	0.918	0.576
112	0.225	0.243	0.257	0.260	0.758	1.049	0.677	0.376

Table B-4a: Dynamic viscosity at various Avicel particle concentrations

Shear Rate [s^{-1}]	Dynamic Viscosity [$x10^{-3}$ kg/m.s]											
	100 g/L					80 g/L			60 g/L			
	Run 1	Run 2	Run 3	Run 4	Run 5	Run 1	Run 2	Run 3	Run 1	Run 2	Run 3	Run 4
350	2.16	1.92	2.15	2.02	2.47	1.93	2.06	2.10	2.46	2.03	2.05	1.90
338	2.17	1.94	2.17	2.04	2.47	1.95	2.07	2.10	2.42	2.01	2.04	1.90
326	2.20	1.97	2.21	2.07	2.51	1.99	2.11	2.14	2.45	2.03	2.07	1.93
314	2.24	2.00	2.27	2.12	2.56	2.04	2.18	2.21	2.50	2.08	2.12	1.98
302	2.28	2.04	2.32	2.16	2.61	2.11	2.25	2.28	2.56	2.12	2.17	2.04
290	2.32	2.08	2.37	2.22	2.66	2.18	2.33	2.36	2.62	2.18	2.22	2.09
278	2.39	2.13	2.44	2.28	2.74	2.27	2.43	2.46	2.70	2.24	2.30	2.16
266	2.44	2.18	2.49	2.35	2.82	2.37	2.54	2.57	2.77	2.31	2.37	2.23
253	2.51	2.24	2.56	2.43	2.92	2.48	2.68	2.70	2.86	2.39	2.46	2.32
241	2.57	2.30	2.62	2.51	3.02	2.62	2.82	2.85	2.94	2.47	2.55	2.40
229	2.65	2.37	2.67	2.61	3.15	2.77	2.99	3.01	3.04	2.57	2.65	2.49
217	2.72	2.45	2.77	2.72	3.29	2.94	3.17	3.19	3.14	2.66	2.75	2.58
205	2.82	2.55	2.84	2.86	3.45	3.13	3.36	3.38	3.26	2.78	2.87	2.69
193	2.94	2.67	2.94	3.01	3.62	3.34	3.56	3.58	3.37	2.89	2.98	2.79
181	3.07	2.82	3.05	3.20	3.82	3.55	3.77	3.80	3.5	3.02	3.11	2.91
169	3.22	3.01	3.20	3.43	4.02	3.78	4.00	4.04	3.66	3.16	3.26	3.04
157	3.42	3.23	3.40	3.68	4.26	4.00	4.24	4.28	3.81	3.30	3.40	3.18
145	3.64	3.47	3.66	3.97	4.55	4.26	4.49	4.55	3.99	3.46	3.57	3.33
133	3.88	3.75	3.96	4.29	4.95	4.55	4.77	4.83	4.19	3.64	3.76	3.50
121	4.18	4.06	4.30	4.64	5.40	4.85	5.07	5.15	4.42	3.85	3.97	3.69
109	4.53	4.41	4.69	5.04	5.94	5.19	5.40	5.51	4.68	4.07	4.22	3.91
96.6	4.95	4.84	5.16	5.51	6.54	5.61	5.82	5.92	5.00	4.35	4.49	4.17
84.5	5.41	5.30	5.67	6.02	7.22	6.08	6.26	6.40	5.37	4.69	4.85	4.47
72.4	5.95	5.84	6.32	6.68	8.05	6.66	6.81	6.98	5.85	5.07	5.26	4.87
60.3	6.60	6.54	7.08	7.44	9.00	7.39	7.56	7.70	6.46	5.62	5.82	5.32
48.3	7.49	7.39	8.03	8.47	10.40	8.40	8.41	8.59	7.22	6.25	6.53	5.95
36.2	8.70	8.52	9.30	9.90	12.09	9.42	9.61	9.72	8.22	7.08	7.45	6.80
24.1	10.60	10.47	11.56	12.02	14.65	11.38	11.34	11.55	10.25	8.87	8.96	8.07
12.1	14.48	14.15	16.48	16.62	20.44	15.00	14.71	15.13	13.83	11.74	11.97	10.54

Table B-4b: Dynamic viscosity at various Avicel particle concentrations

Shear Rate [s^{-1}]	Dynamic Viscosity [$x10^{-3}$ kg/m.s]											
	40 g/L				30 g/L			25 g/L			20 g/L	
	Run 1	Run 2	Run 3	Run 4	Run 1	Run 2	Run 3	Run 1	Run 2	Run 3	Run 1	Run 2
350	2.17	1.67	1.64	1.74	1.14	1.11	1.28	0.99	1.07	0.98	0.91	0.88
338	1.98	1.57	1.56	1.63	1.11	1.08	1.23	0.99	1.05	0.98	0.89	0.88
326	1.94	1.56	1.55	1.60	1.11	1.07	1.22	0.98	1.05	0.99	0.90	0.89
314	1.94	1.57	1.56	1.60	1.11	1.06	1.22	0.99	1.06	0.99	0.90	0.90
302	1.96	1.59	1.58	1.61	1.11	1.05	1.23	0.99	1.06	0.99	0.90	0.90
290	1.99	1.61	1.60	1.63	1.11	1.05	1.22	0.98	1.06	0.99	0.90	0.89
278	2.04	1.65	1.64	1.67	1.12	1.05	1.22	0.99	1.06	1.00	0.90	0.90
266	2.08	1.69	1.67	1.71	1.13	1.04	1.22	0.99	1.06	0.99	0.89	0.89
253	2.13	1.74	1.72	1.77	1.14	1.04	1.22	0.99	1.07	1.00	0.89	0.90
241	2.18	1.78	1.76	1.85	1.15	1.03	1.22	0.99	1.07	1.00	0.89	0.89
229	2.23	1.83	1.82	1.94	1.16	1.03	1.22	0.99	1.08	1.00	0.89	0.89
217	2.29	1.88	1.87	2.04	1.17	1.03	1.23	0.99	1.08	1.00	0.88	0.89
205	2.36	1.94	1.93	2.15	1.19	1.03	1.24	1.00	1.09	1.00	0.89	0.89
193	2.44	2.00	1.99	2.26	1.20	1.02	1.25	0.99	1.09	1.00	0.88	0.88
181	2.52	2.06	2.05	2.37	1.23	1.03	1.26	1.00	1.10	1.00	0.88	0.88
169	2.61	2.14	2.12	2.49	1.26	1.04	1.28	1.01	1.12	1.02	0.88	0.89
157	2.71	2.21	2.20	2.61	1.30	1.03	1.30	1.01	1.13	1.02	0.88	0.88
145	2.82	2.28	2.28	2.74	1.34	1.05	1.33	1.02	1.15	1.03	0.87	0.88
133	2.94	2.37	2.37	2.89	1.38	1.06	1.36	1.02	1.17	1.03	0.87	0.88
121	3.08	2.56	2.48	3.05	1.43	1.07	1.40	1.04	1.21	1.06	0.87	0.88
109	3.25	2.64	2.59	3.22	1.48	1.09	1.48	1.06	1.27	1.08	0.87	0.88
96.6	3.47	2.74	2.73	3.44	1.53	1.14	1.47	1.08	1.33	1.08	0.86	0.87
84.5	3.71	2.87	2.89	3.69	1.60	1.19	1.57	1.12	1.41	1.13	0.87	0.87
72.4	4.02	3.06	3.09	4.01	1.67	1.23	1.64	1.16	1.44	1.16	0.87	0.88
60.3	4.40	3.29	3.37	4.41	1.77	1.30	1.74	1.21	1.44	1.22	0.88	0.89
48.3	4.91	3.64	3.70	4.91	1.86	1.40	1.94	1.26	1.53	1.29	0.89	0.92
36.2	5.65	4.25	4.18	5.57	2.02	1.39	2.23	1.33	2.06	1.46	0.92	0.95
24.1	6.86	5.08	5.15	6.90	2.35	1.58	2.88	1.42	2.91	1.56	0.92	0.98
12.1	9.38	6.93	6.96	8.67	3.00	2.09	4.21	1.79	4.38	2.61	1.06	1.23

Table B-5a: Torque from rheology study at various particle concentrations

Shear Rate [s^{-1}]	Torque [$x10^{-6}$ N·m]											
	100 g/L					80 g/L			60 g/L			
	Run 1	Run 2	Run 3	Run 4	Run 5	Run 1	Run 2	Run 3	Run 1	Run 2	Run 3	Run 4
350	69.1	61.5	68.9	64.7	79.1	61.7	66.1	67.1	64.9	65.6	60.7	78.7
338	67.1	59.9	67.1	63.1	76.4	60.1	63.8	64.9	62.1	62.9	58.6	74.8
326	65.5	58.6	66	61.8	74.7	59.2	62.9	63.9	60.6	61.6	57.6	73.1
314	64.2	57.4	65.1	60.8	73.4	58.7	62.5	63.4	59.6	60.8	57	71.9
302	62.9	56.2	63.9	59.7	71.9	58.2	62.1	62.9	58.5	59.8	56.2	70.6
290	61.6	55	62.9	58.7	70.6	57.8	61.7	62.6	57.6	58.9	55.5	69.4
278	60.6	54	61.9	58	69.5	57.6	61.8	62.6	56.9	58.4	55	68.4
266	59.3	52.8	60.4	57.1	68.4	57.4	61.8	62.4	56	57.6	54.3	67.2
253	58.1	51.9	59.4	56.3	67.6	57.6	62.1	62.6	55.3	57	53.7	66.2
241	56.8	50.8	57.8	55.5	66.7	57.8	62.3	62.8	54.6	56.3	53	65
229	55.5	49.8	56.1	54.8	66	58.2	62.8	63.2	53.8	55.5	52.2	63.8
217	54.1	48.8	55.1	54.1	65.4	58.5	63	63.3	52.9	54.7	51.3	62.4
205	52.9	47.9	53.3	53.6	64.8	58.8	63	63.5	52.1	53.8	50.4	61.1
193	51.9	47.2	51.9	53.2	63.9	58.9	62.9	63.3	51	52.7	49.3	59.5
181	50.8	46.7	50.5	53.1	63.2	58.8	62.5	63	49.9	51.5	48.2	58.1
169	49.8	46.5	49.5	53	62.1	58.4	61.8	62.5	48.8	50.3	47	56.5
157	49	46.3	48.9	52.9	61.2	57.4	60.8	61.4	47.4	48.8	45.6	54.7
145	48.2	46	48.5	52.6	60.3	56.5	59.5	60.2	45.9	47.3	44.1	52.9
133	47.1	45.5	48.1	52.1	60.1	55.2	57.9	58.6	44.2	45.7	42.5	50.9
121	46.1	44.8	47.4	51.2	59.7	53.5	56	56.9	42.5	43.8	40.7	48.8
109	45	43.8	46.6	50.1	59	51.6	53.6	54.7	40.4	41.9	38.8	46.5
96.6	43.7	42.8	45.5	48.7	57.8	49.6	51.4	52.3	38.4	39.7	36.8	44.2
84.5	41.8	41	43.8	46.6	55.8	47	48.4	49.4	36.3	37.5	34.5	41.5
72.4	39.4	38.7	41.8	44.3	53.3	44.1	45.1	46.2	33.6	34.9	32.3	38.8
60.3	36.4	36.1	39.1	41.1	49.7	40.8	41.7	42.5	31	32.1	29.4	35.7
48.3	33.1	32.6	35.4	37.4	45.9	37.1	37.1	38	27.6	28.9	26.3	31.9
36.2	28.8	28.2	30.8	32.8	40	31.2	31.8	32.2	23.4	24.7	22.5	27.2
24.1	23.4	23.1	25.5	26.5	32.4	25.1	25	25.5	19.6	19.8	17.8	22.6
12.1	16	15.6	18.2	18.4	22.6	16.6	16.2	16.7	13	13.2	11.6	15.3

Table B-5b: Torque from rheology study at various particle concentrations

Shear Rate [s^{-1}]	Torque [$x10^{-6}$ N·m]											
	40 g/L				30 g/L			25 g/L			20 g/L	
	Run 1	Run 2	Run 3	Run 4	Run 1	Run 2	Run 3	Run 1	Run 2	Run 3	Run 1	Run 2
350	69.4	53.4	52.5	55.6	36.4	35.7	40.9	31.8	34.1	31.5	29.3	28
338	61.1	48.4	48.2	50.3	34.4	33.4	38	30.5	32.6	30.4	27.6	27.2
326	57.7	46.4	46.2	47.8	33	31.8	36.4	29.4	31.4	29.4	26.7	26.5
314	55.8	45	44.8	46	31.8	30.4	35.1	28.4	30.4	28.5	25.9	25.7
302	54.2	43.8	43.5	44.5	30.6	29	33.8	27.2	29.2	27.4	24.8	24.7
290	52.8	42.7	42.4	43.2	29.4	27.7	32.3	26.1	28	26.2	23.7	23.7
278	51.7	42	41.6	42.4	28.5	26.6	31.1	25.1	27	25.3	22.9	22.8
266	50.4	41	40.6	41.6	27.3	25.2	29.6	24	25.8	24.1	21.7	21.7
253	49.3	40.3	39.8	41.1	26.4	24	28.2	22.9	24.8	23.1	20.7	20.8
241	48.1	39.3	39	40.8	25.3	22.8	26.9	21.8	23.7	22	19.6	19.7
229	46.9	38.5	38.2	40.7	24.3	21.6	25.7	20.8	22.6	20.9	18.6	18.7
217	45.6	37.4	37.2	40.5	23.2	20.4	24.4	19.7	21.5	19.9	17.6	17.7
205	44.3	36.5	36.3	40.4	22.3	19.4	23.2	18.7	20.5	18.9	16.6	16.7
193	43	35.3	35.1	39.8	21.3	18	22	17.6	19.3	17.7	15.5	15.6
181	41.7	34.1	34	39.3	20.4	17.1	20.9	16.5	18.3	16.6	14.5	14.6
169	40.3	33.1	32.8	38.5	19.6	16	19.8	15.6	17.3	15.7	13.6	13.7
157	38.9	31.7	31.5	37.5	18.6	14.8	18.7	14.5	16.2	14.6	12.6	12.7
145	37.4	30.2	30.2	36.3	17.8	13.9	17.6	13.5	15.2	13.6	11.6	11.7
133	35.7	28.8	28.8	35.1	16.8	12.8	16.6	12.4	14.2	12.5	10.6	10.6
121	34	28.3	27.4	33.7	15.8	11.8	15.4	11.5	13.3	11.7	9.61	9.69
109	32.3	26.2	25.7	32	14.7	10.8	14.7	10.5	12.6	10.7	8.62	8.7
96.6	30.6	24.2	24.1	30.4	13.5	10	13	9.51	11.7	9.58	7.63	7.68
84.5	28.7	22.2	22.3	28.5	12.4	9.19	12.1	8.64	10.9	8.73	6.72	6.75
72.4	26.6	20.3	20.5	26.5	11.1	8.13	10.9	7.66	9.52	7.72	5.77	5.85
60.3	24.3	18.1	18.6	24.3	9.78	7.18	9.61	6.69	7.94	6.75	4.84	4.94
48.3	21.7	16.1	16.3	21.7	8.23	6.18	8.56	5.56	6.75	5.71	3.95	4.07
36.2	18.7	14.1	13.9	18.4	6.67	4.6	7.38	4.39	6.84	4.83	3.03	3.16
24.1	15.2	11.2	11.4	15.2	5.18	3.48	6.35	3.14	6.43	3.44	2.03	2.17
12.1	10.4	7.65	7.68	9.58	3.32	2.31	4.65	1.98	4.83	2.88	1.17	1.36

Table B-6: Viscosity measurements for Tween 80

Shear Rate [s^{-1}]	Dynamic Viscosity [$x10^{-3}$ kg/m.s]					Shear Rate [s^{-1}]	Dynamic Viscosity [$x10^{-3}$ kg/m.s]				
	Control		Tween 80				Control		Tween 80		
	Run 1	Run 2	Run 1	Run 2	Run 3		Run 1	Run 2	Run 1	Run 2	Run 3
275	2.76	2.56	2.86	2.92	2.79	137	3.84	3.99	3.77	3.91	3.95
269	2.73	2.57	2.83	2.90	2.78	132	3.92	4.08	3.84	3.98	4.03
264	2.73	2.61	2.83	2.90	2.79	127	4.02	4.19	3.93	4.07	4.13
259	2.75	2.64	2.83	2.90	2.81	122	4.10	4.28	4.01	4.16	4.22
254	2.76	2.67	2.84	2.91	2.82	117	4.21	4.39	4.11	4.26	4.33
249	2.78	2.70	2.85	2.92	2.84	112	4.31	4.52	4.21	4.37	4.44
244	2.82	2.75	2.88	2.95	2.88	107	4.43	4.65	4.32	4.48	4.57
239	2.85	2.79	2.89	2.97	2.90	102	4.55	4.80	4.44	4.61	4.69
234	2.88	2.83	2.92	2.99	2.93	96.6	4.71	4.97	4.58	4.75	4.85
229	2.91	2.87	2.94	3.02	2.97	91.5	4.85	5.13	4.72	4.89	4.99
224	2.95	2.92	2.97	3.05	3.00	86.4	5.03	5.32	4.88	5.06	5.16
219	2.98	2.96	2.99	3.08	3.04	81.4	5.21	5.51	5.05	5.23	5.35
214	3.02	3.01	3.03	3.11	3.08	76.3	5.41	5.73	5.24	5.43	5.55
208	3.06	3.06	3.06	3.15	3.12	71.2	5.63	5.98	5.45	5.64	5.76
203	3.10	3.10	3.09	3.18	3.16	66.1	5.87	6.24	5.68	5.87	6.00
198	3.15	3.16	3.13	3.23	3.21	61	6.17	6.55	5.95	6.15	6.27
193	3.19	3.22	3.17	3.27	3.26	55.9	6.48	6.86	6.24	6.42	6.54
188	3.24	3.27	3.21	3.32	3.30	50.8	6.88	7.27	6.59	6.78	6.87
183	3.29	3.33	3.26	3.36	3.36	45.8	7.26	7.66	6.93	7.10	7.18
178	3.34	3.39	3.30	3.41	3.41	40.7	7.73	8.11	7.33	7.48	7.51
173	3.38	3.44	3.34	3.45	3.46	35.6	8.26	8.64	7.76	7.90	7.90
168	3.44	3.51	3.40	3.51	3.52	30.5	8.88	9.28	8.30	8.36	8.29
163	3.49	3.57	3.45	3.56	3.58	25.4	9.61	10.08	8.89	8.92	8.83
158	3.56	3.65	3.51	3.63	3.65	20.3	10.36	10.83	9.48	9.46	9.29
153	3.62	3.73	3.57	3.69	3.72	15.3	11.44	12.17	10.31	10.22	9.99
147	3.69	3.81	3.63	3.76	3.79	10.2	12.43	13.76	11.10	10.95	10.69
142	3.76	3.89	3.70	3.83	3.86	5.08	16.04	17.79	13.45	13.35	13.37

Table B-7: Dynamic viscosity of oligomer test

Shear Rate [s^{-1}]	Dynamic Viscosity [$x10^{-3}$ kg/m.s]					Shear Rate [s^{-1}]	Dynamic Viscosity [$x10^{-3}$ kg/m.s]		
	Oligomers						Control		
350	0.83	0.83	0.86	0.81	0.79	350	0.849	0.844	0.844
338	0.82	0.82	0.83	0.81	0.79	338	0.847	0.843	0.843
326	0.82	0.82	0.84	0.81	0.79	326	0.842	0.838	0.838
314	0.83	0.83	0.84	0.82	0.79	314	0.844	0.840	0.841
302	0.83	0.83	0.84	0.81	0.79	303	0.843	0.840	0.840
290	0.82	0.82	0.83	0.81	0.79	291	0.842	0.839	0.839
278	0.83	0.83	0.84	0.82	0.80	279	0.844	0.841	0.842
266	0.82	0.82	0.83	0.81	0.79	267	0.836	0.834	0.834
253	0.83	0.82	0.83	0.81	0.79	255	0.834	0.831	0.832
241	0.82	0.82	0.83	0.81	0.79	243	0.839	0.837	0.838
229	0.82	0.82	0.83	0.81	0.79	231	0.834	0.833	0.833
217	0.82	0.82	0.83	0.81	0.79	219	0.835	0.834	0.834
205	0.82	0.82	0.83	0.81	0.79	208	0.831	0.829	0.829
193	0.82	0.82	0.82	0.81	0.78	196	0.830	0.829	0.829
181	0.82	0.82	0.83	0.81	0.79	184	0.827	0.826	0.827
169	0.82	0.82	0.83	0.81	0.79	172	0.834	0.833	0.834
157	0.82	0.82	0.83	0.81	0.79	160	0.830	0.830	0.831
145	0.82	0.82	0.83	0.81	0.79	148	0.828	0.828	0.829
133	0.82	0.82	0.82	0.80	0.78	136	0.828	0.828	0.829
121	0.82	0.82	0.83	0.81	0.79	125	0.829	0.828	0.830
109	0.82	0.82	0.82	0.81	0.79	113	0.822	0.821	0.823
96.6	0.81	0.81	0.82	0.80	0.78	101	0.828	0.828	0.829
84.5	0.82	0.82	0.83	0.81	0.79	89	0.827	0.826	0.828
72.4	0.82	0.82	0.82	0.81	0.79	77.1	0.823	0.823	0.826
60.3	0.82	0.82	0.83	0.81	0.79	65.3	0.823	0.824	0.826
48.3	0.82	0.82	0.82	0.80	0.78	53.4	0.825	0.826	0.828
36.2	0.81	0.81	0.82	0.80	0.78	41.5	0.827	0.828	0.835
24.1	0.83	0.81	0.82	0.81	0.79	29.7	0.835	0.836	0.846
12.1	0.83	0.88	0.85	0.80	0.81	17.8	0.835	0.837	0.856
						5.93	0.798	0.793	0.787

Table B-8: Dynamic viscosity of 3.5 fold base medium

Shear Rate [s^{-1}]	Dynamic Viscosity [$x10^{-3}$ kg/m.s]					
	Base medium at 3.5 fold synthetic medium concentration					
	Run 1	Run 2	Run 3	Run 4	Run 5	Run 6
350	0.874	0.859	0.883	0.867	0.877	0.864
338	0.869	0.855	0.878	0.864	0.871	0.859
326	0.869	0.857	0.878	0.865	0.873	0.861
314	0.872	0.861	0.881	0.869	0.875	0.865
302	0.870	0.859	0.879	0.867	0.873	0.863
290	0.866	0.856	0.876	0.864	0.870	0.860
278	0.870	0.861	0.879	0.869	0.874	0.865
266	0.867	0.858	0.875	0.865	0.870	0.862
253	0.868	0.859	0.876	0.865	0.870	0.863
241	0.863	0.855	0.872	0.863	0.866	0.859
229	0.865	0.857	0.873	0.864	0.868	0.861
217	0.860	0.854	0.870	0.861	0.864	0.858
205	0.864	0.857	0.871	0.864	0.867	0.861
193	0.858	0.852	0.867	0.859	0.861	0.855
181	0.859	0.853	0.867	0.860	0.862	0.857
169	0.862	0.856	0.869	0.863	0.865	0.860
157	0.859	0.853	0.866	0.860	0.861	0.857
145	0.859	0.853	0.866	0.860	0.861	0.856
133	0.857	0.851	0.864	0.858	0.859	0.855
121	0.856	0.851	0.865	0.860	0.859	0.855
109	0.855	0.850	0.865	0.860	0.858	0.854
96.6	0.854	0.849	0.864	0.859	0.856	0.853
84.5	0.856	0.852	0.865	0.860	0.859	0.856
72.4	0.857	0.853	0.865	0.861	0.860	0.857
60.3	0.862	0.856	0.861	0.858	0.863	0.860
48.3	0.857	0.854	0.873	0.869	0.860	0.857
36.2	0.856	0.853	0.902	0.893	0.861	0.858
24.1	0.881	0.881	0.843	0.844	0.874	0.872
12.1	0.846	0.838	0.975	0.968	0.868	0.86

Table B-9: Density of the Avicel particles

Sample [#]	Mass [g]	Volume Displaced [mL]	Calculated Density [kg/m^3]
1	20	12	1667
2	40	25	1600
3	20	12.5	1600
4	40	26	1538
5	20	13	1538
6	40	25	1600
7	20	12.5	1600
8	40	23.5	1702

APPENDIX C: CELL RECYCLING STUDIES

Objectives

The objective of this study was to investigate the possibility of increased ethanol yields from continuously stirred tank reactors employing cell and substrate recycling schemes. The study involved evaluating the effects of lignin presence on the hydrolysis rate of cellulose, the investigation of increased cellulose conversion with higher cellulase loadings and the benefit of cellulose recycling.

Conceptual method

It is proposed that recycling yeast cells and substrate back to the reactor will produce higher ethanol yields as the substrate and yeast concentrations will remain high allowing for maximum conversion conditions to exist. Implementing a feedback scheme in combination with a continuous stirred tank reactor (CSTR) configuration has the added benefit of removing excess ethanol from the reactor. This is especially useful as ethanol inhibits the growth and performance of the organism, thus maintaining low concentrations of this potentially toxic inhibitor is favourable. Substrate recycling bears a further advantage as it returns adsorbed enzymes to the reactor, always ensuring a higher enzyme loading and thereby reducing the excess cost of continuously adding large volumes of expensive enzymes.

Research methodology

Numerical Model

The reaction kinetics model proposed by South *et al.* (1995) for pretreated poplar wood was modified, using concepts from Shao *et al.* (2008) to improve numerical stability and coded into the Matlab R2007a Student Edition (MathWorks, Inc, USA) environment. The model was verified by comparing the results with South *et al.* (1995). The reactors investigated were assumed to operate under ideal mixing conditions resulting in a homogeneous solution. It was also assumed that the pretreated lignocellulose material contained no hemicellulose to avoid by-products such as furfural and hydroxymethyl furfural forming during hydrolysis. This imitates the composition as if you pre-wash the pretreated lignocellulosic material and only use the water insoluble solids.

A reactor substrate concentration of 125 g/L was selected for this study, allowing the substrate to be concentrated to 250 g/L and fed back to the reactor without causing blockage within the system. The lignocellulosic substrate was assumed as softwood with a composition of 38.6 % lignin and 61.4 % fermentable cellulose (Hamelinck *et al.*,2005). Complete conversion of cellulose was assumed, with glucose, ethanol and carbon dioxide as products.

Effects of lignin

Cellulases adsorb onto both cellulose and lignin surfaces. Enzymes adsorbed to cellulose hydrolyse the substrate with the surrounding water and detach from the surface once completing a cellulose chain. Enzymes that adsorb to the lignin surface however are unable to perform any type of reaction and do not detach. This effectively reduces the concentration of available free enzymes in the reactor broth and therefore lower the hydrolysis rate of the reaction (Berlin *et al.*, 2005).

The effects of lignin on the hydrolysis of cellulose were evaluated with a batch type reactor configuration. The control case assumed an initial cellulose concentration of 125 g/L and yeast cell loading of 2.5 g/L with a cellulase loading of 10 filter paper units (FPU)/g cellulose and a β-glucosidase loading of 50 international units (IU)/g cellulose. The simulation was repeated with lignin present at 78.75 g/L, constituting 38.6 % of the substrate composition.

Enzyme loading

Enzyme loading generally increases the hydrolysis rate of cellulose, as the greater the enzyme concentration, the higher the probability of an enzyme protein adsorbing to an available bonding site on the cellulose surface and hydrolysing the substrate. The effect of increased enzyme loading is however limited by the available substrate surface. If all available bonding sites are actively occupied by enzymes, adding additional enzymes would have a negligible effect.

The effects of increased enzyme loading were investigated using a continuous stirred tank reactor configuration. Steady-state conditions were simulated for a substrate feed concentration of 125 g/L cellulose and β-glucosidase loading of 50 IU/g cellulose at various dilution rates to determine the converted substrate concentrations. Three cellulase feed concentrations of 10 FPU/g cellulose, 20 FPU/g cellulose and 30 FPU/g cellulose were evaluated.

Cell and substrate recycling

Recycling microorganism cells and unconverted lignocellulosic substrate back into the reactor increases the average residence time the cellulose remains in the reactor, which improves the total substrate conversion. Adsorbed enzymes are also transported with the substrate back to the reactor, which collectively should raise the reactor enzyme concentration and increase hydrolysis rates and improve efficiency.

The effects of cell and substrate recycling were investigated using a continuous stirred tank reactor configuration with a concentrated feedback loop. Steady-state conditions were simulated for a substrate feed concentration of 125 g/L cellulose, cellulase feed concentration of 10 FPU/g cellulose and β-glucosidase feed concentration of 50 IU/g cellulose at dilution rates between 0.01 h^{-1} and 0.1 h^{-1} to determine the converted substrate concentrations. Cell and substrate recycle

benefits were investigated at three recycling percentages namely 30 %, 60 % and 90 % of the exiting substrate concentration.

Results

Effects of Lignin

The presence of lignin during hydrolysis caused a lower cellulosic conversion rate due to the decrease in free enzyme concentrations in the broth. The ethanol concentration throughout the batch reaction decreased with less than 5 % when lignin was present (Figure C-1).

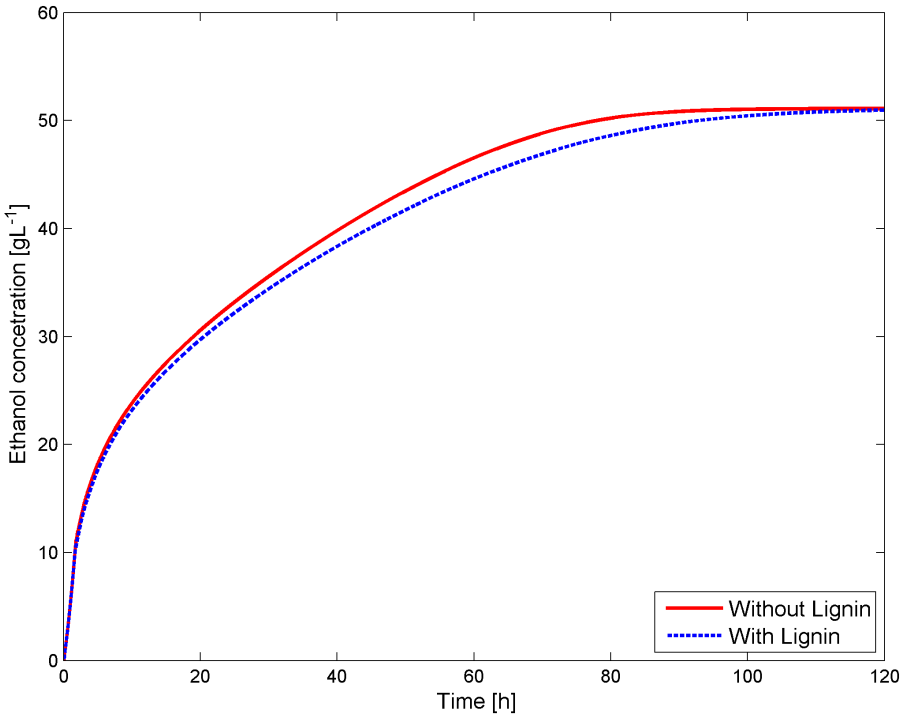

Figure C-1: Batch ethanol concentrations with and without lignin

Cellulases have a higher affinity for cellulose over lignin, causing the majority of the cellulases to bond to the cellulose. As the substrate is hydrolysed, decreasing its concentration, the excess free enzymes adsorb to the lignin (Figure C-2).

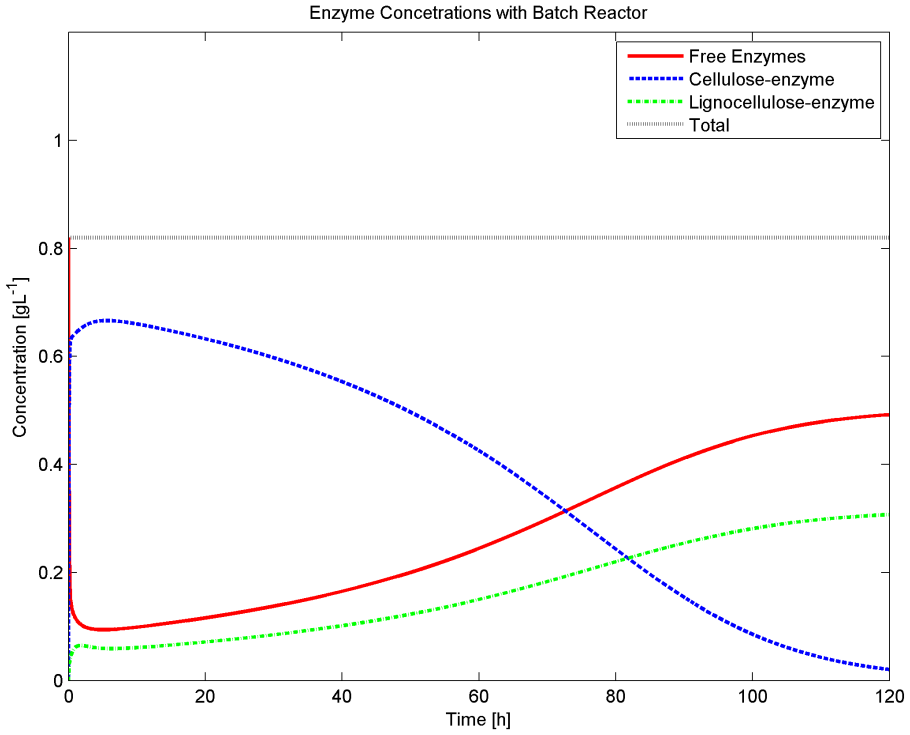

Figure C-2: Adsorbed enzyme concentrations to illustrate enzyme affinity

Enzyme loading

Increasing the feed cellulase concentration in a CSTR configuration caused higher hydrolysis rates and improved conversion of the cellulose substrate (Figure C-3). Residence time in the reactor affects the total substrate conversion, with dilution rates of $D = 0.1\ h^{-1}$ and less producing significantly higher total substrate conversion. It is important to remember that a dilution rate of $D = 0\ h^{-1}$ is essentially a batch tank reactor, which produces the maximum substrate conversion.

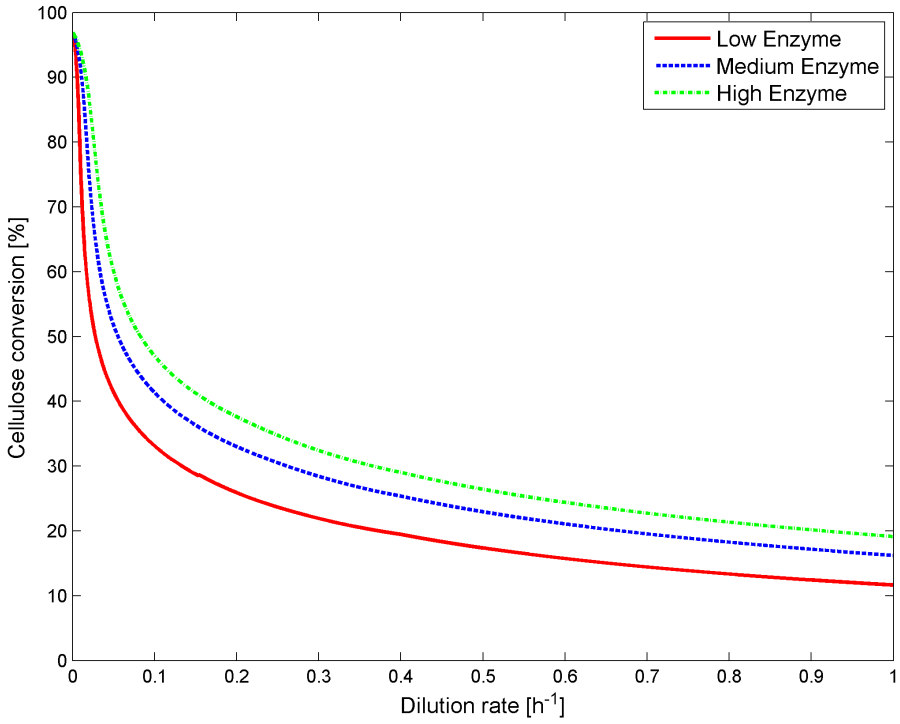

Figure C-3: Cellulose conversion at various enzyme loadings

A second important limitation on CSTR configurations is the maximum growth rate of the organism. Operating a CSTR at dilution rates greater than the maximum growth rate essentially flushes the organism from the system, preventing fermentation. The *Saccharomyces cerevisiae* organism used in this study has a maximum growth rate of μ_{max}=0.4 h^{-1} (Figure C-4).

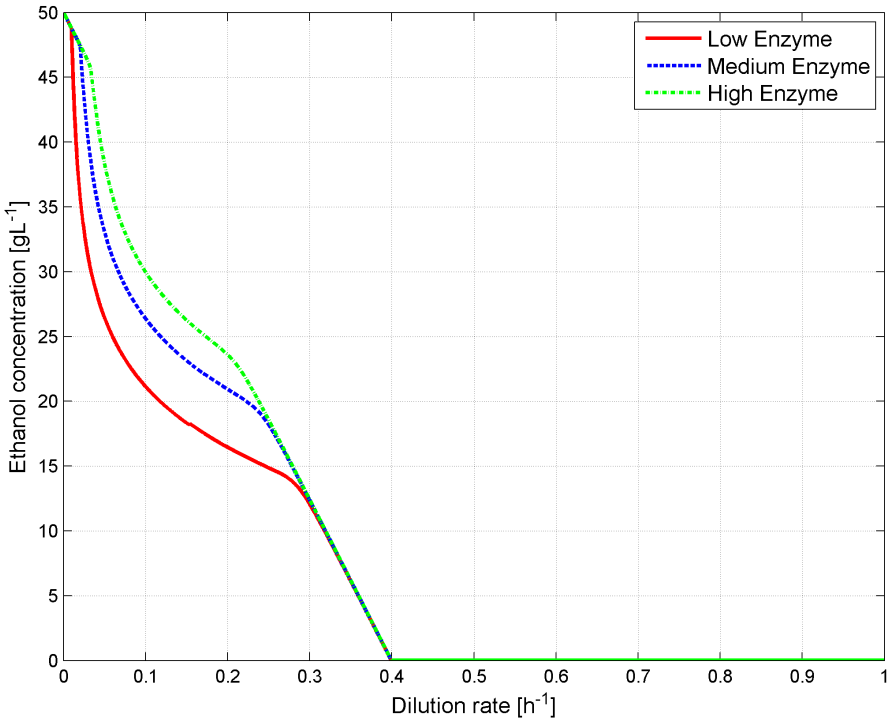

Figure C-4: Ethanol yields at various enzyme loading

Recycled cells and substrate

One primary concern when implementing a feedback loop in a CSTR system is the overfilling and subsequent blockage of or damage to the reactors. Setting a reactor limitation of 125 g/L substrate and simulating cell and substrate recycling schemes revealed that dilution rates below $D = 0.09$ h^{-1} have essentially no risk of overfilling the reactors (Figure C-5).

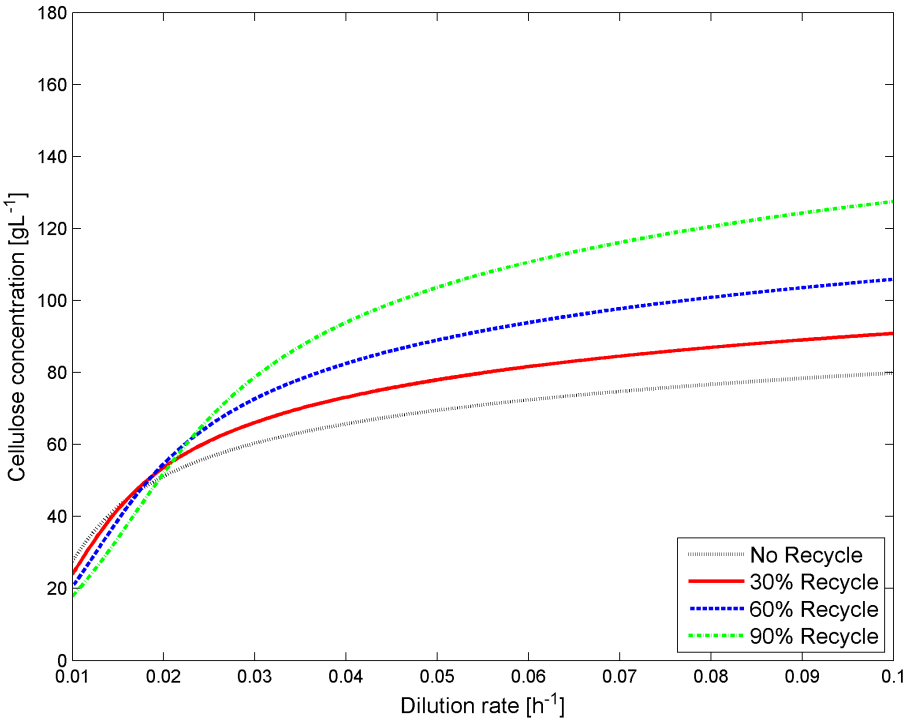

Figure C-5: Reactor cellulose concentrations as a function of dilution rate

Evaluation of the ethanol concentrations that eventually exit the reactors indicated that higher recycling percentages increase final ethanol concentrations. A maximum concentration was observed at a dilution rate of $D = 0.02$ h^{-1} with a 33 % high concentration when compared to a standard CSTR operating under similar conditions (Figure C-6).

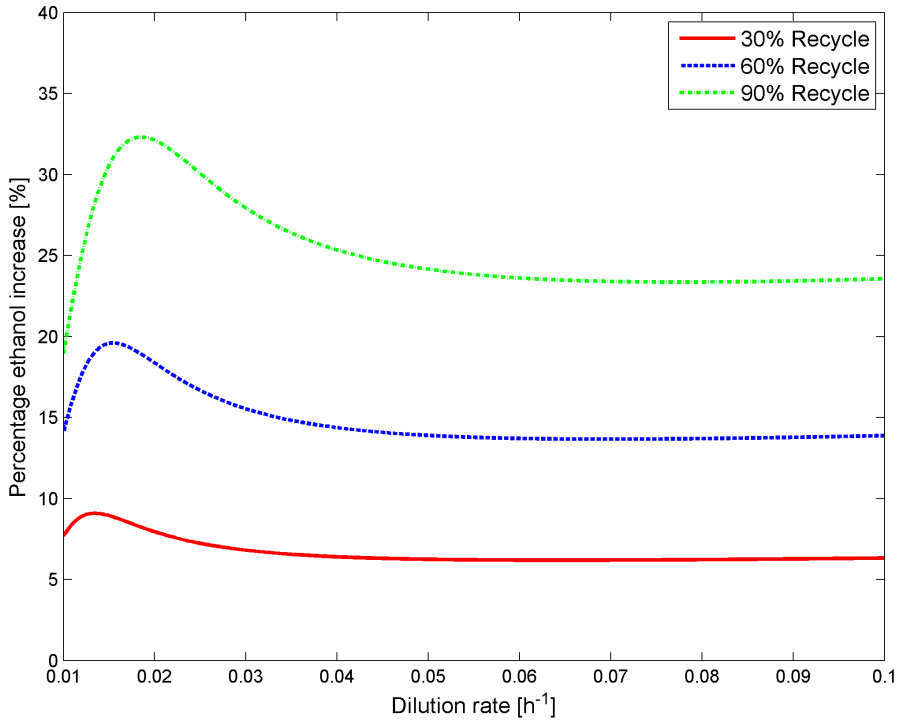

Figure C-6: Ethanol concentration increase caused by recycling substrate

Conclusions and recommendations

Effects of lignin

Conditions with high cellulose concentrations are minimally affected by the presence of lignin as cellulases have a greater affinity for cellulose than lignin. It was observed that when cellulose concentrations decrease significantly, more cellulases adsorb to the non-reactive lignin reducing the number of free enzymes available, inhibiting hydrolysis.

Substrate recycle schemes are significantly affected by the presence of lignin. This is due to the effective concentrating of the lignin in the reactor with each cycle, as lignin is insoluble and non-reactive. The presence of lignin thus results in the reactor rapidly filling and becoming blocked or damaged. Furthermore, the concentration of lignin would soon exceed that of the cellulose substrate, resulting in highly inefficient hydrolysis and decreased ethanol production. Pretreatment should therefore include methods of removing excess lignin from lignocellulosic substrates before hydrolysis and fermentation.

Enzyme loading

Cellulase loadings of 10 FPU/g cellulose, 20 FPU/g cellulose and 30 FPU/g cellulose were investigated. Observations indicated that dilution rates of $D < 0.04$ h^{-1} resulted in high cellulose conversion in excess of 70 % and that higher cellulase loadings significantly improved the hydrolysis rate. Cellulases are however expensive to produce or purchase, thus negatively affecting the attractiveness of increased enzyme loading.

Cellulase loading in excess of 30 FPU/g cellulose have been shown to have little benefit, as the enzyme capacity of the cellulose substrate becomes limited. This is caused by the limited bonding sites available on the substrate surface. Once these sites are saturated it is unable to accommodate additional enzymes.

Cell and substrate recycling

Organism and cellulose substrate recycling simulations indicated increased cellulose conversion producing higher ethanol concentrations when compared to a standard CSTR configuration. Simulations indicated a possible ethanol concentration increase of 33 % at a dilution rate of $D = 0.02$ h^{-1} with 90 % substrate recycle.

A dilution rate of $D = 0.02$ h^{-1} equates to an average residence time of 50 h. Cellulases adsorbed to the residual substrate are continuously returned to the reactor where fresh substrate is available. This effectively increases the enzyme loading of the reactor, which improves hydrolysis rates, as enzymes hydrolyse fresh substrate more efficiently (Tu *et al.*, 2007). Cellulases have been shown to remain active for periods exceeding 48 h, although the industrial environment would rapidly damage or destroy these proteins during longer operation. Recycle reactors thus require a continuous supply of new enzymes.

Operating recycle reactors at much higher dilution rates are impractical as such systems would have low substrate conversion rates, thus rapidly overfilling the reactors, and blocking or even damaging the reactors.

APPENDIX D: EXPERIMENTAL PROTOCOLS

Synthetic Complete Medium

Yeast Nitrogen Base without Amino Acids	1.7 g/L
Glucose	20 g/L
Ammonium Sulphate	5 g/L
Vitamins Solution	1 mL/L
pH	5.5 – 6.0

Vitamins Solution

D(+) Biotin	0.05 g/L
Calcium D(+) pantothenate	1 g/L
Meso-inositol	25 g/L
Nicotinic acid	1 g/L
p-amino benzoic acid	0.2 g/L
Pyridoxine (Vit B6) HCL	1 g/L
Thiamine HCL	1 g/L
$ZnSO_4$ $7H_2O$	4.5 g/L
$CoCl_2$ $6H_2O$	0.3 g/L
$MnSO_4$ H_2O	1.5 g/L
$CuSO_4$ $5H_2O$	0.3 g/L
$FeSO_4$ $7H_2O$	3 g/L
Na_2MoO_4 $2H_2O$	0.4 g/L
H_3BO_3	1 g/L
KI	0.1 g/L
$Al_2(SO_4)_3$	0.1 g/L
pH	5.5 at 30°C

Yeast peptone dextrose plates

Yeast Extract	10 g/L
Peptone	20 g/L
Glucose	20 g/L
Agar	20 g/L

pour approximately 25 mL of YPD solution into each Petri dish.

Citrate buffer

Citrate acid	10.5g/L
Sodium Citrate	14.7g/L

Mix the Citrate acid solution and Sodium Citrate solution together to a pH of 5.5.

β-glucosidase assay procedure

(van Rooyen *et al.*, 2005)

pNPG and buffer solution preparation

Dissolve 0.25 mol/L of p-nitrophenyl-β-D-glucopyranoside (pNPG) in Dimethylformamide (DMF) to a volume of 1.5 mL. Add 1.17 mL of this solution to 48.83 mL citrate buffer to create 50 mL of the reagent solution.

pNP standards for assay

Dissolve 0.025 g with citrate buffer to a volume of 50 mL to form the stock solution. Create 7 dilutions of the stock solution with a factor of 1.5.

Table D-1: Protocol for the pNPG assay to measure β-glucosidase activity

Step	Sample	Sample Blank	Reagent Blank
1	0.025 mL Sample		0.025 mL Citrate Buffer
2	0.15 mL Citrate Buffer and pNPG		
3	Incubate 2 minutes at 55°C		
4	0.075 mL of 1 mol/L Na_2CO_3		
5		0.025 mL Sample	
6	150 µL of each assay well contents and read with colorimeter at 400 nm		

Endoglucanase assay in 96-well plates

(Bailey, 1992)

Dissolve 15 g/L in citrate buffer with 7 dilutions at a factor of 1.5 each.

Dissolve 5 g of Carboxymethyl cellulose (CMC) in citrate buffer to a volume of 500 mL. Autoclave the solution to ensure the CMC dissolves completely.

Table D-2: Protocol for the CMC assay to measure endoglucanase activity

Step	Sample	Sample Blank	Reagent Blank
1	0.0083 mL Sample		0.0083 mL Citrate Buffer
2	0.075mL CMC solution		
3	Incubate 30 min at 50 °C		
4	0.167 mL of DNS		
5		0.0083 mL Sample	
6	Boil at 100 °C for 5 min		
7	150 µL of each assay well contents and read with colorimeter at 540 nm		

Cellobiohydrolase assay
(Den Haan *et al.*, 2007)

Substrate mix

Add 0.6 g Avicel along with 500 µL of 3 mol/L Na-Acetate at pH 5.0, 500 µL NaN_3 (0.5% stock solution) and 30 µL β-glucosidase (Novozym 188) with water to a volume 30 mL.

Dilute samples with acetate buffer (500 µL of 3 mol/L Na-Acetate diluted with H_2O to a volume of 30 mL).

Procedure:

Add 0.45 mL of sample to 0.45 mL substrate mix in a test tube and vortex for 2 seconds. Extract a 200 µL sample from each tube and store on ice at time 0 h and 24 h later after centrifuged for 5 min at 40 000 rpm to separate the remaining Avicel particles. For both the time 0 and 24 hour samples perform the following procedure:

Table D-3: Protocol for DNS assay to measure exoglucanase activity

Step	Samples
1	50 µL of sample (diluted 1:3)
2	100 µL of DNS
3	Heat to 99 °C for 5 min and cool to 4 °C in PCR machine
4	Transfer 50 µL to microtitre plate
5	Measure absorbance at 565 nm

Subtract the readings of the 0 hour samples from the 24 hour samples to determine the average enzyme activity.

APPENDIX E: PARAMETER DETERMINATION

The parameters selected for optimization in Chapter 3 was cellulose, produced ethanol, and adsorbed exoglucanase and endoglucanase concentrations. The goal was to find a set of parameters which minimized the average combined error for these concentrations. Although a single target parameter error could be improved, doing so could degrade the overall accuracy of the remaining target functions. The percentage error for each of the above-mentioned parameters was calculated as the absolute difference between simulated and experimental results divided by the experimental value:

$$\%\ Error = \frac{|\ Simulated\ value - Experimental\ value\ |}{Experimental\ value} \times 100\ . \qquad \text{(E-1)}$$

The combined average was calculated as the root mean square of the four separate parameter errors, allowing the largest error to dominate the optimization process:

$$\%\ Error_{mean} = \sqrt{\frac{Err^2_{Cellulose} + Err^2_{Ethanol} + Err^2_{Endoglucanase} + Err^2_{Exoglucanase}}{4}}\ . \qquad \text{(E-2)}$$

The dominant parameter error was altered by 1 % increments to minimize the combined average error or until another parameter error became dominant. This process was iteratively continued until a satisfactory result was achieved and verified by visual inspection.

Figure E-1 presents a flowchart of the procedure followed to determine the optimal parameter values for calculating the adsorbed enzymes and conversion of cellulose to ethanol.

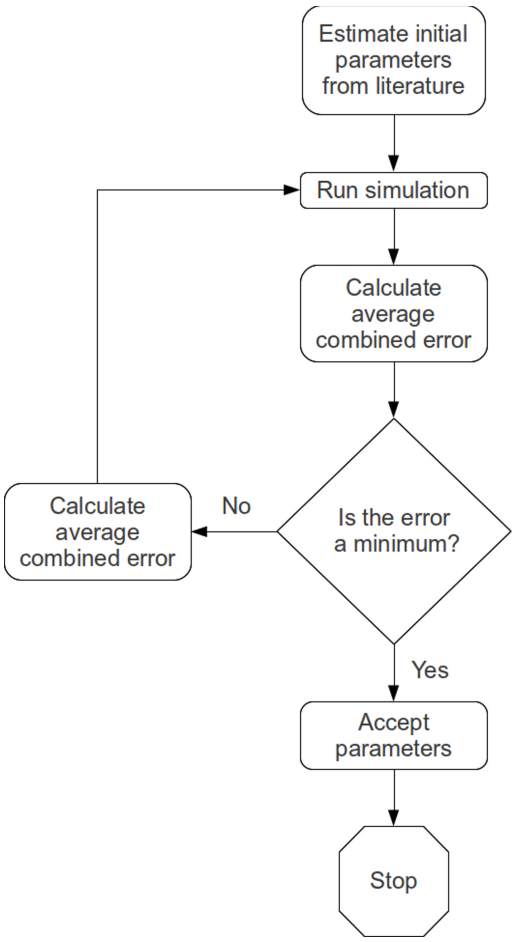

Figure E-1: Flow chart for the parameter determination algorithm

APPENDIX F: APPARATUS AND MATERIAL DETAILS

Equipment

Table F-1: Description of experimental apparatus

Component	Manufacturer	Details
PCR Machine	Applied Biosystems	2720 Thermal Cycler Part No: 4359659
Microfuge	Beckman Coulter	Microfuge 18 Centrifuge Cat No: 367161
HPLC	Thermo Fischer Scientific, Waltham, MA	Finnigan Surveyor RI-40 Milliq effluent
HPLC Coulumb	Phenomenex, Torrance, CA	Rezex RHM-Monosaccharide H+ (8%) Part no: 00H-0132-K0 Size: 300 mm x 7.8 mm
HPLC Coulumb heater	Geck 2000	Operating Temp: 60 °C
Spectrophotometer	Jenway	6100 Spectrophotometer
Rheology machine	Anton Paar	Physica MCR 501
Measuring system	Anton Paar	DG 26.7
Water Bath	Anton Paar	Viscotherm VT2
Fermenters	New Brünswick Scientific, Edison, NJ	1.3L Bioflow 110

Table F-2: Description of computer used for simulations

Component	Manufacturer	Details
Motherboard	Intel	Model: DQ-965GF
Processor	Intel	Model: Core 2 6700 (dual-core) frequency: 2.66 GHz
Graphics Card	Nvidia Corporation	Model: Geforce 8600 GT
Random access memory	Kingston	Amount: 4 GB

Software

Table F-3: Software packages used during the coarse of this work

Component	Manufacturer	Details
Comquest	Thermo Fischer Scientific, Waltham, MA	Version 4.2 http://www.thermoscientific.com/
Rheoplus	Anton Paar	32 bit Version 2.81 http://www.anton-paar.com/
MATLAB	Mathworks	Version R2007a (Student Edition) http://www.mathworks.com/
STAR-CCM+	CD-Adapco	Version 6.02.007 http://www.cd-adapco.com/

Materials

Table F-4: Description of chemicals used during this project

Component	Supplier	Details
Saccharomyces cerevisiae MH-1000	Van Zyl laboratory, Microbiology, Stellenbosch , RSA	
20 µm cellulose acetate filters	Gema Medical S.L., Barcelona, Spain	
D(+) Glucose Anhydrous	Merck Chemicals KgaA, Damstadt, Germany	Univ AR Univ LAB
Avicel PH-101	Fluka Analytical Steinheim, Germany	
Difco Yeast Nitogen Base	Becton, Dickinson and Company Franklin Lakes, NJ	Yeast Nitrogen Base without Amino Acids and Ammonium Sulphate
Spezyme CP	Genencor International, Rochester, NY	
Novozym 188	Novozymes, Bagsvaerd, Denmark	
Bicinchoninic Acid Assay	Novagen, Darmstadt, Germany	
GF/A microfiber filters	Whatman International Ltd, Banbury, UK	

REFERENCES

Abengoa, 2011, Abengoa Bioenergy, www.abengoabioenergy.com, Last accessed on 21 February 2011.

Adamenko II, Bulavin LA, Ilyin V, Zelinsky SA, and Moroz KO, 2006, Anomalous behaviour of glycerol-water solutions, Journal of Molecular Liquids, 127:90-92.

Ahuja GN and Patwardhan AW, 2008, CFD and experimental studies of solids hold-up distribution and circulation patterns in gas-solid fluidized beds, Chemical Engineering Journal, 143 :147-160.

Albers E, Larsson C, Lidén G, Niklasson C, and Gustafsson L, 2002, Continuous estimation of product concentration with calorimetry and gas analysis during anaerobic fermentations of *Saccharomyces cerevisiae*, Thermochimica Acta, 394:185-190.

Alkindi AS, Al-Wahaibi YM, and Muggeridge AH, 2008, Physical properties (Density, excess molar volume, viscosity, surface tension, and refractive index) of Ethanol + Glycerol, Journal of Chemical Engineering Data, 53:2793-2796.

Alliet-Gaubert M, Sardeing R, Xuereb C , Hobbes P, Letellier B, and Swaels P , 2006, CFD analysis of industrial multi-staged stirred vessels, Chemical Engineering and Processing 45:415–427 .

Armenante PM, Luo C,Chou C-C, Fort I, and Medek J, 1997, Velocity profiles in a closed, unbaffled vessel: comparison between experimental LDV data and numerical CFD predictions , Chemical Engineering Science, 52 (20): 3483-3492 .

Auton TR, Hunt JCR, and Prud'homme M, 1988, The force exerted on a body in inviscid unsteady non-uniform rotational flow, Journal of Fluid Mechanics, 197:241-257.

Bailey MJ, Biely P, Poutanen K. 1992. Interlaboratory testing of methods for assay of xylanase activity. Journal of Biotechnology 23:257-270.

Baumert KA, Herzog T, and Pershing J, 2005, Navigating the Numbers, World Resources Institute.

Berlin A, Balakshin M, Gilkes N, Kadla J, Maximenko V, Kubo S, and Saddler J, 2006, Inhibition of cellulase, xylanase and β-glucosidase activities by softwood lignin preparations, Journal of Biotechnology, 125:189-209.

Berlin A, Gilkes N, Kurabi A, Bura R, Tu M, Kilburn D, Saddler J, 2005, Weak Lignin-Binding Enzymes - A Novel Approach to Improve Activity of Cellulases for Hydrolysis of Lignocellulosics, Applied Biochemistry and Biotechnology , 121–124: 163–170 .

BP, 2008, BP Statistical Review of World Energy June 2008, http://www.bp.com, Last accessed on 21 May 2009.

Caminal G, López-Satín J, and Solà C, 1985, Kinetic modeling of the enzymatic hydrolysis of pretreated cellulose, Biotechnology and Bioengineering, 27:1282-1290.

Cannell MGR, 2003, Carbon sequestration and biomass energy offset: theoretical, potential and achievable capacities globally, in Europe and the UK, Biomass and Bioenergy, 24 (2): 97-116.

CD-Adapco, 2011, STAR-CCM+ Version 6.02.007 user guide.

Çengel YA and Cimbala JM, 2006, Fluid Mechanics – fundamentals and applications: First edition in SI units, McGraw Hill, Singapore.

Chirife J and Buera MP, 1997, A simple model for predicting the viscosity of oligosaccharide solutions, Journal of Food Engineering, 33:221-226.

Converse AO and Optekar JD, 1993, A synergistic kinetics model for enzymatic cellulose hydrolysis compared to the degree-of-synergism experimental results. Biotechnology and Bioengineering, 42:145-148.

Converse AO, Matsuno R, Tanaka M, and Taniguchi M, 1987, A model of enzyme adsorption and hydrolysis of microcrystalline cellulose with slow deactivation of the adsorbed enzyme, Biotechnology and Bioengineering, 32:38-45.

Converse AO, Optekar JD. 1993. A synergistic kinetics model for enzymatic cellulose hydrolysis compared to the degree-of-synergism experimental results. Biotechnology and Bioengineering 42:145-148.

Converti A, Zilli M, Arni S, Di Felice R, and Del Borghi M, 1999, Estimation of viscosity of highly viscous fermentation media containing on or more solutes, Biochemical Engineering Journal, 4:81-85.

Coughlan MP, 1992, Enzymic hydrolysis of cellulose: an overview, Bioresource Technology, 39:107-115.

Demombynes G, Özler B, 2005, Crime and local inequality in South Africa, Journal of Development and Economics, 76:265-292.

Den Haan R, Mcbride JE, La Grange DC, Lynd LR, and van Zyl WH, 2007, Functional expression of cellobiohydrolases in *Saccharomyces cerevisiae* towards one-step conversion of cellulose to ethanol, Enzyme and Microbial Technology, 40:1291-1299.

DME, 2007, Biofuels industrial strategy of the Republic of South Africa, Republic of South Africa.

Dong XF, Yu AB, 2009, Numerical analysis of the heterogeneous gas–solid flow in fluidized beds, Journal of the Taiwan Institute of Chemical Engineers, 40:645–653.

Dupont, 2011, DuPont Danisco, www.dupontdanisco.com, Last accessed on 21 February 2011.

Durand H, Soucaille P and Tiraby G, 1984, Comparative study of cellulases and hemicellulases from four fungi: mesophiles *Trichaderma reesei* and *Penicillum* sp. And thermophiles *Thielavia terrestris* and *Sporotrichum cellulpphilum*, Enzyme and Microbial Technology, 6: 175-180.

EIA, 2007, Biofuels in the U.S. Transportation Sector, Available online at http://www.eia.gov/ , last accessed on 15 November 2011.

EIA, 2011, Weekly All Countries Spot Price FOB Weighted by Estimated Export Volume (Dollars per Barrel), http://www.eia.gov , Last accessed on 21 February 2011.

Eriksson T, Karlsson J, Tjerneld F, 2002, A model explaining declining rate of hydrolysis of lignocellulose substrates with cellobiohydrolase I (Cel7A) and endoglucanase I (Cel7B) of *Trichaderma reesei*, Applied Biochemistry and Biotechnology 101 :41-60.

Faiz A, Sinha K, Walsh M, and Varma A, 1990, Automotive air pollution: issues and options for developing coutries, Policy, Research, and External Affairs, WPS 492.

Ferziger JH and Perić, 2002, Computational methods for fluid dynamics, 3rd edition, Springer, New York.

Florides GA and Christodoulides P, 2009, Global warming and carbon dioxide through science, *Environmental International*, 35:390-401

Fung YC, 1994, A first course in continuum mechanics, 3rd Edition, Prentice-Hall, New Jersey.

Ge XM and Bai FW, 2006, Intrinsic kinetics of continuous growth and ethanol production of a flocculating fusant yeast strain SPSC01, *Journal of Biotechnology*, 124:363-372.

Ghose TK and Tyagi RD, 1979, Rapid ethanol fermentation of cellulose hydrolysate II. Product and substrate inhibition and optimizationof fermentor design, Biotechnology and Bioengineering 21: 1401-1420.

Ghose TK, 1987, Measurements of cellulase activities, International Union of Pure and Applied Chemistry, 59:257-268.

Gidaspow, D, 1994, Multiphase Flow and Fluidization: Continuum and Kinetic Theory Descriptions, Academic Press, Boston.

Gírio FM, Fonseca C, Carvalheiro F, Duarte LC, Marques S, and Bogel-Łukasik R, 2010, Hemicelluloses for fuel ethanol: A review, Bioresource Technology, 100:4775–4800.

González B, Calvar N, Gómez E, and Domínguez Á, 2007, Density, dynamic viscosity, and derived properties of binary mixtures of methanol or ethanol with water, ethyl acetate and methyl acetate at T=(293.15, 298.15 and 303.15) K. Journal of Chemical Thermodynamics, 39:1578-1588.

Goyal A, Ghosh B, and Eveleigh D, 1991, Characteristics of fungal cellulases, Bioresource Technology, 36:37-50.

Gusakov AV and Sinitsyn AP, 1985, Kinetics of the enzymatic hydrolysis of cellulose: 1. A mathematical model for a batch reactor process, Enzyme and Microbial Technology, 7:346-352.

Ha SH, Mai NL An G, and Koo Y, 2010, Microwave-assisted pretreatment of cellulose in ionic liquid for accelerated enzymatic hydrolysis, Bioresource Technology, doi:10.1016/j.biortech.2010.07.108.

Hall M, Bansal P, Lee JH, Realff M and Bommarius AS, 2010, Cellulose crystallinity – a key predictor of the enzymatic hydrolysis rate, FEBS Journal, 227: 1571-1582.

Hamelinck CN, van Hooijdonk G, Faaij APC. 2005. Ethanol from lignocellulosic biomass: techno-economic performance in short-, middle- and long-term. Biomass and Bioenergy. 28: 384-410.

Hristov HV, Mann R, Lossev V and Vlaev SD, 2004, A simplified CFD for three-dimensional analysis of fluid mixing, mass transfer and bioreaction in a fermenter equipped with triple novel geometry impellers, Trans IChemE, Part C, Food and Bioproducts Processing, 82(C1): 21–34 .

Human Sciences Research C ouncil, 2004, Fact Sheet Poverty in South Africa , Available online at http://www.sarpn.org , last accessed on 15th November 2011.

International Organization of Motor Vehicle Manufacturers, 2008, http://oica.net/wp-content/uploads/all-vehicles.pdf, Last accessed on 21 February 2011.

IPCC, 2007, Climate change 2007: Synthesis Report. Contribution of Working Groups I, II and III to the Fourth Assessment Report of the Intergovernmental Panel on Climate Change [Core writing team, Pachauri, RK and Reisinger, A (eds.)]. IPCC, Geneva, Switzerland, pp. 104.

Jahoda M, Tomášková L, and Moštěk M, 2009, CFD prediction of liquid homogenisation in a gas-liquid strirred tank, Chemical Engineering Research and Design, 87:460-467.

Janssen R, Rutz D, Hofer A, Helm P, Landahl G, and Ericson J, 2007, Bioethanol for Europe – The EU project best (Bioethanol for sustainable transport), 15th European Biomass Conference and Exhibition, Berlin, Germany, 2284-2287.

Jones WP, and Launder BE, 1972, The prediction of laminarization with a two-equation model of turbulence, International Journal of Heat and Mass Transfer, 15:301-314.

Jongen T, 1998, Simulation and modeling of turbulent incompresible flows, Ph.D. dissertation, Lausanne EPFL.

Kaar WE, Holtzapple MT, 2000, Using lime pretreatment to facilitate the enzymic hydrolysis of corn stover, Biomass and Bioenergy 18: 189-199.

Kim MH, Lee and Dewey SB, Ryu DY, Reese ET, Surface deactivation of cellulase and its prevention, Enzyme and Microbial Technology, 4: 99-103.

Kumar R and Wyman CE, 2008, An improved method to directly estimate cellulase adsorption on biomass solids, Enzyme and Microbial Technology, 42:426-433.

Kuo C and Lee C, 2009, Enhancement of enzymatic saccharification of cellulose by cellulose dissolution pretreatments, Carbohydrate Polymers, 77:41-46.

La Grange DC, den Haan R, van Zyl WH, 2010, Engineering cellulolytic ability into bioprocessing organisms, Applied Microbiology and Biotechnology, 87:1195-1208.

Lance M, and Bateille J, 1991, Turbulence in liquid phase of a uniform bubbly air-water flow, Journal of Fluid Mechanics, 222:95-118.

Launder BE,. and Sharma BI, 1974, Application of the energy dissipation model of turbulence to the calculation of flow near a spinning disc, Letter in Heat and Mass Transfer, 1(2):131-138.

Lee J, 1997, Biological conversion of lignocellulosic biomass to ethanol, Journal of Biotechnology, 56:1-24.

Lee Y and Fan LT, 1982, Kinetic studies of enzymatic hydrolysis on insoluble cellulose: Analysis of the initial rates, Biotechnology and Bioengineering 24 : 2383-2406.

Linde M, Galbe M and Zacchi G, 2008a, Bioethanol production from non-starch carbohydrate residues in process streams from a dry-mill ethanol plant, Bioresource Technology, 99:6505-6511.

Linde M, Jakobsson E, Galbe M, Zacchi G. 2008b, Steam pretreatment of dilute H_2SO_4-impregnated wheat straw and SSF with low yeast and enzyme loadings for bioethanol production, Biomass and Bioenergy. 32: 326-332.

Luukkonen P, Newton JM, Podczeck F, and Yliruusi J, 2001, Use of a capillary rheometer to evaluate the rheological properties of microcrystalline cellulose and silicified microcrystalline cellulose wet masses, International Journal of Pharmaceutics, 216:147157.

Lynd LR, Weimer PJ, van Zyl WH, and Pretorius IS, 2002, Microbial cellulose utilization: Fundamentals and Biotechnology, Microbiology and Molecular Biology Reviews, 66 (3): 506-577.

Malinowski JJ., Lafforgue C, and Goma G, 1987, Rheological behaviour of high density continuous cultures of *Saccharomyces cerevisiae*, Journal of Fermentation Technology, 65 (3): 319-323.

Mancini M and Moresi M, 2000, Rheological behaviour of baker's yeast suspensions, Journal of Food Engineering, 44:225-231.

Martín M, Montes FJ, Galán MA, 2010, Mass transfer rates from bubbles in stirred tanks operating with viscous fluids , Chemical Engineering Science, 65: 3814–3824 .

Mascoma, 2011, Mascoma Corporation, www.Mascoma.com, Last accessed on 21 February 2011.

Matthews JF, Skopec CE, Mason PE, Zuccato P, Torget RW, Sugiyama J, Himmel ME, and Brady JW, 2006, Computer simulation studies of microcrystalline cellulose Iβ, Carbohyd. Res. 341 138-152.

Meroney RN, and Colordo PE, 2009, CFD simulation of mechanical draft tube mixing in anaerobic digester tanks, Water Research, 43:1040-1050.

Moilanen P, Laakkonen M, and Aittamaa J, 2005, Modelling fermenters with CFD, European Symposium on Computer Aided Process Engineering, 15:709-714.

Montante G and Magnelli F, 2004, Liquid homogenization characteristics in vessel stirred with multiple Rushton turbines mounted at different spacings CFD study and comparison with experimental data, Trans IChemE, Part A, Chemical Engineering Research and Design, 82(A9): 1179–1187 .

Moreira R, Chenlo F and LeGall D, 2009, Kinematic viscosity and refractive index of aqueous solutions of ethanol and glycerol, Industrial & Engineering Chemistry Research, 48:2157-2161.

Naik SN, Goud VV, Rout PK, and Dalai AK, 2010, Production of first and second generation biofuels: A comprehensive review, Renewable and Sustainable Energy Reviews, 14:578-597.

Nere NK, Patwardhan AW, Joshi JB, 2003, Liquid-phase mixing in stirred vessels: turbulent flow regime, Industrial & Engineering Chemistry Research, 42 (12): 2661-2698.

Ng GH, Ding YL and Ghadiri M, 2009, Modelling of dense and complex granular flow in high shear mixer granulator – A CFD approach, Chemical Engineering Science, 64 :3622-3632.

Nissen TL, Schulze U, Nielsen J, Villadsen J, 1997, Flux distributions in anaerobic, glucose-limited continuous cultures of *Saccharomyces cerevisiae*, Microbiology 143: 203-218.

Ooshima H, Burns DS, and Converse AO, 1990, Adsorption of cellulase from *Trichoderma reesei* on cellulose and lignacious residue in wood pretreated by dilute sulfuric acid with explosive decompression, Biotechnology and Bioengineering, 36:446-452.

Panwar N.L., Kaushik S.C., Kothari S., 2011, Role of renewable energy in environmental protection: A review. Renewable and Sustainable Energy Reviews. 15:1513-1524.

Paul EL, Atiemo-Obeng VA and Kresta SM, 2004, Handbook of industrial mixing – Science and practice, John Wiley and Sons, Inc., Hoboken, New Jersey.

Phillippidis GP, Smith TK, and Wyman CE, 1992, Study of the enzymatic hydrolysis of cellulose for production of fuel ethanol by the simultaneous saccharification and fermentation process, Biotechnology and Bioengineering 41:846-853.

Ramos LP, Breuil C and Saddler JN, 1993, The use of enzyme recycling and the influence of sugar accumulation on cellulose hydrolysis by *Trichoderma* cellulases , Enzyme and Microbial Technology, 15: 19-25.

Reidy, S., 2010. DuPont Danisco opens cellulose facility, Biofuels Business, 4 (2):20-23.

Reilly J, Paltsev S Felzer B, Wang X, Kicklighter D, Melillo J, Prinn R, Sarofim M, Sokolov A, and Wang C, 2007, Global economic effects of changes in crops, pasture, and forests due to changing climate, carbon dioxide, and ozone, Energy Policy, 35:5370-5383.

Reuß M, Josić D, Popović M, Bronn WK, 1979, Viscosity of yeast suspensions, European Journal of Applied Microbiology and Biotechnology, 8:167-175.

Ryu DDY and Mandels M, 1980, Cellulases: biosynthesis and applications, Enzyme and Microbial Technology, 2:91-102.

Sagar AD, 1995, Automobiles and global warming: alternative fuels and other options for carbon dioxide emissions reduction, Environmental Impact Assessment, 15 (3):241-274.

Sanin FD, 2002, Effect of solution physical chemistry on the rheological properties of activated sludge, Water SA, 28 (2):207-211.

Scheiding W, Thoma M, Ross A, and Schügerl K, 1984, Modelling of the enzymatic hydrolysis of cellobiose and cellulose by a complex enzyme mixture of *Trichoderma reesei* QM 9414, Applied Microbiology and Biotechnology, 20:176-182.

Shao X, Lynd LR, Wyman CE, and Bakker A, 2008, Kinetic modeling of cellulosic biomass to ethanol via simultaneous saccharification and fermentation: Part I. Accommodation of intermittent feeding and analysis of staged reactors, Biotechnology and Bioengineering, 102:59-65.

Shih T-H, Liou WW, Shabbir A, Yang Z, and Zhu J, 1994, A new k-ε eddy viscosity model for high Reynolds number turbulent flows -- model development and validation, NASA TM 106721.

Shiller L and Naumann A, 1933, Uber die grundlegenden Gerecgnnungen bei der Schwerkraftaufbereitung VDI Zeits, 77 (12): 318-320.

Siddiqui A and Fleten S-E, 2010, How to proceed with competing alternative energy technologies: A real option analysis. Energy Economics, 32 :817-830.

South CR, Hogsett DAL, and Lynd LR, 1995, Modeling simultaneous saccharification and fermentation of lignocellulose to ethanol in batch and continuous reactors, Enzyme and Microbial Technology, 17:797-803.

Staniforth JN, Baichwal AR, Hart JP, and Heng PWS, 1988, Effect of addition of water on the rheological and mechanical properties of microcrystalline celluloses, International Journal of Pharmaceutics, 41:231-236.

Statistics South Africa, Online at http://www.statssa.gov.za , last accessed on 15th November 2011.

Sun CC, 2005, True density of microcrystalline cellulose, Journal of Pharmaceutical Sciences, 94 (10):2132-2134.

Syamlal M and O'Brien TJ, 1988, Simulation of granular layer inversion in liquid fluidized beds, International Journal for Multiphase Flow, 14 (4): 473-481.

Syamlal M, 1985, Multiphase hydrodynamics of gas-solids flow, Ph.D. Dissertation, Illinois Institute of Technology, Chicago, Ill.

Tu M, Chandra RP, Saddler JN, 2007, Evaluating the distribution of cellulases and the recycling of free cellulases during the hydrolysis of lignocellulosic substrates, Biotechnology Progress, 23: 398-406.

Twigg MV, 2007, Progress and future challenges in controlling automotive exhaust gas emissions, Applied Catalysis B: Environmental, 70:2-15.

U.S. Census bureau, 2009, http://www.census.gov/ , Last accessed on 20 May 2009.

United States Environment Protection Agency, 1996, http://www.epa.gov/ , Last accessed on 23 January 2011.

Van Rooyen R, Hahn-Hägerdal B, La Grange DC, van Zyl WH, 2005, Construction of cellobiose-growing and fermenting *Saccharomyces cerevisiae* strains, Journal of Biotechnology, 120:284-295.

Van Zyl JM, van Rensburg E, van Zyl WH, Lynd LR, and Harms TM, 2011, A kinetic model for simultaneous saccharification and fermentation of avicel with *Saccharomyces cerevisiae*, Biotechnology and Bioengineering. 108:924-933.

Van Zyl WH, van Zyl JM, Harms TM, van Rensburg E, Lynd LR, 2011, System for modelling the conversions of lignocellulosic materials. (PCT/IB2011/001590; Filed 8 July 2011).

Verduyn C, Postma E, Scheffers WA, and Van dijken JP, 1992, Effect of benzoic acid on metabolic fluxes in yeast: a continuous-culture study on the regulation of respiration and alcoholic fermentation, Yeast, 8:501-507.

Versteeg HK and Malalasekera W, 1995, An introduction to computational fluid dynamics, the finite volume method, Pearson Prentice Hall, New York.

Walker LP and Wilson DB, 1991, Enzymatic hydrolysis of cellulose: an overview, Bioresource Technology, 36:3-14.

White FM, 1991, Viscous fluid flow, second edition, McGraw-Hill International Editions, New York.

World Bank, 2008, *World Development Indicators 2008*.

World Resources Institute, CAIT v.6, 2009, Washington DC, http://cait.wri.org/, Last accessed on 2 February 2009.

World Resources Institute, CAIT v.8, 2011, Washington DC, http://cait.wri.org/, Last accessed on 21 February 2011.

Wyman CE, 2007, What is (and is not) vital to advancing cellulosic ethanol, Trends in Biotechnology, 25 (4) : 153-157.

Yang B, Willies DM, and Wyman CE, 2006, Changes in the enzymatic hydrolysis rate of Avicel cellulose with conversion, Biotechnology and Bioengineering, DOI: 10.1002/bit. 20942.

Zhang J, Shao X, Townsend OV, and Lynd LR, 2009, Simultaneous saccharification and co-fermentation of paper sludge to ethanol by *Saccharomyces cerevisiae* RWB222-Part 1: Kinetic modeling and parameters, Biotechnology and Bioengineering, 104:920-931.

Zhang YP and Lynd LR, 2004, Towards an aggregated understanding of enzymatic hydrolysis of cellulose: Noncomplex cellulase systems, Biotechnology and Bioengineering 88: 788-824.

Zheng J, Pollack GH, 2003, Long-range forces extending from polymer-gel surfaces. Physical Review E, 68 031408.